Master's thesis

Synthesis and structure determination of novel honeycomb layered $A_2Ni_2TeO_6$ (A = Na, K) type and other oxidotellurates(VI)

carried out at the

X-ray Center TU Wien

supervised by

Privatdoz. Dipl.-Ing. Dr.techn. Berthold Stoeger

conducted
by

Tobias Wolflehner, BSc BSc

Vienna, January 11, 2023

Tobias Wolflehner

Abstract

Novel battery materials promise improvements in the efficiency and sustainability of energy storage. Recent research into $A_2M_2TeO_6$ honeycomb layered oxidotellurates(VI) (for short: $A_2M_2TeO_6$ honeycomb tellurates) has demonstrated them as potential electrode materials, owing to their high voltage (up to 4V for $K_2Ni_2TeO_6$) vs. K/K^+ and reversible K ion insertion. In this work, we investigate novel $A_2M_2TeO_6$ (A=Na, K; M=Ni) honeycomb tellurates and demonstrate the existence of novel phases in this system. Moreover, we show that stacking faults and superstructures occur in multiple $A_2M_2TeO_6$ type phases, as has already been shown for $Na_2Ni_2TeO_6$. Several other novel oxidotellurates(VI) (including $Ca_3Cu_3Te_2O_{12}$), a mixed valence oxidotellurate $Ca_2Te_2O_7$ and two calcium oxidotellurate(IV) chlorides ($Ca_2TeO_3Cl_2$ and $Ca_5Te_4O_{12}Cl_2$) are described as well.

Solid-state (600-800°C) and hydrothermal (210°C) synthesis routes were employed to obtain crystalline products. Samples were characterized with single crystal X-ray diffraction (single crystal XRD), powder diffraction (powder XRD), scanning electron microscopy (SEM), energy dispersive X-ray spectroscopy (EDX), transmission electron microscopy (TEM) and electron diffraction (ED), depending on the crystal size present in the sample. Where suitable single crystals were present, single crystal XRD was the preferred method.

A novel $K_4Ni_5Te_3O_{16}$ honeycomb tellurate was synthesized (space group $Amm2$, $a = 12.0639(8)$ Å, $b = 25.2528(16)$ Å, $c = 10.4470(6)$ Å). In the honeycomb layer formed by $[(Ni,Te)O_6]$ octahedra, two edge sharing $[TeO_6]^{6-}$ octahedra form a $[Te_2O_{10}]^{8-}$ subunit in the honeycomb layer surrounded by $[NiO_6]^{10-}$ octahedra. This structural feature was previously unknown in $A_2M_2TeO_6$ honeycomb tellurates. In the hitherto described honeycomb tellurate structures $[TeO_6]^{6-}$ octahedra share edges only with $[MO_6]^{10-}$ units. Furthermore, one-dimensional diffuse scattering in the form of diffuse rods was observed in the $K_4Ni_5Te_3O_{16}$ phase and the novel $Na_{2(x-y)}Ni_xTe_yO_{2(x+y)}$ and $K_{2(x-y)}Ni_xTe_yO_{2(x+y)}$ type phases. This is due to stacking faults of the honeycomb layers, which was also evidenced by high resolution TEM imaging. It clearly showed the presence of stacking faults in a $K_2Ni_2TeO_6$ single crystal.

Other novel tellurates such as $Ca_3Cu_3Te_2O_{12}$ were synthesized as byproducts. Finally, TEM and ED measurements revealed the presence of further novel phases in the $Na_{2(x-y)}Ni_xTe_yO_{2(x+y)}$ and $K_{2(x-y)}Ni_xTe_yO_{2(x+y)}$ systems. Single crystal XRD measurements could not be performed for these latter phases, since no suitable single crystals were found. Rb and Cs analogues could not be obtained, even after numerous systematic experiments. We found some indications for the presence of Rb honeycomb tellurates in few samples, which proved to be inconclusive.

The results presented here improve the understanding of $A_2M_2TeO_6$ honeycomb tellurates which can be used to better gauge their suitability as battery materials in the future. Moreover, we demonstrated that multiple novel honeycomb tellurate phases exist in the already investigated systems. Further research into this direction seems promising.

Zusammenfassung

Neue Kathodenmaterialien in Batterien stellen Verbesserungen der Energiespeicherung in Hinsicht auf Effizienz und Nachhaltigkeit in Aussicht. Sogenannte "honeycomb layered oxidotellurates(VI)" (zu Deutsch etwa: „Honigwabenartige Oxidotellurate(VI)", kurz: „Honigwabentellurate") zeigten vielversprechende elektrochemische Eigenschaften in der akademischen Forschung der letzten Jahre, wie ein hohes elektrochemisches Potential gegen K/K^+ (bis zu 4 V für $K_2Ni_2TeO_6$) und reversible K+ Ionen De- und Interkalation. In dieser Arbeit befassen wir uns mit neuen $A_2M_2TeO_6$ (A=Na, K; M=Ni) Honigwabentelluraten und zeigen die Existenz von einigen bisher unbekannten Phasen in zuvor untersuchten Systemen. Außerdem zeigen wir, dass Stapelfehlordnungen (wie schon für $Na_2Ni_2TeO_6$ bekannt) und Überstrukturen in Honigwabentelluraten prävalent sind. Zusätzlich präsentieren wir einige andere neue Oxidotellurate(VI) wie $Ca_3Cu_3Te_2O_{12}$, das gemischt-valente Te(IV)/Te(VI) $Ca_2Te_2O_7$ und zwei Oxidotellurat-Chloride $Ca_2TeO_3Cl_2$ und $Ca_5Te_4O_{12}Cl_2$.
Es wurden Hydrothermal- und Festkörpersynthesen durchgeführt. Die kristallinen Proben wurden dann mit Einkristall-Röntgendiffraktion, Rasterelektronenmikroskopie (REM), energiedispersiver Röntgenspektroskopie (EDX), Transmissionselektronenmikroskopie (TEM) und Elektronen Diffraktion (ED) untersucht, je nach Größe und Güte der Kristalle.
Ein neues Honigwabentellurat $K_4Ni_5Te_3O_{16}$ ($a = 12.0639(8)$ Å, $b = 25.2528(16)$ Å, $c = 10.4470(6)$ Å, Raumgruppe $Amm2$) zeigte die erwartete Schichtstruktur aufgebaut aus $[(Ni,Te)O_6]$ Oktaedern und K Schichten. Allerdings sind bislang in Honigwabentelluraten unbekannte $[Te_2O_{10}]^{8-}$ Untereinheiten vorhanden, die in den Oktaederschichten aus zwei benachbarten $[TeO_6]^{6-}$ Oktaedern zusammengesetzt sind. Bisher wurden in Honigwabentelluraten lediglich $[TeO_6]^{6-}$ Oktaeder beobachtet, die von $[MO_6]^{10-}$ Oktaedern umgeben sind. Außerdem wurde eindimensionale diffuse Streuung in dieser Phase beobachtet, wie auch in mehreren neuen $Na_{2(x-y)}Ni_xTe_yO_{2(x+y)}$ und $K_{2(x-y)}Ni_xTe_yO_{2(x+y)}$ Phasen. Sie wird durch Stapelfehlordnungen der Schichten erzeugt, was durch TEM Aufnahmen bestätigt werden konnte. Hierdurch konnten wir die Anwesenheit von Stapelfehlordnungen in der schon bekannten Phase $K_2Ni_2TeO_6$ nachweisen. Weitere Oxidotellurate wie $Ca_3Cu_3Te_2O_{12}$ wurden als Nebenprodukte erzeugt.
Die zuvor erwähnten $Na_{2(x-y)}Ni_xTe_yO_{2(x+y)}$ und $K_{2(x-y)}Ni_xTe_yO_{2(x+y)}$ Phasen wurden durch TEM und ED Messungen nachgewiesen, wobei Einkristalldiffraktion wegen der geringen Kristallgröße und -güte nicht möglich war. Daher liegen für diese Phasen noch keine Strukturlösungen vor. Versuche, Rb und Cs Analoga für diverse Übergangsmetalle M zu erhalten, ergaben für Rb gemischte und für Cs keine Erfolge.
Mit den hier präsentierten Ergebnissen wird das Verständnis von Honigwabentelluraten verbessert. Das wird es in Zukunft erleichtern, ihre Eignung als Kathodenmaterialien für Batterien weiter zu untersuchen. Außerdem haben wir die Notwendigkeit nachgewiesen, auch schon charakterisierte Systemen weiter zu untersuchen. Weitere Forschung in diese Richtungen erscheint aus unser derzeitigen Perspektive vielversprechend.

Contents

Preface

I would like to use this preface to express my sincere gratitude to everyone who assisted me in the making and writing of this master's thesis. Especially my advisor, Dr. Berthold Stöger provided me not only with ample expert support, but also took much time out of his busy schedule to discuss various topics of interest and problems I encountered. Many others also helped me along the way and without their help, this work would have likely been the worse for it. Prof. Matthias Weil allowed me the usage of his lab facilities for the practical side of this thesis, assisted with ampoule production and gave me valuable tips on synthesis strategy.
Dipl.-Ing. Werner Artner introduced me to many of the measurement setups in the X-ray Center TU Wien and assisted with the technical side of things. I also appreciated the friendly and cooperative atmosphere at the X-ray Center TU Wien and everyone involved in the group in particular Dr.in Klaudia Hradil and Prof. Erich Halwax for the interesting discussions and professional help, Paul Sicher BSc for the cordial discussions and Dipl.-Ing. Martin Nastran, who introduced me to the laboratory and gave me tips based on his own experience writing a master's thesis. Additionally I would like to thank Dipl.-Ing. Felix Eder for the professional help working on single crystal structure solution and modelling and Alexandre Marsollier, since he synthesized two samples which I was allowed to investigate. Ing. Christian Zaruba performed EDX measurements and the USTEM of TU Wien performed TEM measurements for this thesis, in particular Dr. Michael Stöger-Pollach, for which I am very grateful as well.
Furthermore I also appreciate the support of people, who were not directly involved but made the work much more enjoyable. My close friends, parents and also everyone who proof-read and corrected some part or all of this work. Without the support of many different people this thesis would not exist as it does now.

1 Introduction

1.1 General overview

In this thesis, the synthesis and crystal structures of novel $A_2M_2TeO_6$ honeycomb layered oxidotellurates(VI) (short: $A_2M_2TeO_6$ honeycomb tellurates) and other oxidotellurates as well as oxidotellurate chlorides are described. The introduction starts off by giving the motivation behind honeycomb tellurate research and a broad overview of tellurium. An introduction into various relevant aspects of tellurium chemistry, crystallography and a literature overview on honeycomb tellurates follow.
An overview of oxidotellurate chemistry is given next, followed by a very short summary of the employed synthesis methods. Honeycomb layered structures are discussed, since $A_2M_2TeO_6$ honeycomb tellurates are the main focus of this thesis. Special attention is given to the topics of diffuse scattering and stacking faults, since they are the source of much woe in the characterization of $A_2M_2TeO_6$ honeycomb tellurates. Lastly, because of the interest in the application as battery materials, see for example [1], an overview of the electrochemical research on $A_2M_2TeO_6$ honeycomb tellurates is given.

1.2 Motivation

Today, one of the industrially most relevant tellurium compounds is CdTe. Its bandgap of 1.4–1.6 eV [2] is well suited for absorption of visible light. Therefore it is a suitable material for application in thin film solar cells as an alternative to the ubiquitous α-Si technology [3]. In 2022 the Cadmium Telluride Accelerator consortium was funded by the US Department of Energy (DoE). This consortium aims to stimulate study and development of Cadmium Telluride photovoltaic technology [4]. Moreover, academic interest in tellurium compounds exists as well. Relative to the scarcity of the element, tellurium minerals are surprisingly abundant [5], which drives mineralogical and geological interest.
In recent years, research into battery materials has also found new avenues in $A_2M_2TeO_6$ honeycomb tellurates, which promise good alkali ionic conductivity and high voltage at the expense of specific energy. As will be demonstrated in this thesis, $A_2M_2TeO_6$ honeycomb tellurates often exhibit interesting structural traits such as stacking faults and occupational disorder. Stacking faults result in one-dimensional diffuse scattering, which needs to be modelled separately from standard crystal structure refinement methods. Therefore, crystallographic interest in these compounds is likewise present.
There is also a growing technological demand of CdTe in the context of the energy transition away from fossil fuels. Furthermore, there are the afore discussed academic interests and potential applications in the field of battery technology. All of these factors warrant further study and investigation into the general behaviour of $A_2M_2TeO_6$ honeycomb tellurates and related phases.

1.3 Tellurium and oxidotellurate chemistry and coordination geometry

Tellurium is a rare element with an appreciable range of chemical states and coordination geometries. It was discovered in 1782 in various mineral forms in gold ores [6], but even in modern days research into novel tellurium containing phases continues. An example of this is the discovery of novel oxidotellurates, of which $A_2M_2TeO_6$ honeycomb tellurates are a subgroup.
Tellurium usually occurs in the oxidation states of -II, 0, +IV and +VI. The tellurides containing Te(-II) are a subgroup of the so-called sulfosalts, which are a loosely related group of minerals that contain S, Se or Te as anions. Different definitions and conventions exist for what constitutes a sulfosalt [7], which we will sidestep here by giving a broad description. They can be viewed as oxide analogues, in which the oxygen is replaced by other chalcogens. In nature, sulfosalts make up a large portion of naturally occurring tellurium minerals and are relevant in the field of mineralogy. Examples of tellurides include cubic $AgAuTe_4$ (Sylvanite) [8], PbTe (Altaite) [9] and CdTe [10] (with no corresponding mineral form).
Another relevant subgroup of tellurium compounds are the oxidotellurates. They contain Te(IV) and/or Te(VI) coordinated by oxygen. Numerous mixed-valence oxidotellurates containing Te(IV) and Te(VI) such as $Cd_2Te_2O_7$ [11] and $SrTe_3O_8$ [12] are likewise known. A Te(V) oxidation state is sometimes misattributed to some of these mixed-valence oxidotellurates in crystal structure databases. This may happen when Te(IV) and Te(VI) occur in a 1:1 ratio, mimicking a Te(V) state. Up to now, no stable +V oxidation state has been confirmed for Te.
In oxidotellurates, generally the Te and O atoms form an anionic $[TeO_x]^{y-}$ coordination complex. Te(IV) and Te(VI) feature remarkably distinct coordination behaviour and coordination geometry. The $5s^2$ lone pair of Te(IV) favors lower coordination numbers. For example, Te(IV) may often occur in trigonal pyramidal $[TeO_3]^{2-}$ or disphenoidal $[TeO_4]^{4-}$ configurations [5]. In contrast Te(VI) mostly shows octahedral $[TeO_6]^{6-}$ coordination in oxidotellurates, which is suppressed in Te(IV) by the presence of the lone pair. For this reason, a good indication for the presence of Te(VI) vs. Te(IV) in a crystal structure is the octahedral coordination geometry. The mentioned geometric coordinations are shown in figure 2. The given examples are by no means exhaustive, since numerous other geometries such as tetrahedral $[Te(IV)O_4]^{4-}$ are also known.

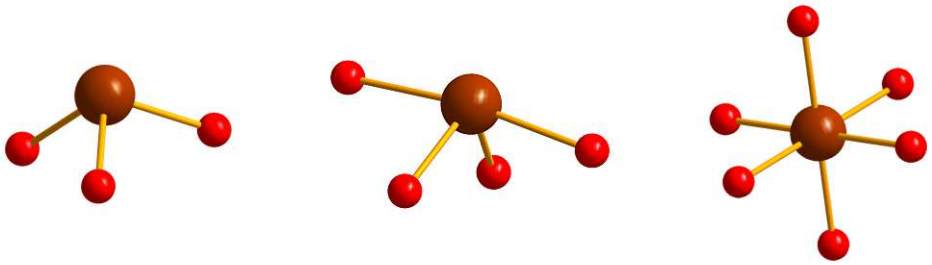

(a) Trigonal pyramidal $[TeO_3]^{2-}$ coordination of a Te(IV) position in $Cd_2Te_2O_7$.

(b) Disphenoidal or seesaw $[TeO_4]^{4-}$ coordination of a Te(IV) position in β-TeO_2 [13].

(c) Typical octahedral $[TeO_6]^{6-}$ coordination geometry of Te(VI) in $Ca_3Cu_3Te_2O_{12}$.

Figure 2: Several possible oxidotellurate coordination geometries.

Often, multiple of these monomeric $[TeO_x]^{y-}$ units link together to form larger $[Te_{x'}O_{y'}]^{z'-}$ polyhedra

by sharing of corners, edges and/or faces [5]. In this way, the $[TeO_x]$ polyhedra can form periodic structures such as chains, layers or networks. Some examples are shown in figure 3. Sometimes these structures also include other coordination polyhedra such as $[NiO_6]^{10-}$ octahedra. Therefrom arises an impressive amount of structural diversity in oxidotellurates, which is especially prevalent in mixed-valence oxidotellurates.

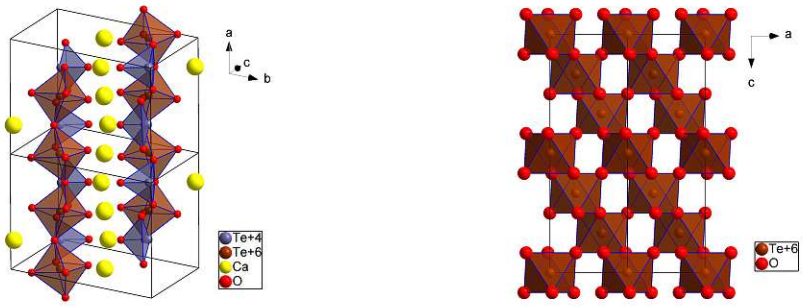

(a) Chains of $[Te(VI)O_6]^{6-}$ octahedra in $Ca_2Te_2O_7$. Also visible are trigonal pyramidal $[Te(IV)O_4]$ in blue, bridging octahedra.

(b) Triperiodic $[Te(VI)O_6]$ octahedral network in TeO_3 [14].

Figure 3: Two periodic $[Te(VI)O_6]^{6-}$ octahedra structural features; $[Te(VI)O_6]^{6-}$ chains (left) and $[Te(VI)O_6]^{6-}$ octahedral network (right).

Christy, Mills and Kampf (2016) [5] introduced a nomenclature for Te structural features based on the silicate nomenclature. In silicates, the $[SiO_4]^{4-}$ tetrahedra can connect to form various larger oligo- and polymeric structure elements. For example, inosilicates such as $MgCaSi_2O_6$ [15] consist of monoperiodic chains or bands of $[SiO_4]^{4-}$ tetrahedra which are linked by corners. Phyllosilicates such as $Al_2Si_2O_5(OH)_4$ [16], on the other hand, form diperiodic layers of tetrahedra. For the sake of simplicity and accessibility, this nomenclature for oxidotellurates will not be used in this work, although we acknowledge the usefulness and rigidity of this approach.
Similar to the silicates, oxidotellurates can contain structures from monomeric isolated units and monoperiodic chains, up to triperiodic networks, as was discussed before. TeO_2 and TeO_3 [14] can be considered as boundary cases in this context, since they contain only $[TeO_x]^{y-}$ units. TeO_3 features the typical $[TeO_6]^{6-}$ octahedra which are linked by corners to form a triperiodic network, as is also shown in figure 3 above. TeO_2 has three known modifications that are stable close to normal conditions. Tetragonal α-TeO_2 also known as paratellurite [17], orthorhombic β-TeO_2 [13] and the metastable γ-TeO_2 [18]. While all TeO_2 modifications consist of disphenoidal $[TeO_4]^{4-}$ units, α-TeO_2 and β-TeO_2 feature a triperiodic network, built of corner sharing $[TeO_4]^{4-}$ units. Meanwhile, γ-TeO_2 shows layers of edge sharing $[TeO_4]^{4-}$ polyhedra.

1.4 Honeycomb tellurate crystal structure and layered makeup

Elementary crystallographic concepts such as the space group types, symmetry operations or Bravais lattices, will not be discussed here. Instead, it will be assumed that the reader is familiar with these concepts. An exact and helpful description of the basics of symmetry and crystallography is given along much other information by Müller in "Symmetry Relationships between Crystal Structures" [19]. A very complete picture is furthermore given by the International Tables for Crystallography, Volume A [20].
Many discussions on honeycomb layer structures refer to the crystal structure of brucite $Mg(OH)_2$ [21] as a kind of parent structure. Brucite shows a layered makeup consisting of edge sharing $[Mg(OH)_6]^{4-}$ octahedra, arranged in a hexagonal layer. This description will not be favoured in this work because of the large discrepancy between the OH ligands in brucite and the alkali A and oxygen atoms in honeycomb tellurates.

1.4.1 Honeycomb tellurate layers

Honeycomb layered crystal structures consist of layers that can be derived from the honeycomb geometry. A single layer can be considered a diperiodic structure, which has lost its third direction of translational symmetry in the stacking direction. The symmetry of three-dimensional diperiodic objects is described by the layer groups [22]. They are therefore the analogue to the space groups which describe the symmetry of three-dimensional triperiodic objects.
There exist 80 layer group types, in contrast to the 230 space group types or 17 plane group types (which are the two-dimensional space group type analogue). Honeycomb layers are most easily pictured by imagining a natural honeycomb as depicted in figure 4. However, this honeycomb does not form an ideal periodic layer, since the translational symmetry is violated. The sketch in the next figure 5 shows an idealization which preserves proper translational symmetry. This is a realization of a honeycomb net, with the highest possible symmetry. A hexagonal two-dimensional lattice is shown in 5b, which shares many features with the realization of the honeycomb net. Importantly, it features additional vertices, or lattice points, as they are called in the context of lattices.

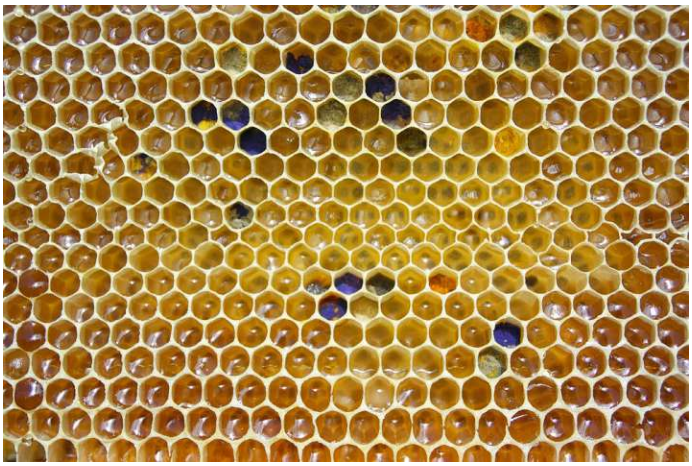

Figure 4: Picture of a natural bee-made honeycomb. Picture by Richard Woeber [23].

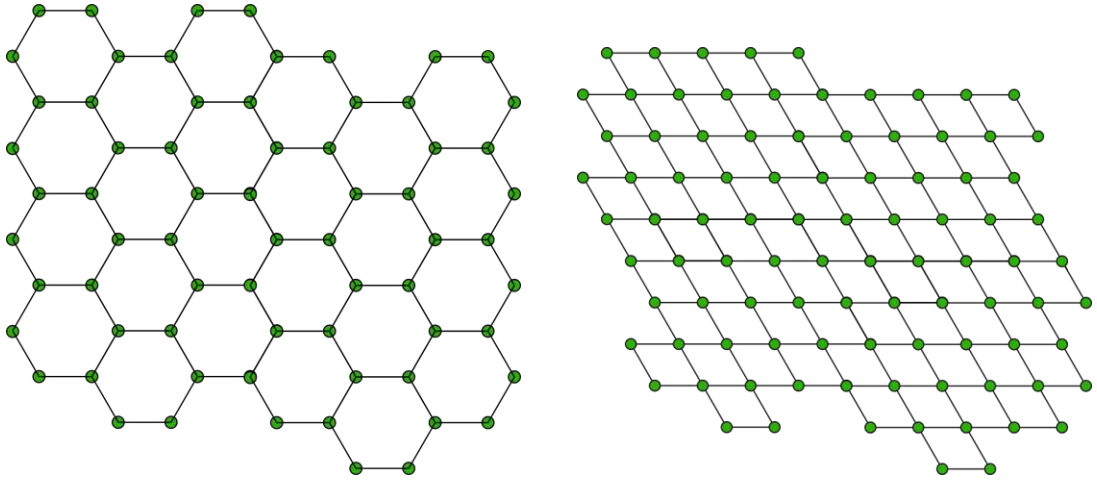

(a) A realization of the two-dimensional honeycomb net.

(b) Two-dimensional hexagonal lattice.

Figure 5: Visualization of the honeycomb geometry and a two-dimensional hexagonal lattice.

It can be easily seen that the hexagonal lattice possesses a sixfold rotation point (not axis, since it is two-dimensional), which is present in any arbitrary lattice point. In comparison, the honeycomb geometry, when interpreted as an atomic layer of sorts, is "missing" some atoms. It also possesess a sixfold rotation, which is located in the central gap between the atoms. Moreover it has a threefold rotation in the position of the atoms themselves.
As is described in the International Tables for Crystallography, Volume E [22], only eight hexagonal layer group types exist. We can consider the hexagonal two-dimensional lattice as a three-dimensional layer instead. In this case, it gains a mirror plane in the third dimension and assumes the highest symmetry of the eight layer group types, the layer group type number 80, $p6/mmm$. The honeycomb geometry also assumes this symmetry under the assumption that only the walls of the honeycomb are considered, which is implicit in the projection to the two-dimensional. The natural honeycomb does include a base, which causes the mirror plane perpendicular to the sixfold axis as well as the inversion center to be lost. This is because the natural honeycomb actually consists of "cup like" hexagonal walls. Depending on whether the bees have filled the "cups", they are either semi-closed or topped with a lid. In this case the layer group $p6mm$ would be assigned to the honeycomb geometry instead.
In the ideal $A_2M_2\mathrm{TeO}_6$ honeycomb tellurate structure, the M and Te atoms sit on a two-dimensional hexagonal lattice as the one shown before in figure 5. Therefore, the metal atoms alone form a perfect hexagonal layer with the layer group $p6/mmm$. Literature and contemporary research refers to $A_2M_2\mathrm{TeO}_6$ type oxidotellurates(VI) as "honeycomb tellurates", even though the main constituents of the layers, the Te atoms and transition metal atoms M are located on a hexagonal lattice. The denomination does make sense in that the alkali A atoms are usually positioned in a honeycomb arrangement. Furthermore, if the Te atoms are ignored in the (Te,M) layers, the M atoms are also arranged this way. Still, there is some ambiguity and in some sense "hexagonal" could be used to denominate these compounds just as well. We will keep in accordance with the literature

convention henceforth as well and will refer to the $A_2M_2TeO_6$ phases as "honeycomb tellurates". Each of the (Te,M) atoms is coordinated octahedrally by six oxygen atoms. Overall, the octahedra are edge linked which produces a [(Te,M)O_2] layer structure, as can be seen in figure 6. The [(Te,M)O_2] makeup occurs, since every oxygen atom is shared between three [(Te,M)O_6] octahedra. The layer group of the [(Te,M)O_2] layers is a subgroup of $p6/mmm$, namely $p\bar{3}m1$. The sixfold rotation is reduced to a $\bar{3}$ rotoinversion, while one of the two fold axes and a mirror plane are lost entirely.
A summary of the symmetry relations is shown together with the family honeycomb layer structure and the [(Te,Ni)O_2] layer of $K_2Ni_2TeO_6$ in figure 6. Also shown is the symmetry relation of the novel $K_4Ni_5Te_3O_{16}$, which will be discussed in the results.

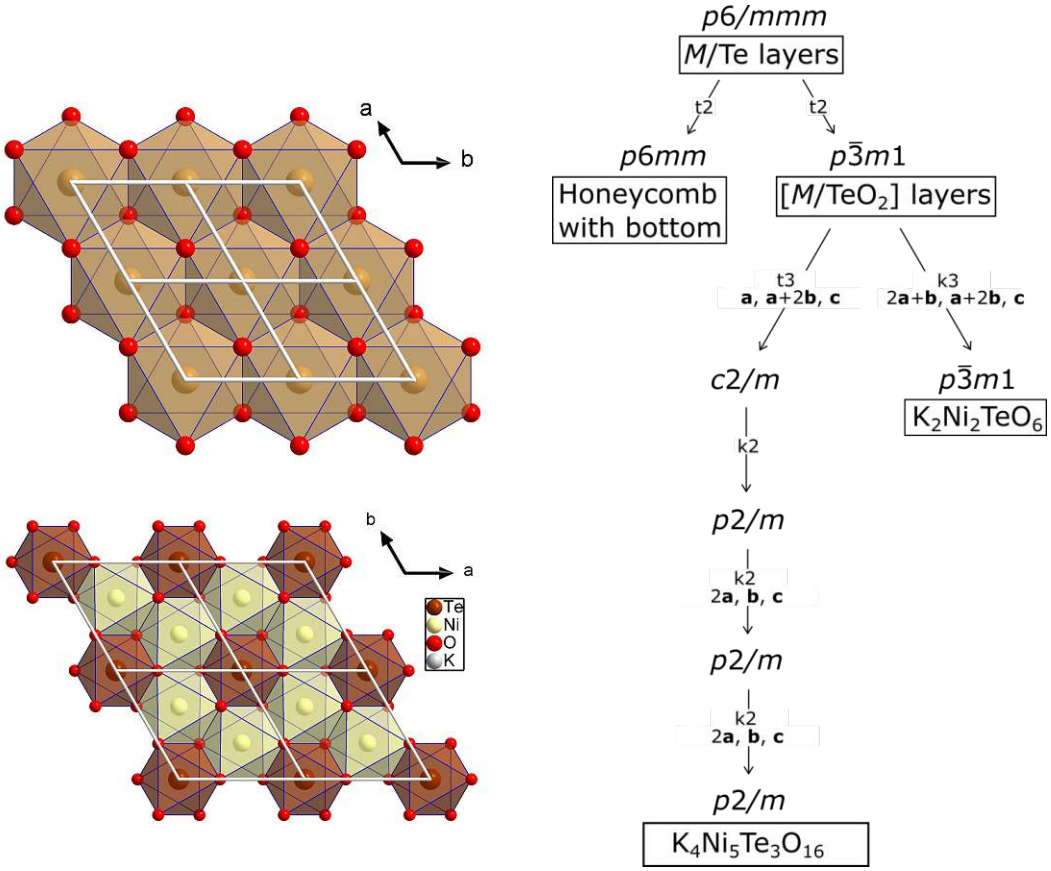

(a) Layer family structure (above) and ordered honeycomb layer of $K_2Ni_2TeO_6$ (below).

(b) Bärninghausen tree of different relevant honeycomb layers.

Figure 6: Layer symmetry relations between different geometries, considered here are always the M,TeO_2 layers of $A_2M_2TeO_6$ honeycomb tellurates.

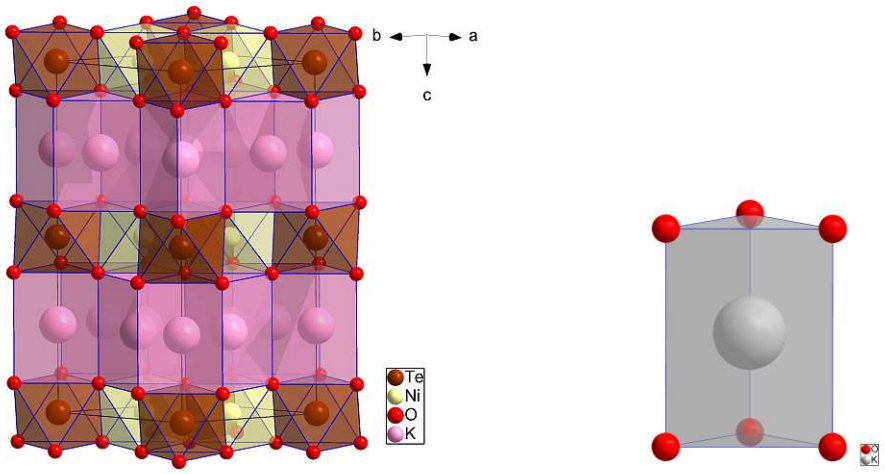

(a) Crystal structure of $K_2Ni_2TeO_6$ [24].

(b) Trigonal prismatic $[KO_6]$ coordination geometry in $K_2Ni_2TeO_6$.

Figure 7: Crystal structure of $K_2Ni_2TeO_6$ and potassium coordination geometry in the structure.

The alkali atoms are positioned between the $[(Te,M)O_2]$ layers in honeycomb layers themselves. Na and K honeycomb tellurates are known, in both of which the alkali atoms coordinate prismatically, as shown in figure 7a. Since there are more positions than alkali atoms in the unit cell, the positions are not fully occupied. Interestingly, while the relative coordinates of the alkali positions in both $Na_2Ni_2TeO_6$ and $K_2Ni_2TeO_6$ as reported by [24] are the same, the alkali occupancy in these positions is not. Although alkali atom ordering is possible [24], it does not seem to occur in $Na_2Ni_2TeO_6$ and $K_2Ni_2TeO_6$. Overall, $K_2Ni_2TeO_6$ as reported by Masese et al.[24] shows a much more inhomogenous alkali distribution than $Na_2Ni_2TeO_6$, which can be explained by the increased repulsion between the K ions in comparison to Na ions, owing to their larger ionic radius.
Because of the structural makeup with isolated alkali layers, one of the decisive factors influencing the thermodynamic stability of the $A_2M_2TeO_6$ honeycomb tellurates is the alkali-alkali repulsion. In $K_2Ni_2TeO_6$ the distance between the partially occupied K sites is roughly 3 Å, which is already unusually close. While this is somewhat countered by the partial occupation of these sites, this only escalates with growing atomic number of the alkali atom. The ionic radius of the next higher atomic number alkali atom Rb is roughly 0.14 Å larger than that of K [25]. Therefore, the Rb-Rb repulsion would grow in relation to the Rb-O interactions in hypothetical $Rb_2Ni_2TeO_6$ honeycomb tellurates. Additionally, the prismatic $[AO_6]^{11-}$ coordination would be distorted in the long axis towards a linear coordination geometry, because of the forced widening of the honeycomb layer distance by the larger Rb atoms. These considerations show that there is likely a cutoff in alkali atom size at which $A_2M_2TeO_6$ honeycomb tellurates are still stable. Since Na and K honeycomb tellurates are known, this cutoff is likely to be Rb or Cs. Because of this conjecture, the synthesis of Rb and Cs $A_2M_2TeO_6$ honeycomb tellurates was one of the foci of this thesis. This will be discussed further in the results.

1.5 Diffuse scattering and stacking faults in honeycomb tellurates

X-ray diffraction is a method that is very well suited to solve and refine crystal structures or identify crystalline phases. Single crystals show an essentially discrete diffraction image when a single crystal XRD measurement is performed. Defects, limited crystallite size, thermal diffuse scattering and similar real world effects cause the deviation from discrete, sharp Bragg reflections. On the other side of the material spectrum, there are amorphous materials, such as glass or opals. They show a continuous diffraction image and display diffuse scattering instead.
Diffuse scattering can be categorized further by its periodicity. Everything from one-dimensional (diffuse rods) up to three-dimensional diffuse scattering (diffuse clouds) can occur. The order of this dimensionality gives the corresponding, still present periodicity in the structure. For example, a completely amorphous glass particle exhibits three-dimensional diffuse scattering and therefore has no (or zero-dimensional) long range order. On the other hand, a hypothetical liquid crystal with perfectly ordered layers (two-dimensional long rage order) would present one-dimensional diffuse rods.
The layered makeup and the presence of at least two distinct layers (the alkali A and the Te,$M\mathrm{O}_2$ layers) of honeycomb tellurates suggests that they are, in fact, an a layered structure with a high stacking fault probability. Often, this can be explained by application of the OD theory [26], which describes structures with different stacking arrangements that are locally equivalent. As a result of stacking faults, one-dimensional diffuse scattering would be expected to manifest as diffuse rods in the diffraction image.
The $A_2M_2\mathrm{TeO}_6$ honeycomb tellurates that are known so far, do in fact have two differing [(Te,M)O_2] layers, as is shown in figure 8. In the following, layers will be named as $\mathbf{X'_y}$ where $\mathbf{X}$ is a letter which denotes the composition, the prime marker ' is a marker for a symmetry operation and the subscript $\boldsymbol{y}$ is a sequential number. The [(Te,M)O_2] layers in $\mathrm{K_2Ni_2TeO_6}$ can be described as an $\mathbf{A_1}$ layer and $\mathbf{A'_1}$ layer which share the same composition, but $\mathbf{A'_1}$ is formed by applying a sixfold rotation on the $\mathbf{A_1}$ layer, which is not a symmetry operation of the layer group of $\mathbf{A_1}$. In contrast, $\mathrm{K_2Ni_2TeO_6}$ has only one kind of K layer, which is denoted as $\mathbf{B}$. The K atoms favour a trigonal

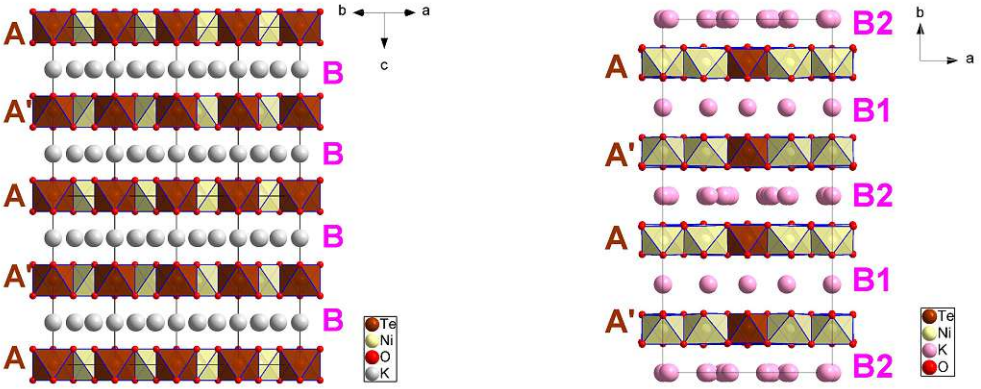

(a) Layer nomenclature in $\mathrm{K_3Ni_3TeO_6}$.

(b) Layer nomenclature in $\mathrm{K_4Ni_5Te_3O_{16}}$.

Figure 8: Layer nomenclature in both $\mathrm{K_3Ni_3TeO_6}$ (a) and $\mathrm{K_4Ni_5Te_3O_{16}}$ (b).

prismatic $[KO_6]^{11-}$ coordination. If an ($\mathbf{A_1A_1}$) or ($\mathbf{A_1'A_1'}$) order were to occur, the K positions would show a trigonal antiprismatic coordination, which would also be clearly evident from single crystal X-ray data, since the scattering amplitude of Te and Ni are high. The ($\mathbf{A_1A'_1}$) ordering preserves the K coordination and the same Ni and Te positions (in x and y). This is possible, since the metal atoms themselves form a layer of the highest layer symmetry $p6/mmm$. The extended layer, containing the oxygen atoms as well, only has the layer group of $p\bar{3}/m1$. Therefore, the sixfold rotation is a symmetry operation of the metal atom layer, but not the whole (Te,M)O_2 layer.
Stacking faults in $A_2M_2TeO_6$ honeycomb tellurates can be explained by the fact, that while the oxygen positions are highly important for the K coordinations, the Ni and Te atoms that form a higher symmetry layer themselves are not. Therefore a shift of the (Te,M)O_2 layer by the non lattice vector ($1/3$,$1/3$,0) preserves the trigonal prismatic $[KO_6]^{11-}$ coordination, while exchanging the Ni and Te positions. Two new layers are obtained, which are denoted as $\mathbf{A_2}$ and $\mathbf{A'_2}$ by the nomenclature as explained before. Because there is only one kind of Wyckoff position for Ni and Te respectively in the $Na_2Ni_2TeO_6$ and $K_2Ni_2TeO_6$ crystal structures, only one possible shift vector is present.
This way, a relatively simple model for stacking faults in $Na_2Ni_2TeO_6$ and $K_2Ni_2TeO_6$ can be conceived. Starting from a ($\mathbf{A_1}$) layer (without loss of generality) the next layer will be either a $\mathbf{A'_1}$ or $\mathbf{A'_2}$ layer, because K coordination must be preserved. The chance that this a stacking fault occurs will be between 0 and 1, where 0 represents the perfect crystalline structure with ($\mathbf{A_1A'_1A_1A'_1...}$) layer order and 1 complete disorder, where no correlation between $\mathbf{A_1}$ or $\mathbf{A_2}$ type layers can be found. In principle, this model is a Markov chain with two states ($\mathbf{A_1}$ and $\mathbf{A_2}$ type layers), where the transition probability between the two states is somewhere between 0 and 1. More exact, it would be a discrete-time Markov chain, which is a kind of stochastic model.
In practice, the degree of disorder can be modelled quantitatively with algorithms, such as the one used by DIFFAX [27]. This was only done qualitatively in this thesis, by comparison of boundary cases with the observed diffraction images. In the case of no disorder, sharp reflections are expected. Conversely, if the disorder parameter is not equal to 0, diffuse rods will be observed instead of reflections. These diffuse rods will be oriented in the reciprocal direction of the stacking layer's normal vector. If some correlation between the layers persists (a disorder parameter of $0 < p < 0.5$), an internal structure will be visible in the rods in the form of intensity maxima and minima. The maxima will be positioned where the reflections would be expected in the case of no disorder. In between these lie the minima. If the disorder parameter approaches 1 this internal structure will vanish and the rods will be of even intensity (discounting losses of intensity by higher scattering angles).
In this way, a qualitative picture of the stacking faults and a simple model can be conceived and falsified for honeycomb tellurates. In case of more diverse and complex arrangements of metal atoms in the layer, these models will gain complexity in that multiple different shift vectors, or even other operations may be necessary.

1.5.1 Possibilities for magnetic ordering in honeycomb layers

Another field of interest pertaining to honeycomb tellurates is their magnetic properties. $Na_2Ni_2TeO_6$ has been shown to possess an antiferromagnetic transition temperature of ca. 27 K by Episcopo et al. [28]. In magnetically ordered materials, be they ferro-, ferri- or antiferromagnetic, unpaired electrons align their spins in the crystal structure. Forgoing magnetic domains, the most basic prerequisite for this behaviour in single crystals is the presence of unpaired electrons in and of

itself.
$Na_2Ni_2TeO_6$ is a honeycomb tellurate which contains Ni(II) atoms. Ni(II) has an electron configuration of [Ar]$3d^8$ and is coordinated octahedrally. Crystal field theory states that this leads to a well known splitting of the d orbitals into t_{2g} and e_g levels. Because of the $3d^8$ electron configuration, a Ni(II) atom will carry two unpaired electrons with octahedral coordination, because of the order of occupation of these energy levels. Meanwhile, the Te(VI) atoms show a [Kr]$4d^{10}$ electron configuration and possess no unpaired electrons.
In order to show antiferro- or ferrimagnetic behaviour, spins of unpaired electrons need to align aparallelly macroscopically, or at least throughout large regions of a crystal. In certain trigonal or hexagonal structures this can be inhibited. While aparallel spin alignment is aspired, if a triangle of spins is considered, this can not be fulfilled for all three spins. This phenomenon is known as magnetic geometrical frustration and occurs in various structures.
Aparallel alignment of Ni(II) d electron spins in the layer in $Na_2Ni_2TeO_6$ is possible, which can be easily checked by arranging the spins on the honeycomb geometry. However, a honeycomb tellurate which we will describe in the results, $K_4Ni_5Te_3O_{16}$, shows an arrangement of $[TeO_6]^{6-}$ and $[NiO_6]^{10-}$ octahedra, which does allow for geometric frustration. The reality of this conjecture still remains an open question, since we did not measure magnetic properties of our samples.

1.6 Current state of honeycomb tellurate research

Honeycomb tellurate research is largely motivated by the search for novel electrode materials for batteries. This is certainly motivated in part by the need for sustainable energy storage in the near future. New developments in battery technology will invariably draw comparison to lithium ion batteries, the most widely successful and efficient type of modern battery. As such, many of the hitherto described honeycomb layered tellurates contain Li as an alkali component. One of the highest density cathode materials in early lithium ion battery development was Li_xCoO_2 [29] which has been used in batteries for many years. The base structure of $LiCoO_2$ [30] itself and also partially depleted Li_xCoO_2 ($0<x<1$) proved to possess high Li^+ ion conductivity coupled with a high redox potential. It is made up of hexagonal octahedra layers with the composition of $[CoO_2]$, quite similar to the $[(Te,M)O_2]$ layers in honeycomb tellurates.
Following this classic cathode material, various other phases were tested and developed for potential use in lithium ion batteries. Some of these phases include $Li_3Zn_2SbO_6$ [31], $Li_3Ni_2SbO_6$ [32], $Li_3Mn_2SbO_6$ [33], which are antimonates possessing the same layered octahedral structure and also the Li tellurates $Li_8Cu_2Te_2O_{12}$, $Li_8Co_2Te_2O_{12}$ [34] and Li_4ZnTeO_6 [35]. Interestingly, not only do Sb and Te display similar coordination geometries in these phases, but Li also tends to form octahedra. For this reason, phases such as Li_4ZnTeO_6 contain layers of $[ZnO_6]$ and $[TeO_6]$ with $[LiO_6]$ octahedra mixed in.
The predominance of Li in honeycomb tellurate research started waning when the first Na honeycomb tellurates $Na_2M_2TeO_6$ were discovered in 2011 by Evstigneeva et al. [36], including notably $Na_2Ni_2TeO_6$. The electrochemical properties of $Na_2Ni_2TeO_6$, including the Na ion diffusion pathways, were later investigated by Bera and Yusuf in 2020 [1]. The coordination geometry of the alkali atoms with higher atomic number than Li does not allow for insertion into the tellurium honeycomb layers anymore, since Na and K coordinate trigonal prismatically in these compounds. Therefore, the formula of $A_2M_2TeO_6$ is usually observed in Na and K type honeycomb tellurates, with clearly distinct $[(Te,M)O_2]$ and A alkali layers.
Following the discovery of the Na-type honeycomb tellurates, Masese et al. described the first K-type $A_2M_2TeO_6$ honeycomb tellurates including $K_2Ni_2TeO_6$ [24]. They also found Co, Mg and other analogue phases, where K shows the same trigonal prismatical coordination as Na in $Na_2Ni_2TeO_6$. While the high density of tellurates (due to the high molecular weight of Te) causes a lower specific energy, Na and K honeycomb tellurates may be an alternative research avenue to traditional Li battery materials. For example, they may find application in non mobile energy storage in the future . Further research on $A_2M_2TeO_6$ honeycomb tellurates can be expected, including this work investigating the existence of possible new phases. Other works also concentrated on heterovalent substitution in honeycomb tellurates, such as [37]. Finally, related phases include the potassium honeycomb layered structure $K_2Mn(II)_2(H_2O)_2C_2O_4(HPO_3)_2$ [38] and the monoclinic vanadates $Mn_5(VO_4)_2(OH)_4$ and $Mn_6O(VO_4)_2(OH)$ [39].
This is the current state of research on honeycomb tellurates. Prospects for current and future research endeavours include the substitution of Li, Na and K by Rb or Cs (as will be discussed later, Rb and Cs substitution was investigated in this work, but Rb and Cs analogues of the honeycomb tellurates were not obtained) and investigating possible candidates for the M metal component, such as Cr(III) or Sr(II) among others.

1.7 Overview of honeycomb tellurate electrochemical properties

In this work we concentrated on the synthesis and structural characterization of honeycomb layered oxidotellurates(VI). Naturally, as materials discussed for use in batteries, their electrochemical properties remain of great interest, especially since good cationic conductivity and a high redox potential (around 4 V for $K_2Ni_2TeO_6$) were demonstrated for $Na_2Ni_2TeO_6$ and $K_2Ni_2TeO_6$ by [24] and [1] respectively. K ion batteries are of great technological and academic interest in aqueous [40] and non aqueous form [41]. A comprehensive overview of K ion batteries was given by Pramudita et al. [42].
The advent of lithium ion batteries sparked interest into layer-type electrode materials. The insertion and extraction of alkali metal ions has proven to be a bottleneck of battery development, since it can limit the rate of charging/discharging and lower battery efficiency. To minimize this effect the presence of low energy diffusion paths is essential. This means that the energy potential barriers between possible sites in the crystal structure should be as low as possible. Channel-type structures can fulfill this criterion, since there is essentially a single degree of freedom with energy barriers in between channel sites. However, in a layer arrangement, there exist a greater number of different diffusion paths which can result in a lowered activation energy for the movement of cations. To calculate the potential barriers, the semi-empirical BVEL method (bond valency energy landscape) can be used, which is based on the bond valence method to determine the bottlenecks in the paths between atomic sites. This approach was used by Bera and Yusuf [1] to investigate the diffusion paths of $Na_2Ni_2TeO_6$.
Different kinds of honeycomb tellurates have been synthesized to date, which share the same basic structure shown previously in figure 7a on page 7. It is desirable for electrode materials to possess some sort of occupational disorder in the conducting ion positions (usually alkali ions). This is advantageous, since this disorder not only reduces the kinetic barriers by introducing defects into the crystal structure, but also prevents the ordering of the crystal structure. If electrode materials experience multiple ordering transitions (of alkali atoms) during discharge, the voltage of the whole cell will show multiple plateaus with sharp decreases in voltage, which is undesirable from a technical point of view. In light of this, the investigation of these ordered $A_2M_2TeO_6$ honeycomb tellurates is of interest for the electrochemical application, if only to prevent their formation.

1.8 Relevant crystal growth and synthesis methods

In this section, some crystal growth methods will be discussed from a theoretical and practical point of view. Solid state and hydrothermal pathways as well as pathways in a closed atmospheres (ampoules) and chemical transport will be summarized briefly. Since the solubility of the investigated tellurates in water is very low and results in decomposition rather than solvation, classical methods, such as crystallization from solution are not viable.

1.8.1 Solid state synthesis

Solid state synthesis is one of the mainstays of anorganic synthesis and it is also known as the "ceramic method". The reactants are combined in solid form and usually do not melt or sublime in bulk. This means that reactions are kinetically controlled by diffusion processes in the solid state. Therefore, high temperatures and temperature resistant crucibles are employed.
Even today, many solid state reactions are not well understood, because of the complex processes, concentration gradients and the difficulty of analysis (largely differing reaction media, as opposed

to reactions in solvents). In principle, a rough understanding can be gained by considering three main factors: The formation of crystallization nuclei, the diffusion of reactants and the growth of the nuclei by the reaction on the grain boundaries. In practice, these parameters can not be easily modified. Therefore, fundamental research is often done by trial and error and systematic variation of accessible parameters. These range from temperature gradient, heating time, reactant ratios and the gas atmosphere to the crucible material and the cooling time. A priori considerations often lead to promising synthesis results, but are not guaranteed to do so.
Solid state synthesis methods find extensive applications in industrial applications, such as in concrete production, firing ceramics or powder metallurgy. Usually, these processes are well known and investigated because of their technological importance and the extensive research performed on them.

1.8.2 Hydrothermal synthesis

Hydrothermal synthesis generally describes synthesis methods utilizing water as a reaction medium under temperatures >100°C and pressures >1 bar. This method mimics a phenomenon that often occurs in nature: Water that is trapped deep underground in rocks and magmatic surroundings can reach very high temperatures and pressures while staying liquid (or supercritical). In this state, the solubility of many minerals and compounds increase significantly, leading to the formation of hydrothermal deposits, where the water cools off and various minerals crystallize.
Hydrothermal synthesis can be useful in scientific research, because high temperatures often increase the solubility of normally insoluble reactants. Moreover, in the lab (or by coincidence in nature) a mineralizer can be added, which is a compound that further increases solubility. For example, $(NH_3)_{aq}$ might be used to facilitate hydrothermal synthesis of copper salts, since it forms the highly soluble and stable $[Cu(NH_3)_4](H_2O)_2{}^{2+}$ complex in aqueous solution. Further discussion on hydrothermal synthesis can be found for example in the review given by Rabenau 1985 [43].
A clear advantage of the method is that high temperatures typically needed in solid state synthesis can be avoided, which can yield single crystals of "low-temperature phases" [43]. This avoids possible twinning and formation of defects in single crystals during cooling, when a phase transition might occur.
However, this method also has clear drawbacks. Depending on the volume of the sealed reaction containers and the temperature the pressure can vary wildly. On one hand this is caused by the vapor pressure of the water. But with filling factors close to 1, the thermal expansion of water also becomes relevant. This is because thermal expansion is much larger close to the boiling or melting point. Therefore, reproducibility is hard to guarantee and can only be achieved by meticulous and precise work.
In this work only an approximate range for the reaction conditions can be given, since each Teflon reaction container had slight geometric differences (deformations during usage contributed to this).

1.8.3 Chemical transport reactions

If solid state and hydrothermal synthesis are understood as reactions in the solid and liquid phase, chemical transport reactions fulfill the third roll of "gaseous synthesis". The method is often applied in ampoules, which are sealed fused silica tubes containing the reactants and a transport agent. The aim is to partially gasify the reactants and intermediates by heating the evacuated ampoules. From the gaseous phase, reactions and possibly recrystallizations occur, which can yield single crystalline material suited to structure solution by single crystal XRD. Similarly to hydrothermal synthesis, a

transport agent such as $PtCl_2$ or I_2 helps convert the reactants into gaseous intermediates.
Chemical transport aiming at synthesizing oxidotellurates can be done with a I_2 mineralizer. First, the reactant and a small amount of I_2 (in the % range) are mixed and ground. This mixture is filled into a fused silica ampoule, which is then evacuated. The ampoule is placed into a two zone furnace, which is comprised of two zones with different temperatures. The products form either on the cold or hot side of the ampoule (depending on whether the overall reaction is exo- or endothermic) and can be harvested after the ampoule is removed from the oven.
In the example just discussed TeO_2 and I_2 can form TeI_2 and O_2 as volatile intermediates. These intermediates react with each other and other intermediates as well as reactants. In the course of the reaction, already formed crystals of the desired product can be reintroduced into the gas phase, which favours the formation of larger single crystals over nanocrystallites.
In many cases this pathway results in large single crystals where other synthesis methods fail, due to the low activation energy of the reactions in stark contrast to most solid state reactions. Also, the reactions do not rely on solubility in water such as in hydrothermal synthesis nor diffusion processes in solid phase. Moreover, compounds that are not stable under air can be prepared.
One of the clear disadvantages of chemical transport synthesis, however, is the effort needed to prepare the experiments. To produce the fused silica ampoules, an oxyhydrogen torch is needed. Moreover, a vacuum pump setup with suitable glassware for evacuation is necessary. In comparison, hydrothermal synthesis is relatively simple, since all that is needed is a suitable oven and autoclaves with inlays. All in all, chemical transport gives a work intensive alternative to hydrothermal and some simple solid state synthesis pathways, which can yield unique and useful results. Finally, the review given by Gruehn and Glaum [44] gives a comprehensive overview of the topic with further information.

2 Methods

In this chapter the various employed experimental methods are discussed in detail. First, an overview on the synthesis strategy and planning is given. This is followed by a summary of the different synthesis methods with the concrete approaches and reaction conditions.

2.1 Heuristic methods and planning

During our attempted synthesis of honeycomb tellurates, especially at the early stages, we ran into a number of practical challenges. In this section the process of our work and some of these challenges are described. The initial motivation for the further study of honeycomb tellurates came from a paper published by Masese et al. [24], who presented novel K honeycomb tellurates including $K_2Ni_2TeO_6$ and investigated their suitability as battery materials.
Therefore, we started our work trying to expand on the already existing research done by Masese et al. as well as that done by Evstigneeva et al. [36] on $Na_2M_2TeO_6$ honeycomb tellurates. Our first avenues of research went into substitution of the alkali A and the transition metal M atoms. At the beginning, we concentrated on the question whether $Rb_2M_2TeO_6$ and $Cs_2M_2TeO_6$ honeycomb tellurates could be synthesized. Furthermore, we designed and executed preliminary experiments to gauge whether divalent Mg, Ca, Mn, Fe, Co, Ni, Cu, Zn and Cd, among others, were candidates for further M substitution. And if these substitutions would yield novel honeycomb tellurates (some of these were already reported in phases such as $K_2Mg_2TeO_6$ [24] or $Na_2Co_2TeO_6$ [36]).
Since our first and foremost method of analysis was single crystal XRD, it was necessary to grow single crystals of suitable size (>30 µm radius) and quality (e.g. few faults, little mosaicity and similar factors). However, initial experiments on the substitution of the various M candidates as well as Rb and Cs failed in yielding novel honeycomb tellurate single crystals. As such, the primary source of structural information for these experiments was powder XRD (including non-ambient powder analysis). Since these measurements were only of routine quality (well suited for qualitative analysis of known phases), structure solution from powder data was unfeasible. In the course of our work we learned, that there are some telltales for the presence of $A_2M_2TeO_6$ honeycomb tellurates from powder data. Because the layered $[(M,Te)O_2)]$ structure and the layer-layer distances are highly predictable for $A_2M_2TeO_6$ honeycomb tellurates, the presence of the 002 and 004 reflections at around 13-16° 2Θ and 26-32° 2Θ in the powder diffractogram hints at the presence of honeycomb tellurates. These layers contain the Te (and M) atoms with high atomic numbers, causing these reflections to have generally high intensity. Additionally, preferred orientation of crystals in the stacking direction 001 can further amplify the relative intensity of these reflections. This makes them a very good practical guideline. Examples can be seen in figure 9 which shows some example powder XRD measurements of various samples containing honeycomb tellurates. With this methodology we achieved a rough overview on which system of reactants was promising and planned our further experiments accordingly. This was done by varying the parameters of the synthesis such as temperature, heating duration, reactant ratios and crucible material. Some novel phases were obtained serependipitously, others were synthesized in quality sufficient for single crystal XRD by repeated experiments. The details for the synthesis conditions are given in the following sections, as well as in the results section starting from page 29.
Another important factor to consider is hygroscopy. $A_2M_2TeO_6$ honeycomb tellurates tend to be hygroscopic, as was also discussed by Masese et al. [24]. This warrants proper storage of samples under vacuum or dry inert gas in a desiccator. However, oftentimes the more pressing problem is the

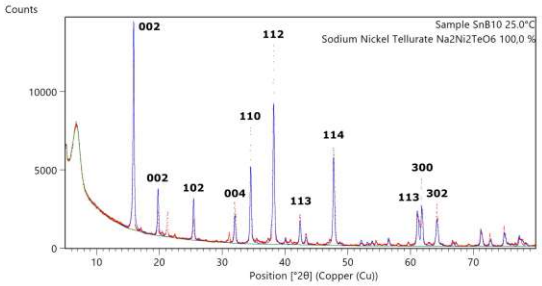

(a) Rietveld fit of the sample SnB10, containing $Na_2Ni_2TeO_6$ showing some unexplained reflections.

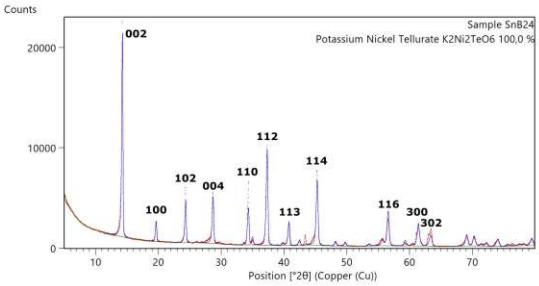

(b) Rietveld fit of the sample SnB24, containing single phase $K_2Ni_2TeO_6$.

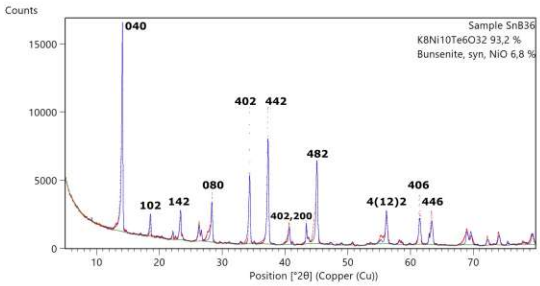

(c) Rietveld fit for a powder XRD measurement of the sample SnB36, containing multiple unknown phases and also $K_4Ni_5Te_3O_{16}$.

Figure 9: Rietveld fits for samples SnB10 and SnB24 (above) as well as SnB36 (below) containing $Na_2Ni_2TeO_6$, $K_2Ni_2TeO_6$ and $K_4Ni_5Te_3O_{16}$, respectively.

hygroscopy of unwanted side products or intermediates such as K_2TeO_4 and especially Rb_2TeO_4. As will be discussed in the results, section 3.3.5 on page 43, K_2TeO_4 and Rb_2TeO_4 form as intermediates and sometimes side products in honeycomb tellurate synthesis. This leads to great practical difficulties, since both phases are highly hygroscopic and even deliquescent. Powder XRD measurements are heavily affected by this, since reliable results are sometimes only obtainable when working under an inert gas atmosphere.
Adding to this, samples containing Rb_2TeO_4 feature reflections in similar positions as the 002 and 004 honeycomb tellurate reflections. Unfortunately, this feigns the presence of novel honeycomb tellurates ($Rb_2M_2TeO_6$). This may be caused by the formation of unknown Rb_2TeO_4 hydrates or other kinds of tellurates. There is however no clear evidence for that, as of yet.
TEM imaging and optical microscopy showed that $A_2M_2TeO_6$ honeycomb tellurates ($K_2Ni_2TeO_6$, $Na_2Ni_2TeO_6$, $K_2Co_2TeO_6$) and related honeycomb phases form hexagonal plates. From our experience, the powder XRD measurements also generally show a strong preferred crystal orientation in the 001 direction. Rietveld refinement with a fitting March-Dollase factor can model this preferred crystal orientation satisfactorily. However, as will be shown later, $A_2M_2TeO_6$ honeycomb tellurates also often show one-dimensional diffuse scattering. This can lead to an weakening of the intensity of reflections in the powder diffractograms. The preferred orientation and diffuse scattering complicate Rietveld refinements. Single crystal structure refinement or alternative methods such as TEM analysis are useful in avoiding these problems.

2.2 Synthesis Methods

2.2.1 Solid-state Synthesis overview

Different salts of alkali metals (e.g. K_2CO_3), transition and earth alkali metals (e.g. NiO and $CaCO_3$) and tellurium compounds (TeO_2 or $Te(OH)_6$) were mixed. All of the reactants were obtained commercially except for the M_3TeO_6 ortho-oxidotellurates(VI). These were obtained via a solid-state synthesis route adopting and modifying procedures known from literature such as [45] for Co_3TeO_6 and Mn_3TeO_6 or [46] for Cu_3TeO_6. The reactant mixture was homogenized and ground with an agate mortar and pestle. Depending on the sample it was also pressed into a pellet with a hydraulic press.
Following this preparation, the samples were heated at temperatures ranging from 500–900°C, in corundum, platinum, MgO ceramic, porcelain or fused silica crucibles. Samples prepared using the solid-state synthesis were abbreviated with **SnBX** or **SX** (X= $1, 2, ...$). SnB stands for "Shake'n'bake" and S for "Saltflux" referring to solid state synthesis in a flux.

A flux material was added to some samples, which also took the role of supplying alkali-metal ions. This was done by adding an excess of KCl, KBr, RbBr or CsCl to the other reactants and heating the mixture in the oven above the melting point of the flux material.

2.2.2 Hydrothermal Synthesis overview

The reactant mixtures were weighed into PTFE inlays which were filled with water to filling factors of 60–80 %. In order to achieve strongly alkaline conditions, an excess of alkali hydroxide (NaOH, KOH, RbOH or CsOH) was added as a mineralizer.
The PTFE inlays were placed in steel autoclaves (pictured in figure 10) and heated at 210°C for a duration ranging 3–21 days. Accordingly, the pressure conditions ranged roughly from 19 to around 60 bar. The exact pressure is hard to estimate, since every vessel has a slightly differenty geometry; the vapor pressure of water at 210°C is about 19 bar.
After the procedure, the supernate was discarded and the samples washed twice with water and twice with isopropanol. Ultimately, the samples were dried in air, in a warm environment (30–40°C). The samples were labelled with **HTX** (X= $1, 2, ...$), abbreviated from "**H**ydro**T**hermal".

2.2.3 Synthesis in ampoules

Samples were roughly mixed with a mineralizer, then sealed in evacuated fused silica glass ampoules. The ampoules were heated in a two zone furnace, with temperatures of 700 and 770°C on each side, respectively. For this preparation method, the samples were placed such that no chemical transport occured, which was the lower temperature end.
After removing the ampoules from the oven, they were cut open with a diamond blade and the contents were quickly transferred into glass containers and stored in an dessicator under vacuum. Ampoule synthesis was only investigated for the Rb-Ni-Te-O system with three different transport agents (I_2, $HgBr_2$ and $PtCl_2$). Ampoule samples were labelled **AX** (X= $1, 2, ...$).

Figure 10: A steel autoclave (left) and an oven (right) used for hydrothermal synthesis.

2.3 Reaction conditions

2.3.1 Honeycomb tellurate synthesis conditions

The synthesis of $A_2M_2TeO_6$ and other honeycomb tellurates was attempted via all four synthesis routes that were mentioned above in section 2.2. Generally, either A_2CO_3 or ANO_3 was mixed with MO or $M(NO_3)_2$ and TeO_2. In reactions utilizing flux, ACl or ABr was substituted as an alkali atom A source. Reaction equivalents were based on the ideal reactions

$$A_2CO_3 + 2MO + TeO_2 + {}^1/_2O_2 \xrightarrow{700\text{–}850°C} A_2M_2TeO6 + CO_2,$$
$$2ANO_3 + 2MO + TeO_2 + {}^1/_2O_2 \xrightarrow{700\text{–}850°C} A_2M_2TeO6 + yNO_z.$$

Table 1 gives a summary of the reaction conditions for most successful solid state synthesis experiments.

Table 1: Reaction conditions of the honeycomb tellurate experiments. Sample names, reaction equivalents, crucible materials, maximal oven temperature T_{max} and time t at that temperature are given.

Sample	**TeO_2**	**$NiCO_3$**	**$NaNO_3$**	**Crucible**	**T_{max} [K]**	**t [h]**
1f	1	2	2	Corundum	700	30 h

Sample	**TeO_2**	**KNO_3**	**$NiNO_3$ $.6H_2O$**	**Crucible**	**T_{max} [K]**	**t [h]**
SnB11	1	2	2	Corundum	700	30 h
SnB24	1	2	2	Corundum	850	11 d

Sample	**TeO_2**	**Rb_2CO_3**	**$NiNO_3$ $.6H_2O$**	**Crucible**	**T_{max} [K]**	**t [h]**
SnB49	1	1	2	Corundum	700	30 h

Sample	**TeO_2**	**K_2CO_3**	**KNO_3**	**NiO**	**Crucible**	**T_{max} [K]**	**t [h]**
SnB29	1		2	2	Si plate	900	24 h
SnB31	1	1		2	Si plate	860	24 h
SnB35	1	1		2	Platinum	800	15 d
SnB36	1		2	2	Platinum	800	15 d

Table 2: Reaction conditions for unsuccessful honeycomb tellurate synthesis attempts. Sample names, reaction equivalents, crucible materials, maximal oven temperature T_{max} and time t at that temperature are given.

Sample	**$Te(OH)_6$**	**$NiNO_3$ $.6H_2O$**	**Ni_3TeO_6**	**KBr**	**KOH**	**t [d]**
HT21	1	2			7	6
HT22	1	2			7	6
HT59	2		2	6		10
HT60	1		2		7	10
HT66	1		2		6	3

Sample	**$Te(OH)_6$**	**$NiNO_3$ $.6H_2O$**	**KBr**	**Crucible**	**T_{max} [K]**	**t [h]**
S29	2	2	10	Corundum	710	28

2.3.2 Rb and Cs reaction mixtures

The suitability of different divalent transition metals M (Cu, Fe, Mn, Ni, Cd, Co, Zn and Mg) for honeycomb tellurate synthesis was investigated. Different candidates for the alkali atoms A were tested as well (K, Rb and Cs; Na to a lesser degree). Table 4 shows the reaction conditions of various samples containing Rb. In table 3 similar data is given for the experiments utilizing Cs.

Table 3: Reaction conditions for unsuccessful Cs honeycomb tellurate synthesis attempts. Sample names, reaction equivalents, crucible materials, maximal oven temperature T_{max} and time t at that temperature are given.

Sample	**x =**	**x**	**$Te(OH)_6$**	**Cs_2CO_3**	**CsOH**	**t [d]**
HT5	CuO	2	1	3		3
HT6	CuO	2	1	3		3
HT11	Fe_2O_3	1	1		7	4
HT12	Fe_2O_3	1	1		7	4
HT17	MnO	2	1		6	4
HT18	MnO	2	1		6	4
HT25	$Ni(NO_3)_2.6H_2O$	2	1		7	6
HT26	$Ni(NO_3)_2.6H_2O$	2	1		7	6
HT35	$Cd(NO_3)_2.4H_2O$	2	1		7	11
HT36	$Cd(NO_3)_2.4H_2O$	2	1		7	11
HT41	$(CoCO_3)_2(Co(OH)_2)_3$	0.4	1		7	11
HT42	$(CoCO_3)_2(Co(OH)_2)_3$	0.4	1		7	11
HT47	$Zn(NO_3)_2.6H_2O$	2	1		7	7
HT48	$Zn(NO_3)_2.6H_2O$	2	1		7	7
HT51	CuO	2	1	1		13
HT52	CuO	2	1	1		13

Sample	**x =**	**x**	**TeO_2**	**$Te(OH)_6$**	**Cs_2CO_3**	**NiO**	**Crucible**	**T_{max} [K]**	**t [h]**
SnB6			1		1	2	Corundum	750	12
SnB7				1	1	2	Corundum	750	12
SnB23	CuO	2		1	1		Corundum	850	30
SnB69	Ni_3TeO_6	2	1		3		Corundum	750	12

Sample	**M =**	**MCl_2**	**x =**	**x**	**$Te(OH)_6$**	**CsCl**	**Crucible**	**T_{max} [K]**	**t [h]**
S3	Cu	2			2	20	Corundum	800	5
S6	Zn	2			2	20	Corundum	800	5
S7	Mg	2			2	20	Corundum	800	5
S15	Cd		Cd_3TeO_6	1		20	Corundum	820	3
S27	Ni		$Ni(NO_3)_2.6H_2O$	2	1	4	Corundum	730	20
S34	Ca	2			2	10	Corundum	820	5

Table 4: Reaction conditions for unsuccessful Rb honeycomb tellurate synthesis attempts. Sample names, reaction equivalents, crucible materials, maximal oven temperature T_{max} and time t at that temperature are given. "Tr. Agent" stands for transport agent. * = $RbNO_3$ was used instead of Rb_2CO_3.

Sample	**x =**	**x**	**$Te(OH)_6$**	**RbOH**	**t [d]**
HT3	CuO	2	1	6	3
HT4	CuO	2	1	6	3
HT9	Fe_2O_3	1	1	7	4
HT10	Fe_2O_3	1	1	7	4
HT15	MnO	2	1	6	4
HT16	MnO	2	1	6	4
HT23	$Ni(NO_3)_2.6H_2O$	2	1	7	6
HT24	$Ni(NO_3)_2.6H_2O$	2	1	7	6
HT33	$Cd(NO_3)_2.4H_2O$	2	1	7	11
HT34	$Cd(NO_3)_2.4H_2O$	2	1	7	11
HT39	$(CoCO_3)_2(Co(OH)_2)_3$	0.4	1	7	11
HT40	$(CoCO_3)_2(Co(OH)_2)_3$	0.4	1	7	11
HT45	$Zn(NO_3)_2.6H_2O$	2	1	7	7
HT46	$Zn(NO_3)_2.6H_2O$	2	1	7	7
HT58	Ni_3TeO_6	2	1	7	10

Sample	**$Te(OH)_6$**	**NiO**	**$NiNO_3.6H_2O$**	**RbBr**	**Crucible**	**T_{max} [K]**	**t [h]**
S26	1	4	2	4	Corundum	730	20
S30	2	10	2	10	Corundum	710	28
S31	1	10	2	10	Corundum	710	28

Sample	**x =**	**x**	**TeO_2**	**$Te(OH)_6$**	**Rb_2CO_3**	**Crucible**	**T_{max} [K]**	**t [h]**
SnB4	NiO	2	1		1	Corundum	750	12
SnB5	NiO	2		1	1	Corundum	750	12
SnB12	$Ni(NO_3)_2.6H_2O$	2	1		1	Corundum	700	30
SnB21	$Zn(NO_3)_2.6H_2O$	2	1		1	Corundum	850	55
SnB22	CuO	2		1	1	Corundum	850	30
SnB25	$Ni(NO_3)_2.6H_2O$	2	1		1	Corundum	850	260
SnB26	CuO	2	1		1	Corundum	700	260
SnB33	CuO	2		1	1	Corundum	470	550
SnB34	CuO	2	1		2*	Corundum	470	550
SnB41	Ni_3TeO_6	2	1		3	Corundum	750	30
SnB43	Ni_3TeO_6	2	1		3	Corundum	700	18
SnB49	$Ni(NO_3)_2.6H_2O$	2	1		1	Corundum	700	30
SnB66	Co_3TeO_6	2	3		3	Platinum	700	6
SnB74	Ni_3TeO_6	2	1		3	Platinum	700	18

Sample	**Precursor**	**$m_{pre.}$ [mg]**	**Tr. Agent**	**$m_{t.A.}$ [mg]**	**T_{low} [K]**	**T_{high} [K]**	**t [h]**
A1	SnB49	157	I_2	21.0	700	770	650
A2	SnB49	153.3	$PtCl_2$	17.6	700	770	650
A3	SnB49	157	$HgBr_2$	24.0	700	770	650

2.3.3 Synthesis of $K_{5.5}Co_{14.5}Te_6O_{36}$ and $K_{4.67}Cd_{15.67}Te_6O_{36}$

Both $K_{5.5}Co_{14.5}Te_6O_{36}$ and $K_{4.67}Cd_{15.67}Te_6O_{36}$ were obtained as singular results from solid state synthesis, respectively in samples SnB75 and SnB28. Both samples were prepared similarly by mixing the dry reactants and heating them in a crucible under air.
Sample SnB75 yielded $K_{5.5}Co_{14.5}Te_6O_{36}$ and was synthesized by reacting $(Co_{0.93}Ni_{0.07})C_2O_4.2H_2O$ with TeO_2 in a 1:3 molar ratio (1.716 g and 5.9 g) at 820°C for 10 h in a porcelain crucible. This synthesis was originally aimed at investigating the $(Co_{0.93}Ni_{0.07})TeO_6$ system, see also section 2.3.7 on page 25. $K_{5.5}Co_{14.5}Te_6O_{36}$ was obtained as a minor phase in sample SnB75.
Sample SnB28 containing $K_{4.67}Cd_{15.67}Te_6O_{36}$ was prepared by mixing $Cd(NO_3)_2.4H_2O$, TeO_2 and K_2CO_3 in a 1:1:2 molar ratio (0.1 g, 0.087 g and 0.387 g) and heating the mixture in a corundum crucible at 850°C for 7 days. The remaining product was single phase, yellow $K_{4.67}Cd_{15.67}Te_6O_{36}$.

2.3.4 Synthesis of $CaCu_2TeO_6$ and $Ca_3Cu_3Te_2O_{12}$

$CaCu_2TeO_6$ and $Ca_3Cu_3Te_2O_{12}$ were synthesized under very similar conditions. $CaCu_2TeO_6$ was obtained by heating sample HT3 to 1100°C for 20 min, which yielded $H_4Rb_4Cu_2Te_2O_{14}$ by hydrothermal synthesis and is described in detail on page 26 in section 2.3.8.
$Ca_3Cu_3Te_2O_{12}$ on the other hand was prepared in multiple solid-state synthesis experiments with varying levels of purity. The reaction conditions for the experiments which produced $Ca_3Cu_3Te_2O_{12}$ are summarized in table 5.

Table 5: Reaction conditions of the $Ca_3Cu_3Te_2O_{12}$ experiments. Sample names, reaction equivalents, phase fraction of $Ca_3Cu_3Te_2O_{12}$, crucible materials, maximal oven temperature T_{max} and time t at that temperature are given.

Sample	TeO_2	CuO	$Ca(NO_3)_2.4H_2O$	Frac. [%]	Crucible	T_{max} [K]	t [h]
SnB14	1	2	1	86	Corundum	850	24
SnB15	1	1	2	66	Corundum	850	24
SnB16	1	2	1	66	Corundum	850	24

2.3.5 Synthesis of $Ca_2Te_2O_7$

Single crystals of $Ca_2Te_2O_7$ were obtained via solid state synthesis with flux (NaCl and $CaCl_2$). $Te(OH)_6$, $CaCl_2.6H_2O$ and NaCl were mixed in a molar ratio of 1:0.6:10 (0.196 g, 0.091 g, 0.5 g) in powder form and ground in an agate mortar. The reaction was done in a corundum crucible, at a maximum temperature of 820°C, which was held for 5 h. Following that, the sample was cooled with gradient of 100°C/h down to 200°C and quenched in air. The sample contained $Ca_2Te_2O_7$ only as a minor phase, a structure solution was done using colorless $Ca_2Te_2O_7$ crystalline needles (with prevalent twinning).

2.3.6 Synthesis of $Ca_2TeO_3Cl_2$ and $Ca_5Te_4O_{12}Cl_2$

Initially, $Ca_5Te_4O_{12}Cl_2$ was obtained via solid-state synthesis starting from $Te(OH)_6$, $CaCl_2.6H_2O$ and CsCl (flux) in sample S11. While $Ca_5Te_4O_{12}Cl_2$ was single phase in this sample, the experiment failed to yield the same result upon repetition.
The samples were prepared by mixing the reagents in dry form and grinding the mixture in an agate mortar. Afterwards the homogenized powder was filled in a crucible and fired under air atmosphere. The reaction conditions are summarized in tables 6 and 7.

Table 6: Reaction conditions of the $Ca_2TeO_3Cl_2$ experiments. Sample names, reaction equivalents, phase fraction of $Ca_2TeO_3Cl_2$, crucible materials, maximal oven temperature T_{max} and time t at that temperature are given.

Sample	**$Te(OH)_6$**	**$CaCl_2.6H_2O$**	**CsCl**	**Frac. [%]**	**Crucible**	**T_{max} [K]**	**t [h]**
S11	1	0.6	5	100	Corundum	820	5
Sample	**TeO_2**	**$CaCl_2.6H_2O$**	**$Ca(NO_3)_2$ $.4H_2O$**	**Frac. [%]**	**Crucible**	**T_{max} [K]**	**t [h]**
SnB59	1	1.5	1	5	Corundum	820	5
Sample	**TeO_2**	**$CaCl_2.6H_2O$**	**$CaCO_3$**	**Frac. [%]**	**Crucible**	**T_{max} [K]**	**t [h]**
SnB62	1	0.72	1	52	fused silica	820	5
SnB63	1	2	1	3	fused silica	800	4
SnB64	1	1	1	53	fused silica	800	4

Table 7: Reaction conditions of the $Ca_2TeO_3Cl_2$ experiments. Sample names, reaction equivalents, phase fraction of $Ca_2TeO_3Cl_2$, crucible materials, maximal oven temperature T_{max} and time t at that temperature are given.

Sample	**TeO_2**	**$CaCl_2.6H_2O$**	**$Ca(NO_3)_2$ $.4H_2O$**	**Frac. [%]**	**Crucible**	**T_{max} [K]**	**t [h]**
SnB59	1	1.5	1	14	Corundum	820	5
Sample	**TeO_2**	**$CaCl_2.6H_2O$**	**$CaCO_3$**	**Frac. [%]**	**Crucible**	**T_{max} [K]**	**t [h]**
SnB61	1	1.5	1	50	Platinum	820	5
SnB63	1	2	1	53	fused silica	800	4

2.3.7 Synthesis of $(Co_{0.93}Ni_{0.07})TeO_6$

The synthesis of the $(Co_{0.93}Ni_{0.07})_3TeO_6$ was achieved inadvertently in sample SnB48, when employing $Co(C_2O_4).2H_2O$ contaminated with around 7%$_{wt}$ Ni relative to Co. Initially, this reaction was intended to yield the known ortho-tellurate Co_3TeO_6 instead.
To reproduce the result obtained in sample SnB48 further experiments were done with the contaminated $(Co_{0.93}Ni_{0.07})(C_2O_4).2H_2O$ and pure $Co(C_2O_4).2H_2O$ as well as Co_3O_4 as a pure Co source. All the reaction conditions are summarized in table 8, while the respective phase fractions of each sample are given in table 9.

Table 8: Reaction conditions of the $(Co_{0.93}Ni_{0.07})_3TeO_6$ experiments. Sample names, reaction equivalents, crucible materials, maximal oven temperature T_{max} and time t at that temperature are given.

Sample	**TeO_2**	**$Co(C_2O_4).2H_2O$**	**$(Co_{0.93}Ni_{0.07})(C_2O_4).2H_2O$**	**Crucible**	**T_{max} [K]**	**t [h]**
SnB48	2	3		Porcelain	820	12 h x2
SnB50	1	3		Platinum	820	12 h
SnB71	1		3	Platinum	750	12 h

Sample	**TeO_2**	**NiO**	**$Ni(NO_3)_2.6H_2O$**	**Co_3O_4**	**Crucible**	**T_{max} [K]**	**t [h]**
SnB51	1			1	Porcelain	820	12 h
SnB52	1			1	Porcelain	820	12 h
SnB54	1	0.15		0.95	Platinum	820	12 h
SnB73	1		0.3	0.9	Platinum	820	12 h
SnB76	1		0.15	0.95	Platinum	820	12 h

Table 9: Phase fractions in $(Co_{0.93}Ni_{0.07})_3TeO_6$ experiment samples. Fractions of monoclinic m-$(Co_{0.93}Ni_{0.07})_3TeO_6$, orthorhombic o-Co_3TeO_6 and NiO are given. * = unknown phases present in sample.

Sample	**m-Co_3TeO_6**	**o-$(Co_{0.93}Ni_{0.07})_3TeO_6$**	**Target phase**
SnB48		100	Co_3TeO_6
SnB50		100	$(Co_{0.93}Ni_{0.07})_3TeO_6$
SnB51	100		Co_3TeO_6
SnB52	100		Co_3TeO_6
SnB54	71.1	28.1	$(Co_{0.93}Ni_{0.07})_3TeO_6$
SnB71	100		Co_3TeO_6
SnB73		100.0*	$(Co_{0.93}Ni_{0.07})_3TeO_6$
SnB76	10.6	89.4	$(Co_{0.93}Ni_{0.07})_3TeO_6$

2.3.8 Synthesis of $H_4Rb_4Cu_2Te_2O_{14}$

$H_4Rb_4Cu_2Te_2O_{14}$ was obtained by hydrothermal synthesis at 210°C. CuO, $Te(OH)_6$ and an aqueous (50 $\%_{wt}$) RbOH solution were mixed and filled up with deionized water to a filling factor of about 0.7 in a PTFE inlay in sample HT3. The molar ratios for CuO, $Te(OH)_6$ and (50 $_{wt}\%$) RbOH were 1:2:6 (reactant weights: 0.239 g:0.187 g:1.001 g). After mixing, the PTFE inlay was sealed in a steel autoclave and heated for 72 h at 210°C. Finally, the sample was washed with water twice and again with isopropanol two more times. Then it was left to dry. Aside from $H_4Rb_4Cu_2Te_2O_{14}$, another major constituent of the reaction product was CuO.

2.3.9 Synthesis of $H_6K_3FeTe_2O_{12}$ and $H_4K_3FeTe_2O_{11}$

$H_6K_3FeTe_2O_{12}$ was prepared via hydrothermal synthesis in sample HT8. $H_4K_3FeTe_2O_{11}$ was subsequently obtained by heating a $H_6K_3FeTe_2O_{12}$ single crystal on the single crystal diffractometer. A mixture of microcrystalline $H_6K_3FeTe_2O_{12}$ and $H_6K_3FeTe_2O_{12}$ single crystals were obtained by mixing $Te(OH)_6$, $FeSO_4 \cdot {}_7H_2O$ and KOH in a molar ratio of 1:2:6 in a PTFE inlay. The container was filled with deionized water to a filling factor of about 0.75 and heated at 210°C in a steel autoclave for 3 days. Sample preparation of sample HT8 and washing was done as described in section 2.2.2 on page 18. $H_6K_3FeTe_2O_{12}$ was obtained as a single phase and single crystals were present in the sample as pale yellow to colorless needle to plates.

2.4 Instruments and analytical methods

The synthesized compounds were analyzed mainly with XRD methods and XRF. TEM and SAED were employed to analyze selected samples. Generally, samples were first examined via ambient PXRD under air. SAED was performed with a TEM, which was carried out using facilities at the University Service Centre for Transmission Electron Microscopy, Vienna University of Technology, Austria. This also yielded high resolution depictions of the sample grains.
To determine the structure of unknown compounds, single crystal diffraction was performed, whenever suitable crystals could be found with a polarizing microscope. Some reactions were monitored by non-ambient in-situ PXRD, in order to determine intermediate reaction products. To determine the presence of impurities which are hard to evidence by XRD, such as Ni in Co compounds, XRF was employed for some samples. We do not show the XRF data here, it was however useful in guiding further analysis, which is why we mention it at this point.

2.4.1 Powder Diffraction Phase and Semi Quantitative Rietveld Analysis

Phase analysis via ambient PXRD was performed for all samples. For this, samples were ground to a fine powder in an agate mortar and mounted on Si plates cut in the 711 direction. Small amounts of vaseline were used to affix the powder samples to the support.
The diffractograms were evaluated with the HighScore Malvern Panalytical program. A search-match algorithm was used to match the background corrected measurement with the PDF® (ICDD Powder Diffraction File™) database entries. Sources for the crystal structures for phase analysis and Rietveld fits were the single crystal structure entries from the ICSD (Inorganic Crystal Structure Database, FIZ Karlsruhe) as well as the .cif files of our novel crystal strucures.
Following the phase identification, a standard Rietveld fit was performed which also yielded semi-quantitative phase ratios. Depending on the sample, the texture was modelled usually using the

March-Dollase model for preferred crystal orientation and rarely by expansion into spherical harmonics. The peak form was modelled using a Pseudo-Voigt function with asymmetrical width and form. FWHM (full width half maximum) was adjusted according to the Caglioti formula

$$H = \sqrt{U \tan \Theta^2 + V \tan \Theta + W},$$

where the W and V parameters were refined (U was set to 0). We show many powder diffractograms that were measured for the novel structures in the results, from page 29 on, and the appendix starting from page 86. Where important for the discussion we show relevant indexed reflections.

2.4.2 Single Crystal Diffraction Analysis

In samples where single crystals of suitable size could be synthesized, single crystal diffraction was performed on unknown phases. The samples were transferred to a glass microscope slide and covered with Fomblin® PFPE lubricant. They were examined under an polarizing microscope. If suitable crystals could be found, they were isolated via a needle. Afterwards they were harvested with a MicroLoop LD™ crystal holder and mounted onto the diffractometer sample holder.
In the following, the procedure of measurements using the Apex program and the Kappa Apex II diffractometer is outlined.
Measurements consisted of a matrix-run in which the unit cell of the crystal was determined. For this, the Apex program measured predetermined parts of reciprocal space automatically and tried to match the identified reflections to a unit cell.
The Bravais lattice was determined after the unit cell. The proper measurement was optimized by Apex using the estimated point group of the crystal. Frame data was collected in multiple runs and reduced to individiual intensity values for the assigned reflections.
Then, corrections for absorption effects using the multi-scan method, the determination of the space group and finally the structure solution were performed. The structural solution and the following refinement of the structure were performed in ShelXle.
Likewise, the procedure with the STOE Stadivari diffractometer was very similar. Here, the refinement was performed in Olex2 [47], which integrates SHELXL [48] as well as other refinement and structure solution programs.

2.5 Instrumentation

2.5.1 Powder Diffraction Diffractometers

Three different diffractometers were used for the PXRD measurements. Of these, two are X'Pert Panalytical devices, one of which is the X'Pert Pro model. Both of these instruments were operated with Cu K_α radiation (1.54056 Å) at 45 kV and 40 mA in Bregg-Brentano configuration. Non-ambient PXRD measurements were performed with the X'Pert Pro device. Additionally, a third diffractometer was used to make PXRD measurements of samples that exhibited fluorescence under Cu K_α radiation, which utilized Cr K_α radiation instead.

2.5.2 Single Crystal Diffractometers

The single crystal diffraction measurements were performed using two different instruments. Firstly, a Bruker Kappa Apex II with a custom cooling setup, which can cool down to 100 K was utilized. It has a four-axis κ-goniometer and a Mo X-ray source. Measurements with the Kappa Apex II

were always done with a generator Voltage of 45 kV and a current of 40 mA.
Additionally, a STOE Stadivari diffractometer was used, which also had a quarter Eulerian cradle, but possessed both Cu and Mo radiation micro-sources. The STOE Stadivari diffractometer was used with different settings for the two radiation microsources; the Cu K_α beam was generated with 50 kV and 1.0 mA and the Mo K_α beam was generated with 60 kV and 0.83 mA.

2.6 Structure modelling and simulation

Various programs were used for the simulation and the structure solution from single crystal XRD measurements. Additionally to Olex and ShelXle and their integrated algorithms, PLATON [49] was employed in order to check the integrity of the produced structure models. Depictions and structural images were created with the program DIAMOND [50].

3 Results and Discussion

This chapter presents the results we obtained starting off by giving a overview over the crystal structures and measurement parameters for single crystal XRD measurements in section 3.1 on page 29. Also, the cell parameters obtained by Rietveld fitting for the phases are listed alongside the ones obtained from integration of single crystal XRD intensity data. Various practical challenges and the viability of synthesis routes are detailed in section 3.2 on page 31. Afterwards, novel honeycomb tellurates (including $K_4Ni_5Te_3O_{16}$) are discussed and a rough description of the reaction sequence is discussed in section 3.3 starting from page 32. This was done by in-situ monitoring a solid state honeycomb tellurate synthesis and observing the formation of intermediates and products. Following that, two novel hexagonal oxidotellurates(VI) $K_{14/3}Cd_{47/3}Te_6O_{36}$ and $K_{5.5}Co_{14.5}Te_6O_{36}$, showing K channels and occupational disorder, are presented in section 3.4 on page 46 and the following pages. Next, various other novel oxidotellurate and oxidotellurate-chloride crystal structures are presented in section 3.5 and multiple subsections starting from page 52 - see also the contents on page IV. Finally the chapter closes by discussing results that demonstrate the limits of substitutions for M and A components in $A_2M_2TeO_6$ honeycomb tellurates, namely such substitutions that did not yield novel phases. This is done in section 3.6 starting from page 73.
All the crystal structures presented here have supplemental information in the form of atom positions, ADPs and powder diffractograms as well as distance and angle tables where the data is relevant. This supplemental data can be found in the appendix 8 from page 86 onward under the respective subsections. Moreover, the reaction conditions for each phase can be found in the Methods section 2.3 starting from page 19.

3.1 Overview of results

We report twelve novel crystal structures of various oxidotellurates and oxidotellurate-chlorides. Most of the structures were obtained by solid state synthesis, details for each phase can be found in section 2.3 on page 19. A summary of important information relating to the structure solution and refinement by single crystal XRD are found in table 11. Table 10 shows the cell parameters obtained by Rietveld analysis of the investigated samples. Sample labels can be cross referenced between tables 10 and 11. Other results, especially the powder XRD diffractograms or SAED images and diffraction images, are presented in the discussion of each phase.

Table 10: Overview of the cell parameters of the novel phases, obtained by Rietveld refinement.

Sample	a [Å]	b [Å]	c [Å]	α[°]	β[°]	γ[°]	V [Å^3]
HT4	9.4777(8)	6.4773(6)	12.4478(7)	90	91.0401(12)	90	764.048(15)
HT8	14.1297(15)	14.9160(4)	5.9776(5)	90	114.9884(18)	90	1141.90(3)
SnB16	7.34115(9)	7.34115(9)	8.65666(2)	90	90	90	466.529(2)
SnB28	9.9433(3)	9.9433(3)	9.7643(2)	90	90	120	836.048(4)
SnB36	12.084(4)	25.267(3)	10.462(3)	90	90	90	3194.22(25)
SnB50	10.3800(1)	8.61375(9)	19.8305(2)	90	90	90	1773.02(3)
SnB61	6.6905(2)	6.7401(2)	8.1104(3)	66.7601(5)	67.8821(5)	82.0556(6)	311.308(4)
SnB64	17.1240(2)	18.2654(1)	11.246(1)	90	90	90	3510.77(11)
SnB75	9.3446(8)	9.3446(8)	8.9652(13)	90	90	120	677.98(4)

Table 11: Overview of key crystallographic data (SG short for space group type) of the newly reported structures.

Sum form.	$K_4Ni_5Te_3O_{16}$	$(Co_{0.9}Ni_{0.1})_{14.5}K_{5.5}Te_6O_{36}$	$K_{4.67}Cd_{15.67}Te_6O_{36}$	$Ca_2Te_2O_7$	$Ca_3Cu_3Te_2O_{12}$	$CaCu_2TeO_6$
a [Å]	12.0639(8)	9.3602(6)	9.9157(4)	7.4607(3)	7.3290(4)	9.6555(6)
b [Å]	25.2528(16)	9.3602(6)	9.9157(4)	10.1847(3)	7.3290(4)	7.0316(3)
c [Å]	10.4470(6)	8.9674(5)	9.7371(3)	8.4428(3)	8.6353(5)	6.8627(4)
α[°]	90	90	90	94.446(3)	90	90
β[°]	90	90	90	77.307(3)	90	92.911(5)
γ[°]	90	120	120	100.500(3)	90	90
V [Å^3]	3182.6(3)	680.40(10)	829.10(7)	614.90(4)	463.84(6)	465.33(4)
Z	4	1	1	2	2	2
SG	$Amm2$	$P6_3/m$	$P\bar{3}$	$P\bar{1}$	$P4_2/nnm$	$C2/c$
Color	light green	violet	yellow	colorless	green	yellow
Habitus	hexag. plate	needles	hexag. plates	needles	plate	plate
Crys. size [mm^3]	0.040× 0.025× 0.010	0.075× 0.043× 0.022	0.025× 0.02× 0.005	0.08× 0.03× 0.03	0.05× 0.04× 0.035	0.048× 0.032× 0.01
ρ [g/cm^3]	4.557	5.883	6.411	4.832	5.428	5.578
μ [mm^{-1}]	12.349	15.867	121.625	11.142	14.712	16.337
T [K]	293(2)	293	100	300	300	300
Radiation	Mo K_α	Mo K_α	Cu K_α	Mo K_α	Mo K_α	Mo K_α
***R*(obs)**	0.0612	0.0222	0.0711	0.031	0.0183	0.0168
***wR*(all)**	0.2546	n	0.1252	0.09	0.0412	0.0403
Refl.	4655	1102	1027	42007	640	1115
Refl.(obs)	1919	830	767	26413	344	896
Parameters	211	54	98	202	32	51
Riet. Sample	SnB36	SnB75	SnB28		SnB16	
Notes			tiny crystals	four domain twin		

Sum form.	$Ca_5Te_4O_{12}Cl_2$	$Ca_2TeO_3Cl_2$	$(Co_{0.93}Ni_{0.07})_3TeO_6$	$H_6K_3FeTe_2O_{12}$	$H_4K_3FeTe_2O_{11}$	$H_{16}Rb_8Cu_4Te_4O_{28}$
a [Å]	17.1142(4)	6.6855(13)	10.3819(3)	14.1306(7)	14.0888(6)	9.4781(6)
b [Å]	18.2830(6)	6.7181(12)	8.6126(2)	14.9042(8)	14.9470(6)	6.4883(4)
c [Å]	11.1879(3)	8.0847(15)	19.8265(5)	5.9782(3)	5.9706(2)	12.4659(8)
α[°]	90	66.645(5)	90	90	90	90
β[°]	90	67.917(5)	90	115.0300(10)	115.027(3)	91.110(2)
γ[°]	90	82.124(6)	90	90	90	90
V [Å^3]	3500.68(17)	308.88(10)	1772.79(8)	1140.80(10)	1139.27(8)	766.47(8)
Z	8	2	16	8	8	2
SG	$Pnma$	$P\bar{1}$	$Pca2_1$	$C2/m$	$C2/m$	Cc
Color	colorless	colorless	violet	pale yellow	pale yellow	dark green
Habitus	needles	plates	needles	plates	plates	plates
Crys. size [mm^3]	0.10× 0.063× 0.040	0.04× 0.04× 0.02	0.2× 0.05× 0.03	0.32× 0.25× 0.12	0.18× 0.08× 0.01	0.13× 0.09× 0.08
ρ [g/cm^3]	3.042	3.512	6.001	3.641	3.547	4.143
μ [mm^{-1}]	5.87	7.248	17.496	7.487	7.486	19.189
T [K]	300	100(2)	298(2)	300(2)	430(5)	296(2)
Radiation	Mo K_α	Mo K_α	Mo K_α	Mo K_α	Mo K_α	Mo K_α
***R*(obs)**	0.0322	0.0372	0.0253	0.0212	0.0385	0.023
***wR*(all)**	0.0808	0.0688	0.0493	0.0491	0.1154	0.0498
Refl.(obs.)	11576	5144	14429	2650	2713	4065
Refl.(all)	7572	4129	12718	2348	2207	3690
Parameters	214	73	363	97	89	113
Riet. Sample	SnB64	SnB61	SnB50	HT8		HT4

3.2 Challenges and viability of the synthesis and preparation routes

Initially, we tried to reproduce the synthesis as given by Masese et al. in [24] for $K_2Ni_2TeO_6$ and other samples. Unfortunately, we did not obtain $K_2Ni_2TeO_6$ reproducibly and therefore investigated different synthesis routes with varying parameters, as described in section 2.2 and 2.3 from page 18 onward. During the synthesis experiments, we encountered some challenges in the handling of precursors, reaction mixtures and products. One such was the hygroscopy of not only the honeycomb tellurates, but also side products such as K_2TeO_4 and Rb_2TeO_4. We side stepped this problem by quenching reaction products from relatively low temperatures in the range of 200–300°C after synthesis and storing them in a desiccator immediately. Performing the synthesis under inert gas atmosphere is not viable, since similar work on honeycomb tellurate synthesis, as done by [24] for example, utilized TeO_2. In this case, oxidizing Te(IV) to Te(VI) via atmospheric oxygen is necessary. We did not investigate possible alterations to the synthesis route in detail, such as preparing TeO_3 as a precursor. Moreover, we do not expect inert gas atmosphere to improve upon the stability of products very much. We argue that the presence of small amounts of water vapor in the air should not influence the reaction greatly, as long as the temperature is reasonably high (above 500°C in our experiments).

From the tested synthesis methods, the solid state method produced honeycomb tellurates most reliably. However, one of the decisive drawbacks of the solid state method is its tendency to produce microcrystalline samples. Some experiments with added flux produced honeycomb tellurate single crystals, notably of $K_4Ni_5Te_3O_{16}$ in sample S21. Following this, we were able evidence the phase in several other samples by Rietveld refinement of powder XRD data, including SnB31 and SnB36. Since $K_4Ni_5Te_3O_{16}$ was previously unknown, but seemed to form readily, we expect the presence of many more unknown honeycomb tellurates in already characterized systems. This is further supported by SAED and TEM analysis on microcrystalline Ni containing honeycomb tellurate samples 1f and SnB35.

A practical issue which we want to note at this point, is the fact, that it is hard to find a suitable crucible material for some of the solid state synthesis experiments. We employed a variety of different materials for these reactions (corundum, fused silica, platinum, porcelain, MgO ceramic), depending on the reaction conditions. Of these, corundum is a very useful crucible material, since it is inexpensive and heat resistant and did not react with the employed chemicals. Corundum crucibles do stain easily however and some compounds can creep up the side of the crucibles easily. Porcelain as well as the MgO ceramic share similar issues as corundum. Platinum crucibles do not show reactant creep and do not stain, but are expensive and can be corroded by halogenide melts. Fused silica has a tendency to form glasses with tellurium compounds. Overall, despite it's price, platinum crucibles appear to be the best choice for solid state synthesis of honeycomb tellurates, unless working with halogenide melts.

The hydrothermal synthesis experiments were not effective at producing $A_2M_2TeO_6$ honeycomb tellurates. Still, a number of other novel oxidotellurates were obtained using this method. The only time honeycomb tellurates were obtained via a hydrothermal synthesis was in systems containing Cu. In fact, the $K_2Cu_2TeO_6$ phase, which has already been found by a colleague and is currently being worked upon, was synthesized via a hydrothermal reaction. Attempts at synthesizing the Rb analogue $Rb_2Cu_2TeO_6$ yielded the novel phase $H_8Rb_4Cu_2Te_2O_{14}$, which is isotypic [51] to $H_8K_4Cu_2Te_2O_{14}$ reported by Effenberg and Tillmanns in 1992 [52].

Attempts at synthesizing Ni-based honeycomb tellurates using the hydrothermal route failed. Most experiments of this category produced essentially amorphous powders, while some contained unreacted Ni_3TeO_6. While hydrothermal synthesis otherwise often resulted in single crystalline products,

these were not the target honeycomb tellurates.
Ultimately, a small number of ampoule synthesis experiments, similar to chemical transport were attempted. The target phase of these experiments was $Rb_2Ni_2TeO_6$, which was unfortunately not obtained.
On a final note, tellurium is an element that forms volatile compounds at high temperatures. $TeCl_4$ and $TeBr_4$ for example evaporate at 394 and 414°C [53] respectively, but the high melting α-TeO_2 can also release significant amounts of vapour when heated >700°C. Loss of tellurium by evaporation is a significant problem in solid state reactions in open containers. A good way to check for this effect is to monitor the mass loss during the reaction. Often a mass loss is expected, when employing carbonates or nitrates as precursors, but it may also come as a surprise. For this reason, we adjusted some reaction ratios from the theoretical equivalents for a number of experiments.

3.3 Novel honeycomb tellurate phases

In this section, novel honeycomb tellurate phases are reported, of which only the crystal structure of $K_4Ni_5Te_3O_{16}$ has been solved satisfactorily. Other novel phases including $Na_{2(x-y)}Ni_xTe_yO_{2(x+y)}$ which shows a new superstructure and at least two distinct $K_{2(x-y)}Ni_xTe_yO_{2(x+y)}$ phases have also been found. However, the crystal structure of these phases could either not be reliably identified with single crystal XRD or single crystals of suitable size were not obtained. Instead, Rietveld fits of powder XRD data as well as TEM images, SAED images and electron diffraction were employed to show that these phases are indeed novel honeycomb tellurates. In the case of an unknown $Na_{2(x-y)}Ni_xTe_yO_{2(x+y)}$ phase a single crystal XRD measurement was done. However, the crystal quality and the diffuse scattering prevented a complete structure determination.
Additionally, we report diffuse one-dimensional scattering of $K_2Ni_2TeO_6$, which corresponds well to the measured diffuse scattering of the unknown $Na_{2(x-y)}Ni_xTe_yO_{2(x+y)}$ and also $Na_2Ni_2TeO_6$.

3.3.1 Crystal structure of $K_4Ni_5Te_3O_{16}$ and novel $K_{2(x-y)}Ni_xTe_yO_{2(x+y)}$ honeycomb tellurates

The novel $K_4Ni_5Te_3O_{16}$ phase was first obtained by solid state synthesis in a KBr flux in sample S21. The crystal structure with the space group $Amm2$ was refined with $Z = 4$ and the cell parameters are $a = 12.0639(8)$ Å, $b = 25.2528(16)$ Å and $c = 10.4470(6)$ Å. Only a poor structure solution was possible, with a value of $R_1[I >= 2\sigma(I)] = 0.0567$ and $wR_2[all] = 0.2268$, 1916 independent observed reflections and 201 parameters. Nevertheless, most of the structural components prove to be crystallographically and chemically sensible. Additionally, the Rietveld fit performed for sample SnB36 for $K_4Ni_5Te_3O_{16}$, shows very good agreement with the single crystal XRD results on the cell parameters: $\widehat{a} = 12.084(4)$ Å, $\widehat{b} = 25.267(3)$ Å and $\widehat{c} = 10.462(3)$ Å. When compared, the cell paremeters obtained by Rietveld fit are slightly larger, but the deviation is <2‰.
After the initial synthesis, this phase was identified in numerous other samples including SnB31 and SnB36. The reaction conditions can be found in section 2.3.1 on page 19. Figure 11 shows the crystal structure of $K_4Ni_5Te_3O_{16}$. It shows great similarity to the known $A_2M_2TeO_6$ honeycomb tellurates such as $K_2Ni_2TeO_6$ in the layered honeycomb buildup.
A major difference lies in the structure of the honeycomb [M/TeO_2] layers themselves, as is depicted in the next figure, 13. The structural $[Te_2O_{12}]^{12-}$ unit is formed within the [Ni/TeO_2] honeycomb layers. This violates the sixfold screw axis and threefold axis, since the units are oriented in the [100] direction in every layer. This forces the descent from hexagonal to orthorhombic symmetry. Tentatively, the structure has been determined with the space group $Amm2$. The crystallographic

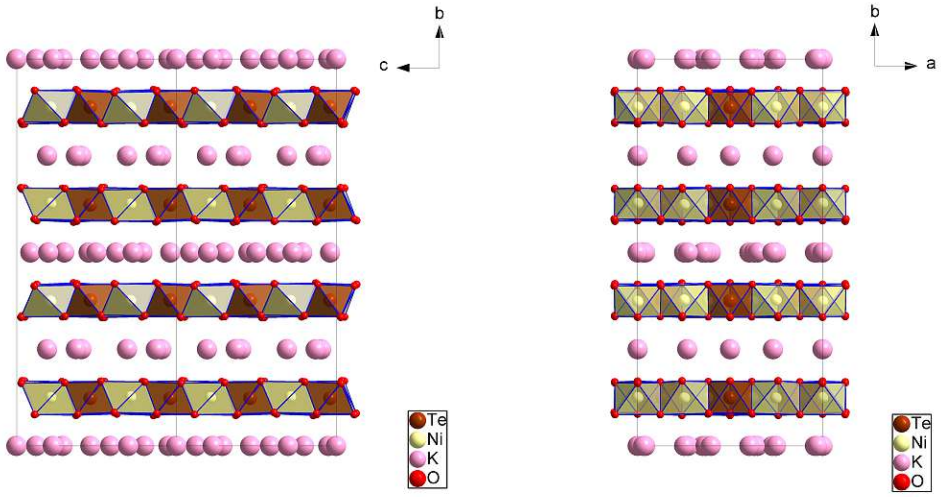

(a) View along the [100] direction.

(b) View along the [001] direction.

Figure 11: Crystal structure of the novel honeycomb tellurate $K_4Ni_5Te_3O_{16}$.

relationship between $K_4Ni_5Te_3O_{16}$ and $K_2Ni_2TeO_6$ can be described by considering the layer group symmetry for the [Ni/TeO_2] honeycomb layers, as was done in section 1.4.1 on page 4 in figure 6b. $K_4Ni_5Te_3O_{16}$ is an order-disorder (short: OD) structure [26]. Besides the [Ni/TeO_2] layers, another crucial point is the arrangement of K atoms in between those layers, namely the presence of occupational disorder and the occupied K atom sites. K shows trigonal prismatic $[KO_6]^{11-}$ coordination in $K_2Ni_2TeO_6$ and the other known hexagonal $K_2M_2TeO_6$ honeycomb tellurates. Therefore, in the [Ni/TeO_2] layers of $K_4Ni_5Te_3O_{16}$ there are a total of 9 different "ideal" K positions that could be occupied. In contrast, $K_2Ni_2TeO_6$ with its higher symmetry has a maximum of 3 unique "ideal" K positions only (one above Ni and Te and one above a gap). This can be seen in figure 13, where the ideal K positions of $K_4Ni_5Te_3O_{16}$ are compared with the two types of K layers $\mathbf{B_1}$ and $\mathbf{B_2}$. Layer $\mathbf{B_1}$ shows complete ordering of K atoms, while $\mathbf{B_2}$ seemingly is a result of overlapping K layers with different arrangements. Unfortunately, no satisfying model was yet found for how these layers might be arranged. However, the ordered $\mathbf{B_1}$ layers show an interesting K ordering: The K-K distance is increased to >3.5 Å in comparison to the 3 Å distances in the disordered $K_2Ni_2TeO_6$ K positions, as given in table 13 in the appendix on page 87. This reduces the K ion repulsion in the structure and suggests that this interaction is a significant destabilizing factor of the phase. Moreover, the "ideal" $K_2Ni_2TeO_6$ structure shows the K position in the center of the trigonal prisms, while K atoms in the $\mathbf{B_1}$ layers of $K_4Ni_5Te_3O_{16}$ are displaced to maximize K-K distances in the layer. This can also be seen in the [Ni/TeO_2] honeycomb layers, as the [Ni/TeO_6] octahedra are actually slightly corrugated. These deviations from the "ideal" $K_2Ni_2TeO_6$ crystal structure suggest that the ionic radius of the K atoms is already large enough to start distorting the structure. This in turn hints at Rb and Cs being too large to form the Rb and Cs honeycomb tellurate analogues. Figure 14 shows powder XRD diffractogramms of both $K_4Ni_5Te_3O_{16}$ and $K_2Ni_2TeO_6$. The similarities of

both Rietveld fits are especially evident in the 2Θ range of ∼14°, ∼28-29° and ∼44° where the most intensive 00$2\underline{n}$ reflections occur. Since the distances between the layers are nearly identical, this is expected. Major differences appear when comparing the "in layer" reflections, where $K_4Ni_5Te_3O_{16}$ shows a number of additional reflections not found in $K_2Ni_2TeO_6$.
Finally, $K_4Ni_5Te_3O_{16}$ also showed one-dimensional diffuse scattering in the reciprocal [001]* direction, as can be seen in figure 12.

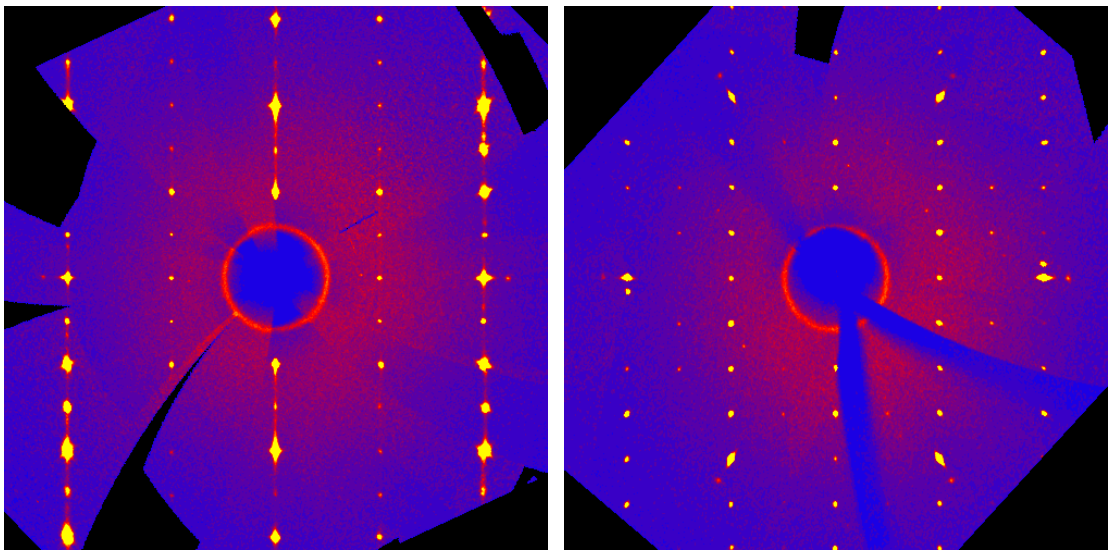

Figure 12: Reciprocal space reconstruction of $K_4Ni_5Te_3O_{16}$ single crystal XRD measurement. Diffuse rods visible in the reciprocal $0kl$ plane (left) which do not appear in the reciprocal $h0l$ plane (right) as expected.

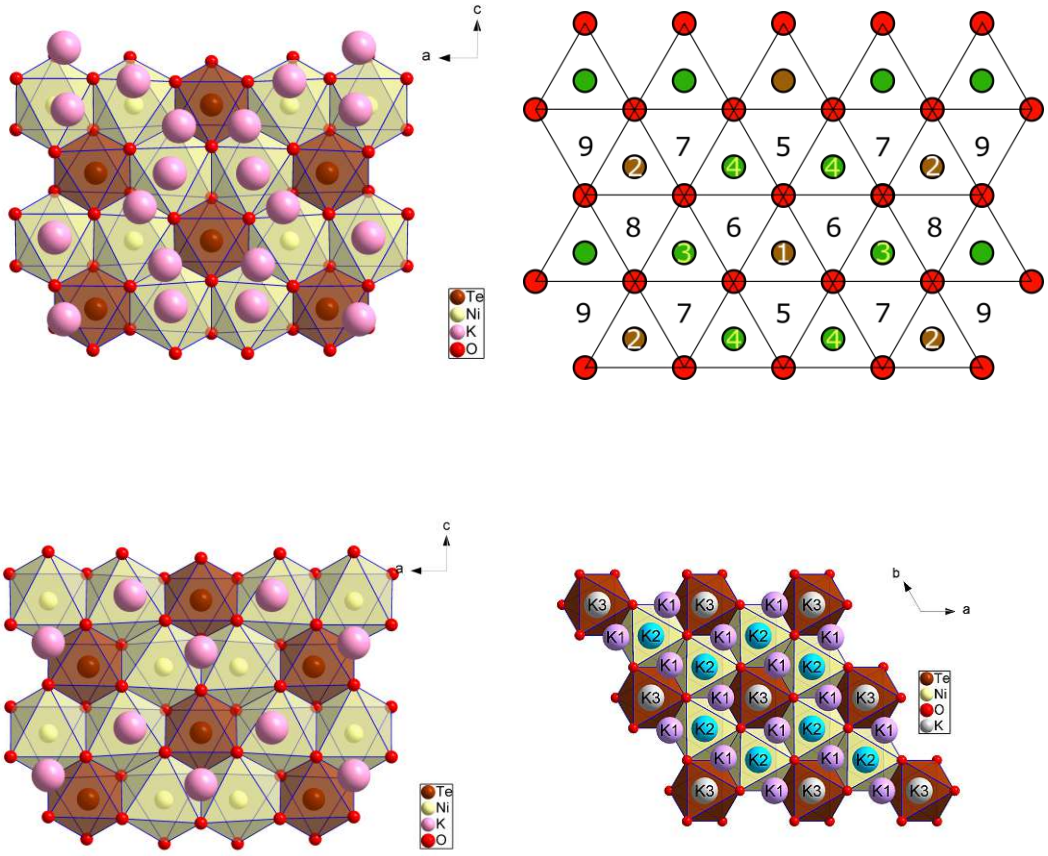

Figure 13: Potassium layer structure of $K_4Ni_5Te_3O_{16}$ (a), (b) and (d) in comparison with the nine possible, ideal horizontal (in the K plane) positions for K atoms (c). In reality, the horizontal placement of K is slightly distorted away from the triangle centres, because of K-K repulsion. This becomes evident when comparing (c) with (d).

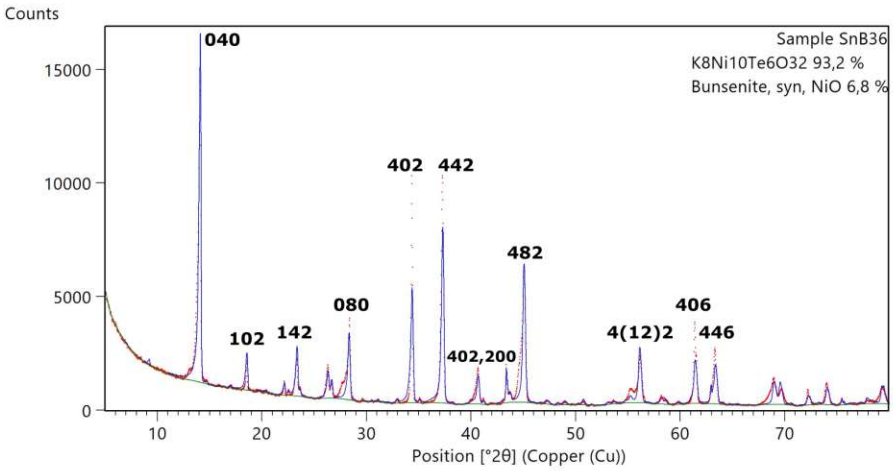

(a) Rietveld fit for sample SnB36, containing mainly $K_4Ni_5Te_3O_{16}$.

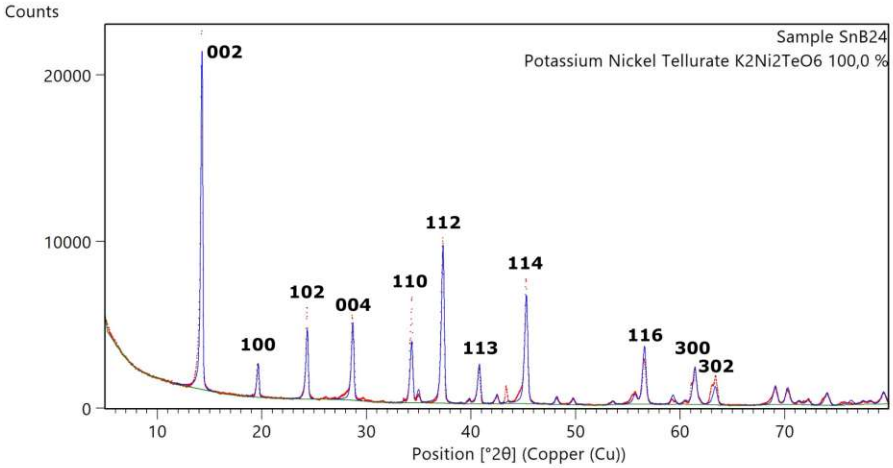

(b) Rietveld fit for sample SnB24, containing phase pure $K_2Ni_2TeO_6$.

Figure 14: Rietveld fits for samples SnB36 (above) and SnB24 (below) containing $K_4Ni_5Te_3O_{16}$ and $K_2Ni_2TeO_6$ respectively.

3.3.2 Diffuse scattering of $K_2Ni_2TeO_6$

The novel phase $K_4Ni_5Te_3O_{16}$, which was described in the previous section, was obtained in combination with the already known $K_2Ni_2TeO_6$ in multiple experiments. Since $Na_2Ni_2TeO_6$ exhibits diffuse scattering caused by stacking faults, $K_2Ni_2TeO_6$ can be expected to behave similarly. Therefore TEM and SAED investigations were performed on $K_2Ni_2TeO_6$, proving not only the anticipated diffuse scattering, but also a few unknown novel $K_{2(x-y)}Ni_xTe_yO_{2(x+y)}$ type phases confirmed via SAED measurement. Unfortunately these phases have as of now not been obtained as single crystals of suitable quality and size for single crystal XRD. Only the cell and the superstructure in relation to the cell of $K_2Ni_2TeO_6$ are known. First the diffuse scattering of $K_2Ni_2TeO_6$ will be discussed.
As can be seen in the depictions in figure 15, the HRTEM image clearly shows the presence of different stacking arrangement with a high stacking fault probability. This is confirmed by the presence of diffuse scattering, as can be seen in 15d and 15e. In contrast to some other $K_{2(x-y)}Ni_xTe_yO_{2(x+y)}$ type phases, the SAED image shows intensity (reflections and diffuse rods) only where the reflections are expected from the $K_2Ni_2TeO_6$ cell, which further confirms the fact that this is a $K_2Ni_2TeO_6$ single crystal ($K_2Ni_2TeO_6$ in the sample was identified initially with powder XRD).

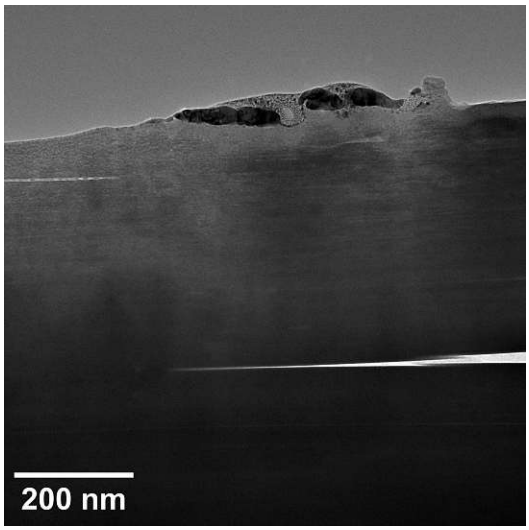

(a) TEM image of single crystal in sample SnB24 cut along the stacking direction.

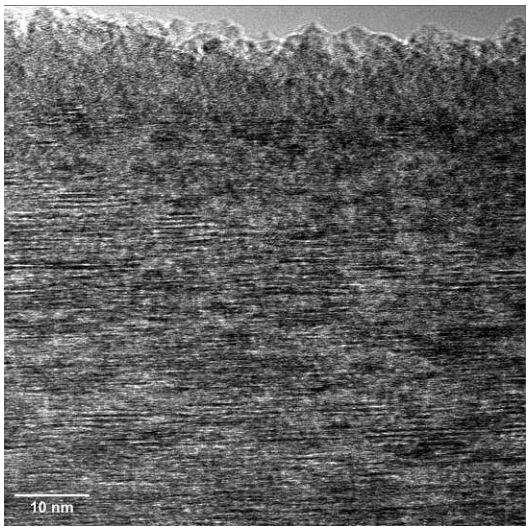

(b) High resolution TEM image showing the prevalence of stacking faults and an amorphous outer layer caused by the sample preparation.

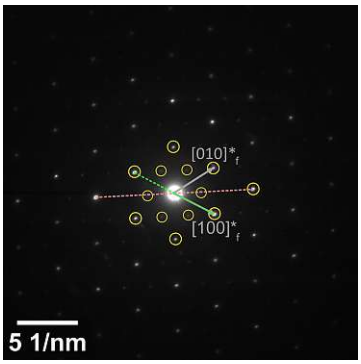

(c) Reciprocal *hk0* plane showing no superstructure "reflections", expected reflections marked in **yellow**. Reciprocal directions shown in 15d and 15e indicated in **pink** and **green**. Family structure reflections labelled in grey.

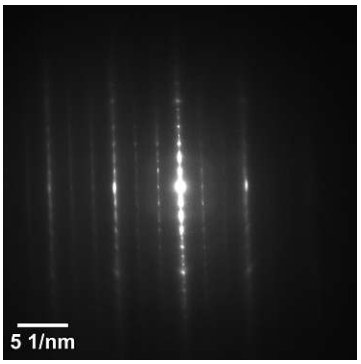

(d) Reciprocal *0kl* plane showing only expected reflections and diffuse rods in the reciprocal c^* direction.

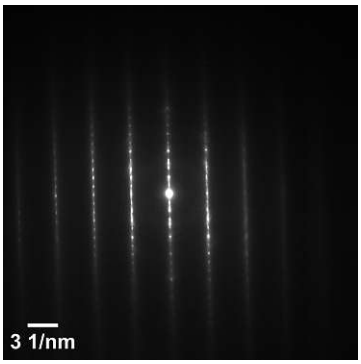

(e) Reciprocal *hhl* plane showing again expected reflections and diffuse scattering.

Figure 15: TEM pictures (above) and SAED diffraction images (below) of a $K_2Ni_2TeO_6$ crystal in sample SnB24.

3.3.3 Novel $Na_{2(x-y)}Ni_xTe_yO_{2(x+y)}$ honeycomb tellurate superstructure exhibiting one-dimensional diffuse scattering

A novel $Na_{2(x-y)}Ni_xTe_yO_{2(x+y)}$ phase was found and analyzed. A satisfying structure refinement was not yet possible. It was obtained via a solid state synthesis which was done at 700°C for 30 h. As figure 16 shows, $Na_2Ni_2TeO_6$ and Ni_3TeO_6 were apparently present in this sample. The Rietveld fit already shows some details of this measurements. At around 28-31° 2Θ an amorphous peak is visible, which can not easily be attributed to any phase. In this same range two very small unassigned reflections can be found as well, which do not belong to any phase in the fit. In fact, there are a few low intensity unassigned reflections, which can either be attributed to a very minor, undetermined phase or interpreted as possible superstructure reflections belonging to $Na_2Ni_2TeO_6$.

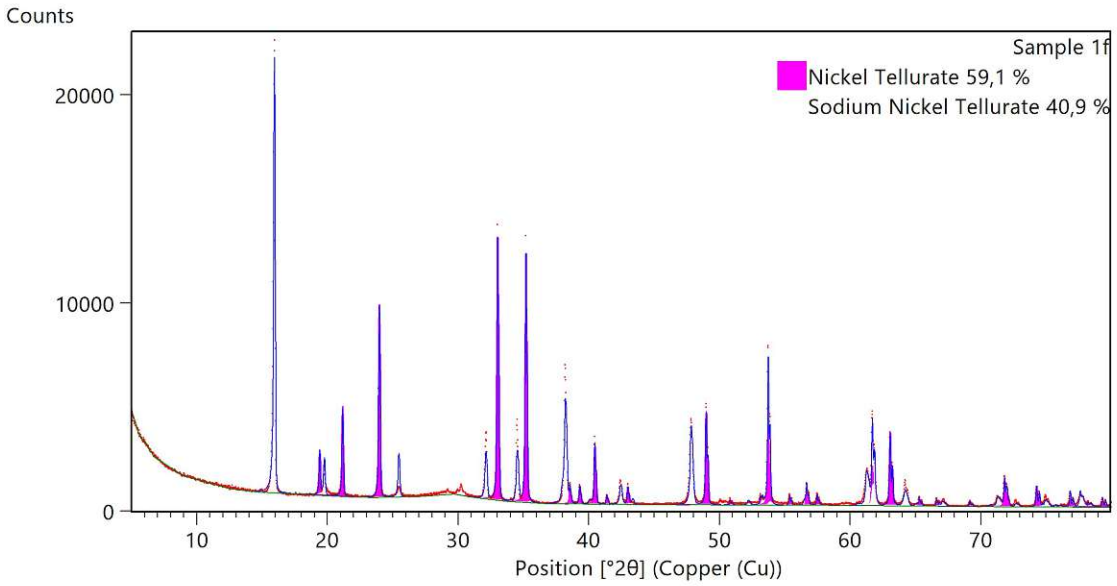

Figure 16: Rietveld fit for $Na_2Ni_2TeO_6$ in sample 1f, containing $Na_2Ni_2TeO_6$ as well as Ni_3TeO_6.

While the crystal structure $Na_2Ni_2TeO_6$ is already known, the single crystal measurement showed interesting additional features, see figure 17. First, diffuse rods were observed originating from the $Na_2Ni_2TeO_6$ cell reflections, which are caused by stacking faults in the $Na_2Ni_2TeO_6$ crystal structure. Diffuse scattering in $Na_2Ni_2TeO_6$ has already been described by [54].
However, additional superstructure diffuse rods were present in reciprocal space marked in **green** in figure 17. These do not correspond to any reflections of the $Na_2Ni_2TeO_6$ cell and instead form a two fold superstructure in the reciprocal a^* and b^* direction. This indicates that this phase is in fact not the already known $Na_2Ni_2TeO_6$ or that this superstructure is a hitherto unknown structural feature occurring in $Na_2Ni_2TeO_6$. The corresponding cell to this novel $Na_{2(x-y)}Ni_xTe_yO_{2(x+y)}$ phase can be formed by simply doubling the $Na_2Ni_2TeO_6$ cell parameters a and b. Alternatively, the crystal may also be twinned and only a single superstructure in either a or b direction may be present. Unfortunately, the quality of the single crystal measurement did not allow for a satisfying

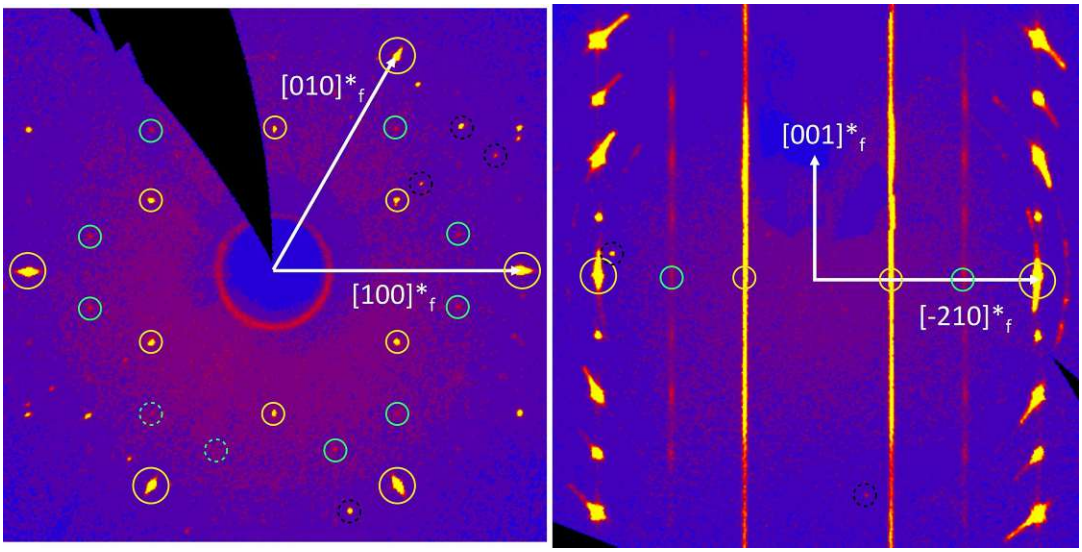

Figure 17: Reciprocal space reconstruction of a $Na_{2(x-y)}Ni_xTe_yO_{2(x+y)}$ from sample 1f. The cell of the family structure is drawn in **white**, reflections/diffuse scattering attributed to a $Na_2Ni_2TeO_6$ cell circled in **yellow** and new superstructure diffuse rods marked in **green**. Some reflections belonging to an unwanted second domain are circled in **black**.

structure solution. This is for one caused by the diffuse scattering, which can not be modelled by standard structure solution programs (this leads to the presence of few sharp reflections, which impedes absorption correction and reduces the number of available reflections for refinement in structure solution). Another factor is the poor crystal quality, which is evident by the family structure reflections indicated by white arrows in figure 17. They show a significant arching. This is likely caused by bending or curling of the single crystalline hexagonal $Na_{2(x-y)}Ni_xTe_yO_{2(x+y)}$ plates.

3.3.4 Novel $K_{2(x-y)}Ni_xTe_yO_{2(x+y)}$ honeycomb tellurates

Besides the novel $K_4Ni_5Te_3O_{16}$ phase, TEM and SAED measurements showed the presence of a novel $K_{2(x-y)}Ni_xTe_yO_{2(x+y)}$ phase, which is closely related to $Na_{2(x-y)}Ni_xTe_yO_{2(x+y)}$ which was described in the previous section. No single crystal XRD data exists of this crystal, the only avaible measurements are SAED diffraction images and TEM images, shown in figure 18. Therefore only the presence of a novel phase can be assumed, and the cell parameters can be inferred.
The crystals are hexagonal plates and the dark field TEM image in 18b hints at defects or twinning. In 18d a SAED diffraction image is visible, which shows a very similar picture to the single crystal XRD measurement of the $Na_{2(x-y)}Ni_xTe_yO_{2(x+y)}$ phase from the previous section. In fact, the superstructure reflections/diffuse rods are located analogous in the reciprocal $hk0$ plane, which suggests a layer structure isotypic to the layer structure of $Na_{2(x-y)}Ni_xTe_yO_{2(x+y)}$. Owing to the limited range of rotation of the instrument, reflections $\mid l \mid > 0$ direction could not be observed. Therefore, the length of the cell parameter c is unknown as well as the presence or absence of diffuse scattering. Since both the investigated $Na_{2(x-y)}Ni_xTe_yO_{2(x+y)}$ and $K_2Ni_2TeO_6$ single crystals showed a similar c parameter and both exhibited diffuse scattering (although to differing degrees), this novel $K_{2(x-y)}Ni_xTe_yO_{2(x+y)}$ phase can be expected to likewise feature stacking faults.

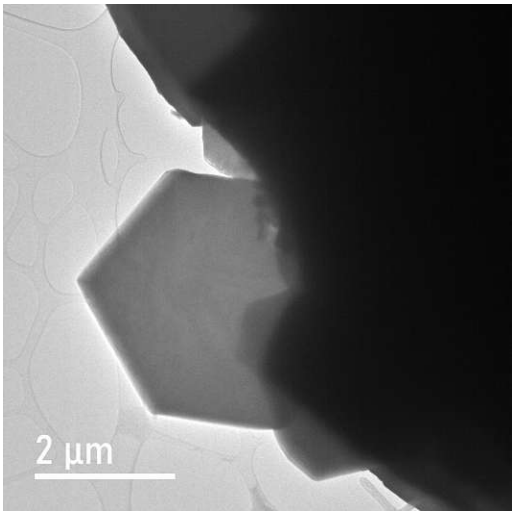

(a) TEM image showing multiple hexagonal $K_{2(x-y)}Ni_xTe_yO_{2(x+y)}$ plates.

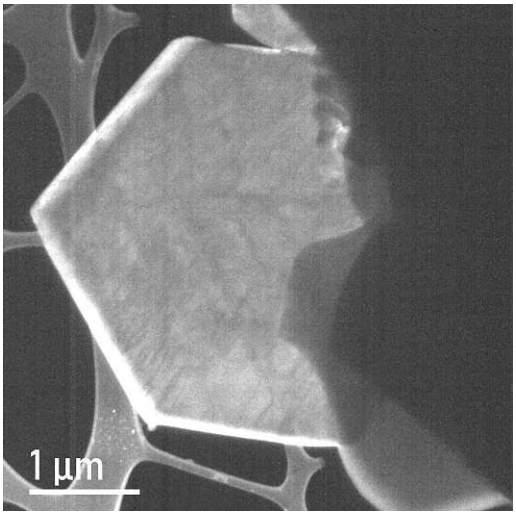

(b) Dark field TEM image TEM image showing the $K_{2(x-y)}Ni_xTe_yO_{2(x+y)}$ plate measured with SAED. Inhomogeneities in the crystal further hint defects in.

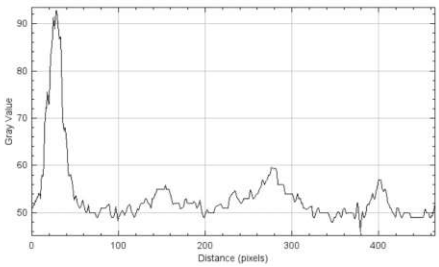

(c) Intensities along a line path of the gray scale SAED image in 18d. The line path is also given in 18d in **pink**. Only two maxima are expected, however the additional two in the middle mark the superstructure reflections/diffuse rods.

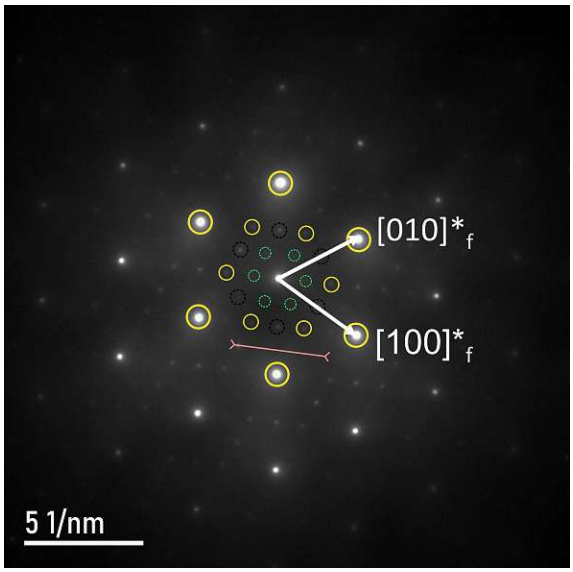

(d) SAED diffraction image of the $K_{2(x-y)}Ni_xTe_yO_{2(x+y)}$ crystal, showing the family structure (**white**), reflections belonging to the $K_2Ni_2TeO_6$ cell (**yellow**) as well as very weak superstructure reflections (**green**). A line plot of the greyscale of the image is given in 18. The crystal was twinned (indicated **black**).

Figure 18: TEM images (above) and SAED diffraction image of a $K_{2(x-y)}Ni_xTe_yO_{2(x+y)}$ crystal in sample SnB35.

3.3.5 Reaction monitoring and thermal behaviour of honeycomb tellurates solid state synthesis using non-ambient powder XRD

To complement the information gained from routine powder XRD measurements reaction monitoring using non-ambient powder XRD was performed. Sample SnB10 containing $Na_2Ni_2TeO_6$ was heated up to 1200°C under air in varying heating steps. The data for this analysis as well as the temperatures for each step are shown in a triperiodic line plot in table 19.
At around 960°C the first big change in crystal structure occurs. $Na_2Ni_2TeO_6$ decomposes itself into NiO and K_2TeO_4. The layered structure itself, indicated by the characteristic 002 reflection at around 16° 2Θ, vanishes after all other reflections. This suggests, that before complete decomposition, extensive disorder and faults occur in the layers themselves, causing reflections such as the 100 reflection to disappear first. Detailed powder diffractograms of sample SnB10 are shown in figure 20. There the effect is even more evident, as in the diffractogram measured at 960°C in 20d only the 002 and 004 reflections are observed.

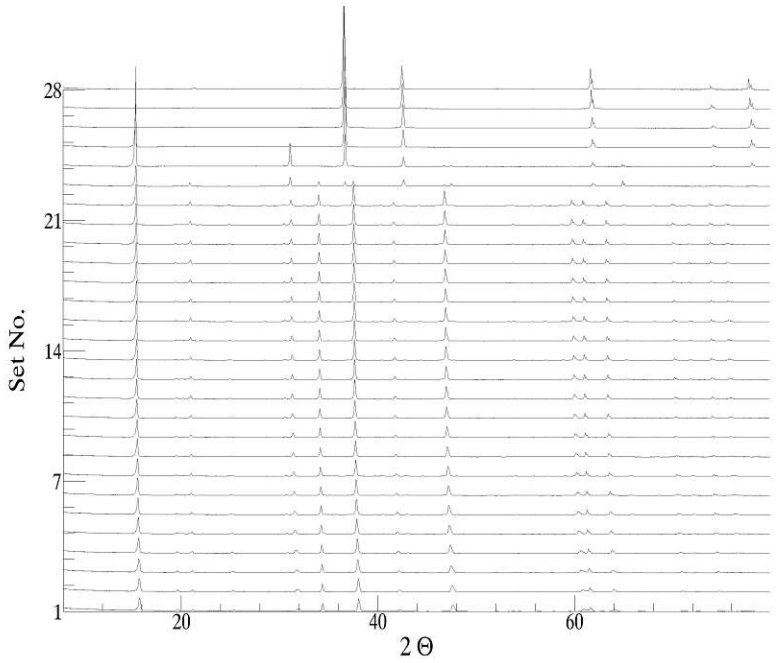

(a) Three-dimensional plot depicting array of non-ambient powder XRD measurements of sample SnB10 containing $Na_2Ni_2TeO_6$.

Scan Nr.	T [°C]
1	25
2	100
3	200
4	300
5	400
6	450
7	500
8	550
9	600
10	650
11	700
12	720
13	740
14	760
15	780
16	800
17	820
18	840
19	860
20	880
21	900
22	920
23	940
24	960
25	980
26	1000
27	1100
28	1200

Figure 19: Three-dimensional plot depicting array of non-ambient powder XRD measurements of sample SnB10 containing $Na_2Ni_2TeO_6$ (left), the sample was heated up to 1200°C under air as given by the temperature table (right).

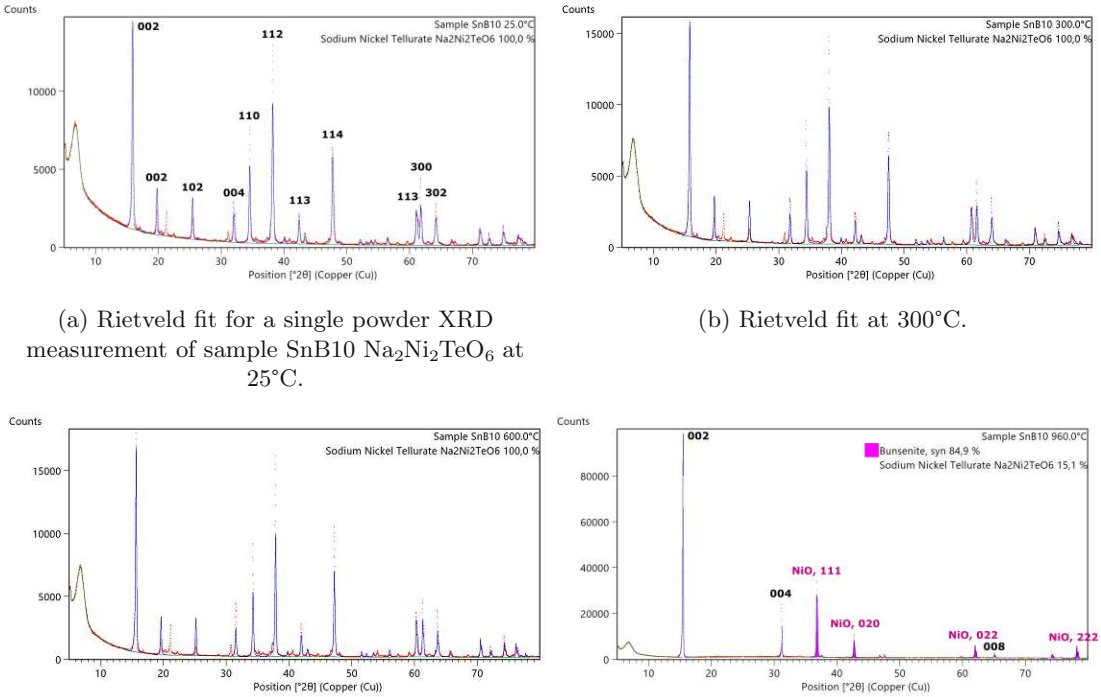

(a) Rietveld fit for a single powder XRD measurement of sample SnB10 $Na_2Ni_2TeO_6$ at 25°C.

(b) Rietveld fit at 300°C.

(c) Rietveld fit at 600°C.

(d) Rietveld fit at 960°C.

Figure 20: Rietveld fit for powder XRD measurements of sample SnB10 containing $Na_2Ni_2TeO_6$ at different temperatures.

To investigate the reaction mechanisms with which $K_2Ni_2TeO_6$ and related K honeycomb tellurates form, non-ambient powder XRD measurements were recorded in air ranging from 25 to 800°C in sample SnB29. The reactants were mixed on the sample holder and reacted in situ while being monitored by powder XRD. The triperiodic line plot and the temperature table for the scans are shown in table **??**.

At around 160°C in scan Nr. 6 the first reaction takes place, which is the decomposition of KNO_3 into KO_x. Next, at around 500°C at scan Nr. 17, the formation of K_2TeO_4 occurs as an important intermediate reaction. This proves that the oxidation of Te(IV) to Te(VI) is not the limiting reaction step. At least for the K-Ni-Te-O system, the reaction of K_2TeO_4 with NiO is the last reaction step, which does not occur until around 600°C. Furthermore, fractions of NiO persist up to around 750°C. Therefore, NiO remains somewhat inert through the reaction and this is an important factor to consider while planning the synthesis of honeycomb tellurates. While no non-ambient reaction monitoring was done for samples aimed at producing $Rb_2M_2TeO_6$ honeycomb tellurates, multiple powder diffractograms in multiple samples showed the presence of Rb_2TeO_4 after the synthesis. This suggests that the formation of A_2TeO_4 is a general intermediary step in the solid state synthesis of honeycomb tellurates. In the case of $Rb_2M_2TeO_6$ honeycomb tellurates, it was likely not only the intermediary, but also the final product, since no $Rb_2M_2TeO_6$ honeycomb tellurate phases could be evidenced.

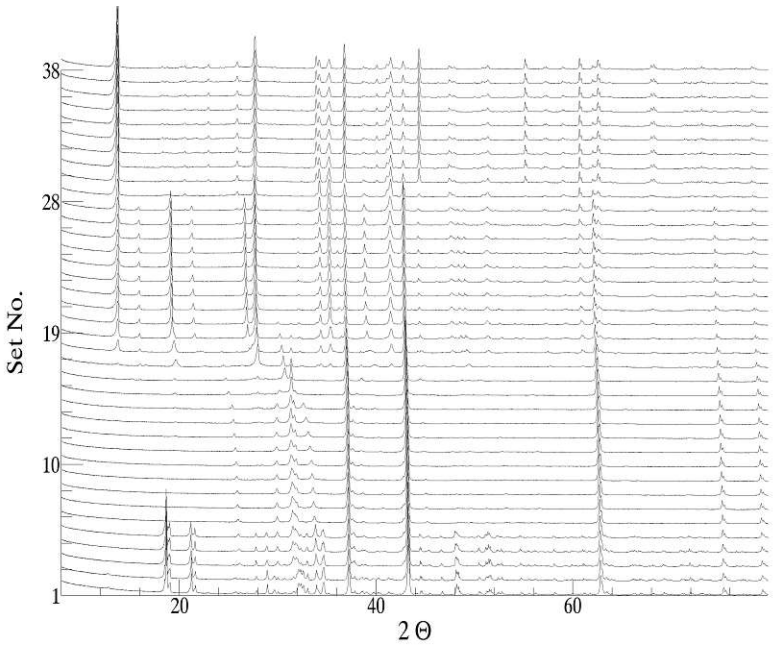

(a) Three-dimensional plot depicting array of non-ambient powder XRD measurements of sample SnB29, which was an synthesis aimed at producing $K_2Ni_2TeO_6$.

Scan Nr.	T [°C]
1	25
2	50
3	75
4	100
5	125
6	150
7	175
8	200
9	225
10	250
11	275
12	300
13	325
14	350
15	400
16	450
17	500
18	550
19	600
20	650
21	670
22	690
23	710
24	730
25	750
26	770
27	790
28	800*
29	800*
30	800*
31	800*
32	800*
33	800*
34	800*
35	800*
36	800*
37	800*
38	800*

Figure 21: Three-dimensional plot depicting array of non-ambient powder XRD measurements of sample SnB29, which was a synthesis aimed at producing $K_2Ni_2TeO_6$ (right), the sample was heated up to 800°C as given by the temperature table (left). *Scans 28-37 were recorded at 800°C and measured in 25 min intervals. *Scan 38 was recorded after heating at 800°C for 1325 min.

3.4 Hexagonal and trigonal channel type oxidotellurates(VI)

3.4.1 Crystal structure of $K_{5.5}(Co_{0.9}Ni_{0.1})_{14.5}Te_6O_{36}$

The crystal structure of $K_{5.5}(Co_{0.9}Ni_{0.1})_{14.5}Te_6O_{36}$ with the hexagonal space group $P6_3/m$ is shown in figure 22. The crystal structure was refined with $Z = 1$ and the cell parameters are $a = b = 9.3602(6)$ Å, $c = 8.9674(5)$ Å, $\gamma = 120°$. A value of $R_1[I >= 2\sigma(I)] = 0.0222$ and $wR_2[all] = 0.0579$ was achieved with 830 independent observed reflections and 54 parameters. A powder XRD measurement and Rietveld fit of sample SnB75 gave the cell parameters of $\widehat{a} = \widehat{b} = 9.3446(8)$ Å, $\widehat{c} = 8.9652(13)$ Å, $\widehat{\gamma} = 120°$ which match the single crystal XRD measurement well.

The $K_{5.5}(Co_{0.9}Ni_{0.1})_{14.5}Te_6O_{36}$ crystals are violet needles prone to twinning and intergrowths. Figure 23 on page 48 shows a SEM image taken of the sample containing $K_{5.5}(Co_{0.9}Ni_{0.1})_{14.5}Te_6O_{36}$ and a mixture of other phases.

$K_{5.5}(Co_{0.9}Ni_{0.1})_{14.5}Te_6O_{36}$ is closely related to $Na_{5.5}Co_{15}Te_6O_{36}$ [55] and $PbMn_2Ni_6Te_3O_{18}$ [56]. The structure is built of a network of TeO_6^{6-} and CoO_6^{10-} octahedra and perforated by two kinds of channels along the [001] direction. One channel contains solely trigonal prismatical $[KO_6]^{11-}$ units, while the other shows similar coordination with occupational disorder of Co and K. In the diffraction image, no superstructure reflections were observed, confirming the occupational disorder.

In the light of electroneutrality, there needs to be some Co(III) present in the phase, so a more correct formula would be $K_{5.5}(Co_{0.9}Ni_{0.11})_{13}Co(III)_{1.5}Te_6O_{36}$. Alternative methods such as XPS measurements confirming the existance of Co(III) have not yet been performed. Another complication is the fact that ca. 10% of the Co atoms are substituted by Ni as evidenced by EDX measurements. This is due to the fact that the reactants contained a mixture of Co_3O_4 and NiO. The sample was actually aimed at reproducing the solid solution $(Co_{0.93}Ni_{0.07})_3TeO_6$ which will be discussed later. Because routine single crystal XRD can not distinguish Ni and Co, whether there is some kind of ordering of Ni and Co is unknown. Further experiments with Ni free reactants are planned to confirm whether $K_{5.5}Co_{14.5}Te_6O_{36}$ also is stable without Ni substitution.

Moreover, figure 24 on page 48 shows the coordination of the mixed (K,Co) positions. The mixed positions actually show a geometry similar to the trigonal prismatic $[KO_6]^{11-}$ coordination with three additional oxygen atoms located further away, resulting in a triple capped prism.

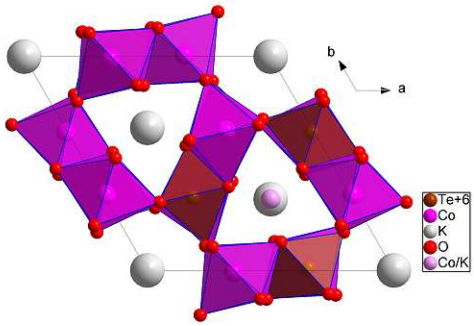

(a) View along the [001] direction with $[TeO_6]^{6-}$ and $[CoO_6]^{10-}$ octahedra network.

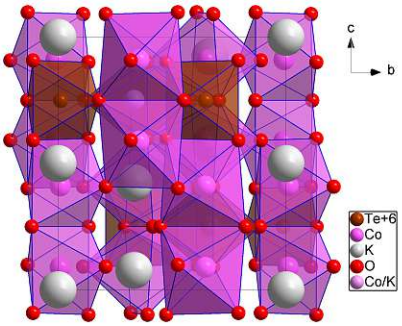

(b) View along the [100] direction with $[TeO_6]^{6-}$ and $[CoO_6]^{10-}$ octahedra network.

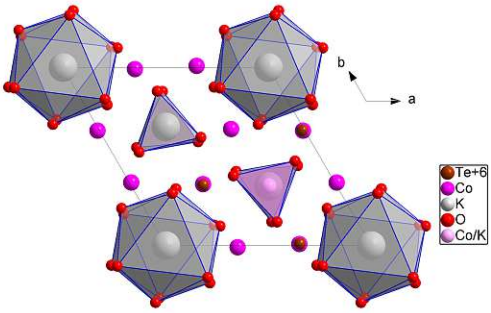

(c) View along the [001] direction with coordination polyhedra of the K and (K,Co) channels.

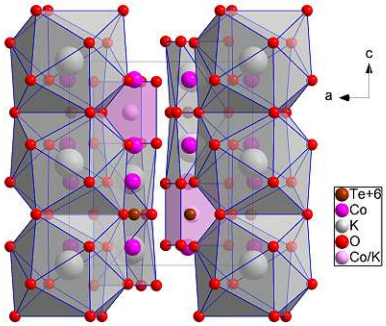

(d) View along the [100] direction with coordination polyhedra of the K and (K,Co) channels.

Figure 22: Above: Crystal structure of $K_{5.5}(Co_{0.9}Ni_{0.1})_{14.5}Te_6O_{36}$ with $[TeO_6]^{6-}$ and $[CoO_6]^{10-}$ octahedra network. Below: K and (K,Co) coordination polyhedra, which are located in the two distinct kinds of channels between the $[TeO_6]^{6-}$ and $[CoO_6]^{10-}$ network.

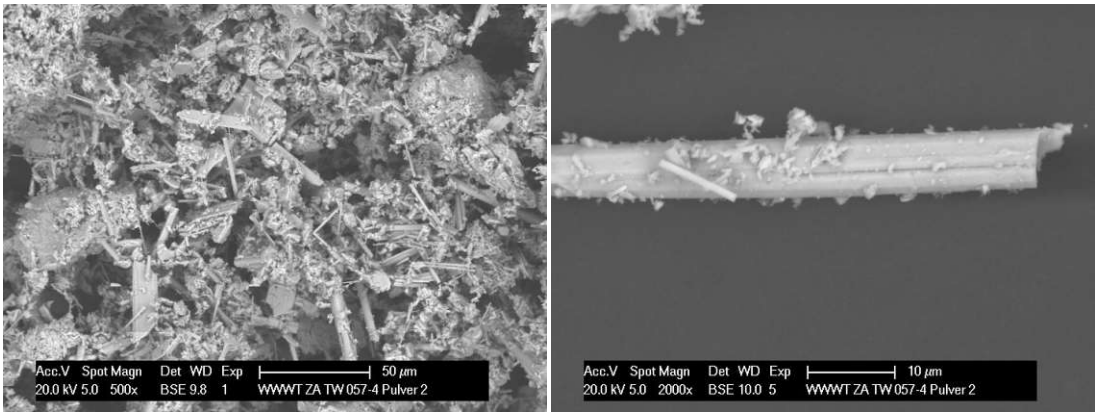

Figure 23: SEM images of $K_{5.5}Co_{14.5}Te_6O_{36}$ grains. EDX measurements were taken in these areas as well.

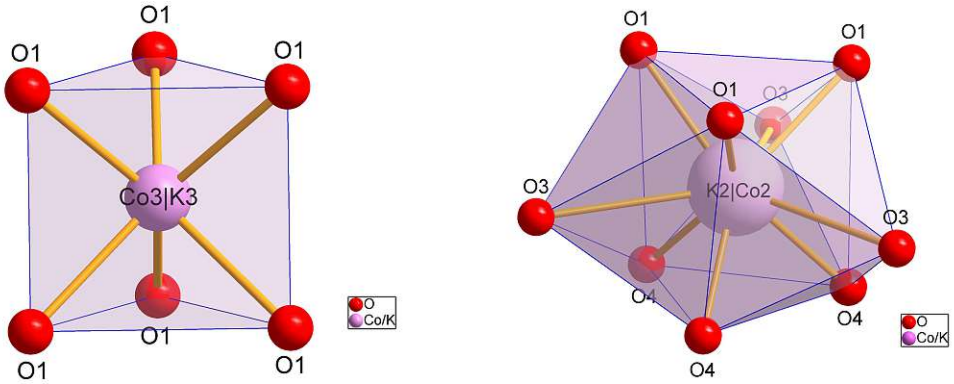

(a) (Co3,K3) $[(Co_3,K_3)O_6]$ trigonal prismatic coordination geometry.

(b) (K2,Co2) $[(K_2,Co_2)O_9]$ tripple capped trigonal prismatic coordination geometry.

Figure 24: Coordination geometry of the mixed occupany K,Co sites in $K_{5.5}Co_{14.5}Te_6O_{36}$.

3.4.2 Crystal structure of $K_{14/3}Cd_{47/3}Te_6O_{36}$

$K_{14/3}Cd_{47/3}Te_6O_{36}$ crystallizes in the spacegroup of $P\bar{3}$ which is a maximal subgroup of the $P6/m$ symmetry of $K_{5.5}Co_{14.5}Te_6O_{36}$. The crystal structure was refined with $Z = 1$ and the cell parameters are $a = b = 9.9157(4)$ Å, $c = 9.7371(3)$ Å, $\gamma = 120°$. A value of $R_1[I >= 2\sigma(I)] = 0.0711$ and $wR_2[all] = 0.1252$ was achieved with 767 independent observed reflections and 98 parameters. The refinement and structure solution was impeded by the extremely small crystal size <30 µm. Figure 25 shows SEM images of the $K_{14/3}Cd_{47/3}Te_6O_{36}$ crystals, illustrating the crystal size. This is problematic in single crystal XRD since the intensity of the diffracted x-rays depends greatly on the crystal volume. Therefore we employed Cu K_α radiation instead of the routine Mo K_α to make use of the higher intensity output by Cu x-ray tubes. This resulted in a satisfying structure solution. A powder XRD measurement and Rietveld fit of sample SnB28 gave the cell parameters of $\widehat{a} = \widehat{b} = 9.9433(3)$ Å, $\widehat{c} = 9.7643(2)$ Å, $\widehat{\gamma} = 120°$. These values are slightly larger than the single crystal XRD cell determination at 100 K. However, this is expected owing to thermal contraction (powder XRD measurements were taken at room-temperature).
Interestingly, the crystal structure of $K_{14/3}Cd_{47/3}Te_6O_{36}$ as shown in figure 26, is of the same structure type as $K_{5.5}Co_{14.5}Te_6O_{36}$, with clear cell parameter differences as well as the symmetry reduction to $P\bar{3}$. All non O atoms stay very close to their relative positions in the cell, even though the coordination of Cd differs significantly from the corresponding coordination of Co in $K_{5.5}Co_{14.5}Te_6O_{36}$. This difference is evident when comparing figures 24 and 27 showing the coordination geometries in both $K_{5.5}Co_{14.5}Te_6O_{36}$ and $K_{14/3}Cd_{47/3}Te_6O_{36}$. This is quite remarkable, because the symmetry is broken by the distortion of the whole network. While the relative coordinates are very similar, the distances in $K_{14/3}Cd_{47/3}Te_6O_{36}$ are stretched disproportionately in the c direction.
The apparent positional K disorder could be due to a composite structure [57], where the K channels and the rest of the network possess different periodicity or an incommensurate structure. However, no unindexed reflections were noted in the reciprocal space reconstructions (or diffraction images), possibly owing to the small crystal size. Another possibility could be, that this degree of K disorder is simply present in the structure as such. One argument for this case is the fact, that while the c-axis has been elongated by around 0.9 Å in comparison $K_{5.5}(Co_{0.9}Ni_{0.1})_{14.5}Te_6O_{36}$, the number of atomic positions in the main Te-Cd network remains unchanged. The three K positions, which are present in $K_{5.5}(Co_{0.9}Ni_{0.1})_{14.5}Te_6O_{36}$ possibly split into multiple, partially occupied K positions.

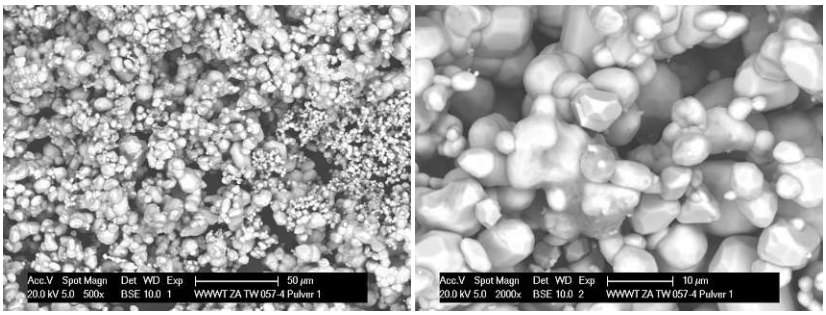

Figure 25: SEM pictures of $K_{14/3}Cd_{47/3}Te_6O_{36}$ grains from sample SnB29.

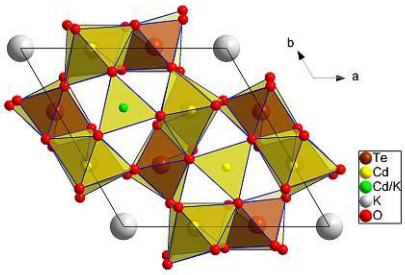

(a) View along the [001] direction with $[TeO_6]^{6-}$ and $[CdO_6]$ octahedra network.

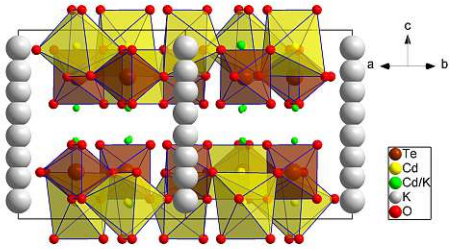

(b) View along the [110] direction with $[TeO_6]^{6-}$ and $[CdO_6]$ octahedra network.

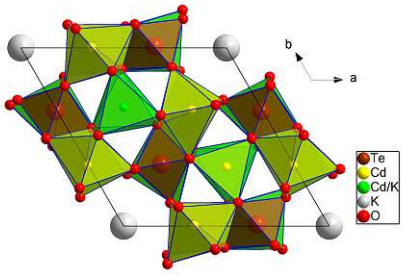

(c) View along the [001] direction with polyhedra of the K and K-Cd channels.

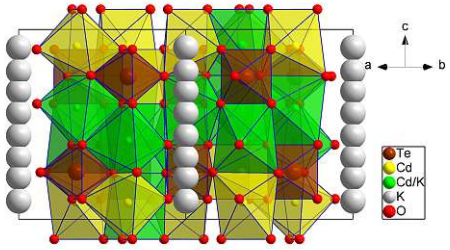

(d) View along the [110] direction with polyhedra of the K and K-Cd channels.

Figure 26: Crystal structure of $K_{14/3}Cd_{47/3}Te_6O_{36}$ (above) and $K_{14/3}Cd_{47/3}Te_6O_{36}$ with K and K-Cd coordination polyhedra (below).

Additionally, figure 27 shows the different Cd and (K,Cd) mixed position coordination geometries. Most of the coordination geometries are very close to those found in $K_{5.5}(Co_{0.9}Ni_{0.1})_{14.5}Te_6O_{36}$ for Co and K, but show slight distortion due to the change in cell parameters. These manifest in slight torsion of the trigonal prisms or distortion of angles and distances in the octahedra.

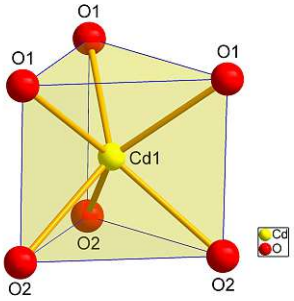

(a) Cd1 [CdO_6] trigonal prismatic coordination geometry.

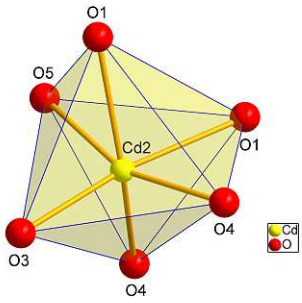

(b) Cd2 [CdO_6] distorted octahedral coordination geometry.

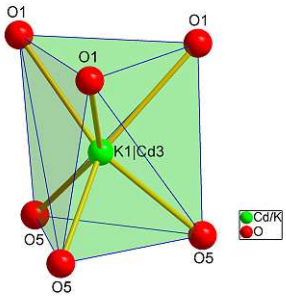

(c) (Cd3,K1) [$(Cd_3,K_1)O_6$] twisted trigonal prismatic coordination geometry.

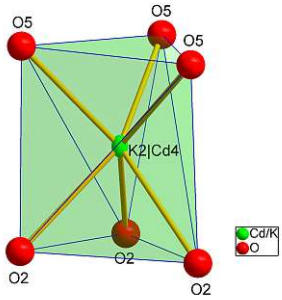

(d) (Cd4,K2) [$(Cd_4,K_2)O_6$] twisted trigonal prismatic coordination geometry.

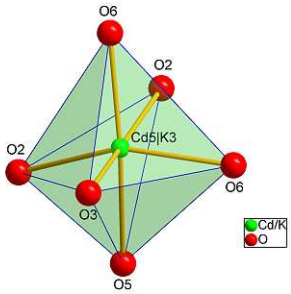

(e) (Cd5,K3) [$(Cd_5,K_3)O_6$] distorted octahedral coordination geometry.

Figure 27: Coordination geometry of the Cd and mixed occupany K-Cd sites in $K_{14/3}Cd_{47/3}Te_6O_{36}$.

3.5 Other oxidotellurate and oxidotellurate chloride crystal structures

3.5.1 $Ca_2Te_2O_7$ related to $Cd_2Te_2O_7$

A novel mixed-valence Te(IV) Te(VI) compound, $Ca_2Te_2O_7$, was found. This compound is closely related to $Cd_2Te_2O_7$, which was reported by Weil 2004 [11]. The triclinic crystal structure with the space group $P\overline{1}$ was refined with $Z = 2$, measured at 300K and the cell parameters are $a = 7.4607(3)$ Å, $a = 10.1847(3)$ Å, $c = 8.4428(3)$ Å, $\alpha = 94.446(3)°$, $\beta = 77.307(3)°$ and $\gamma = 100.500(3)°$. A value of $R_1[I >= 2\sigma(I)] = 0.0310$ and $wR_2[all] = 0.0900$ was achieved with 26413 independent reflections and 202 parameters. The measured crystal was a four component twin.

Figure 28 shows the crystal structure of both $Ca_2Te_2O_7$ and $Cd_2Te_2O_7$. Also clearly visible are chains of $[TeO_6]^{6-}$ octahedra, oriented in the **a** direction. Te(IV) coordinates trigonal pyramidally in both structures. Half of the $[TeO_4]^{4-}$ pyramids in $Ca_2Te_2O_7$ and $Cd_2Te_2O_7$ are attached to the $[TeO_6]^{6-}$ chains, while the other half are isolated.

However, the Ca and Cd coordination geometry shows discrepancies in the structures. While all Ca atoms show sevenfold, somewhat irregular coordination in $Ca_2Te_2O_7$, half the Cd atoms in $Cd_2Te_2O_7$ clearly display a distorted $[CdO_6]^{10-}$ octahedral geometry. The other Cd atoms also show a somewhat irregular capped triangular prismatic $[CdO_7]^{12-}$ coordination geometry.

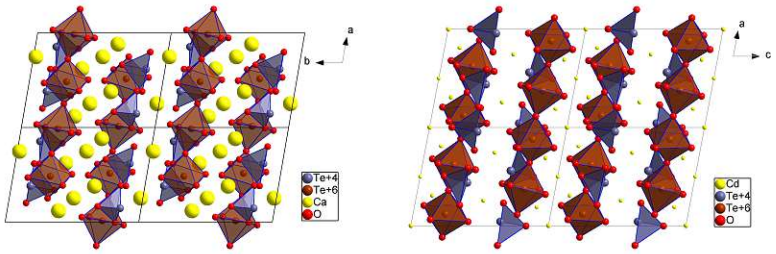

(a) View of $Ca_2Te_2O_7$ along the [100] direction.

(b) View of $Cd_2Te_2O_7$ along the [001] direction.

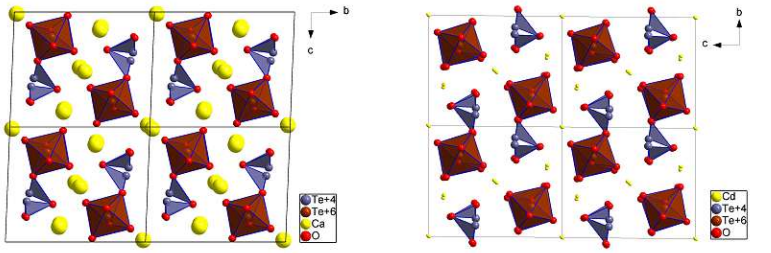

(c) View of $Ca_2Te_2O_7$ along the [100] direction in the $[TeO_6]^{6-}$ chain orientation.

(d) View of $Cd_2Te_2O_7$ along the [100] direction in the $[TeO_6]^{6-}$ chain orientation.

Figure 28: Structure comparison of $Ca_2Te_2O_7$ with the already known $Cd_2Te_2O_7$.

3.5.2 Crystal structure of $Ca_3Cu_3Te_2O_{12}$

The crystal structure of $Ca_3Cu_3Te_2O_{12}$ with the space group $P4_2/nnm$ is shown in figure 29. The structure model was refined with $Z = 2$, measured at 300K and the cell parameters are $a = b = 7.3290(4)$ Å and $c = 8.6353(5)$ Å. A value of $R_1[I >= 2\sigma(I)] = 0.0183$ and $wR_2[all] = 0.0412$ was achieved with 344 independent reflections and 32 parameters. A powder XRD measurement and Rietveld fit of sample SnB16 gave the cell parameters $\widehat{a} = \widehat{b} = 7.34115(9)$ Å and $\widehat{c} = 8.65666(2)$ Å which are in good agreement with the single crystal XRD results.
This structure features two kinds of Cu environments namely a quadratic planar $[CuO_4]^{6-}$ and a slightly distorted $[CuO_4]^{6-}$ arrangement, which is formed by displacing two oxygen atoms out of the plane of the quadratic planar coordination. The expected $[TeO_6]^{6-}$ units are observed here as well and a triperiodic network together with the $[CuO_4]^{6-}$ fragments. In between this network of interconnected $[CuO_4]^{6-}$ and $[TeO_6]^{6-}$ units, two distinct Ca atoms are positioned, which show rectangular $[CaO_8]^{14-}$ and irregular $[CaO_8]^{14-}$ coordination. During the investigation another unknown phase was found, which we tentatively identified as Ca_2CuTeO_6 using the base structure of $SrCaNi(TeO_6)$ [58] as a model using Rietveld refinement. Further analysis on this phase is under work.

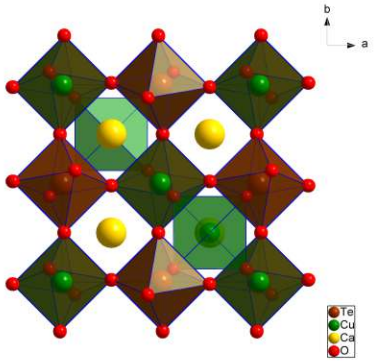

(a) View along the [001] direction.

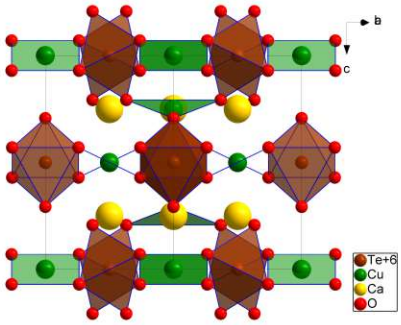

(b) View along the [-110] direction.

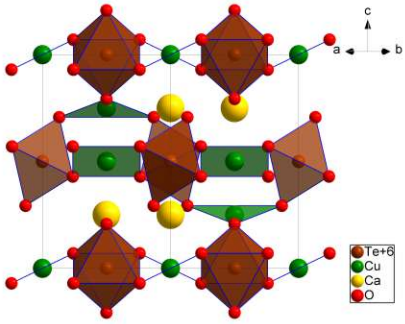

(c) View along the [110] direction.

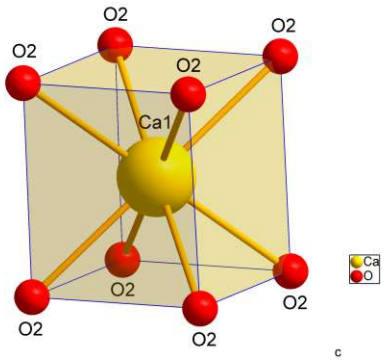

(d) Rectangular Ca1 [CaO_8] coordination geometry.

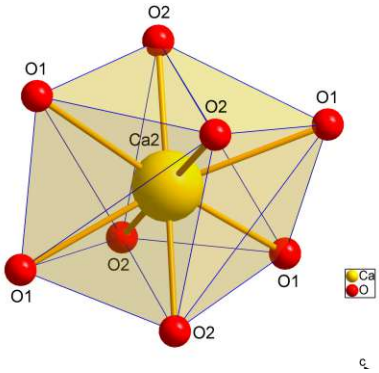

(e) Irregular Ca2 [CaO_8] coordination geometry.

Figure 29: Crystal structure of $Ca_3Cu_3Te_2O_{12}$ (above). Rectangular Ca1 [CaO_8] and irregular Ca2 [CaO_8] coordination (below).

3.5.3 Crystal structure of $CaCu_2TeO_6$

A further novel calcium copper oxidotellurate(VI) was isolated, namely $CaCu_2TeO_6$ with the monoclinic space group $C2/c$. This structure model was refined with $Z = 2$, measured at 300K and the cell parameters are 9.6555(6) Å, b = 7.0316(3) Å, c = 6.8627(4) Å and β = 92.911(5). A value of $R_1[I >= 2\sigma(I)] = 0.0168$ and $wR_2[all] = 0.0403$ was achieved with 896 independent reflections and 51 parameters. However, the synthesis of this compound could not be reproduced. The phase fraction in the sample it was isolated from, was so low, no reflections could be attributed to $CaCu_2TeO_6$ in the sample's powder diffractograms - the intensity of the reflections was likely too low to be visible. Initially, sample SnB14 yielded $Ca_3Cu_3Te_2O_{12}$, where that component was present at a phase fraction of 86%. Attempts at reproducing $CaCu_2TeO_6$ and searching for a suspected Ca_2CuTeO_6 phase were unsuccessful and resulted in $Ca_3Cu_3Te_2O_{12}$ instead. Unfortunately, since the relative amount of $CaCu_2TeO_6$ in the heated sample HT3 it was obtained from was so low and the phase could not be reproduced, we do not have any powder XRD data on this phase.
A chemically related structure is the $I4/m$ Sr_2CuTeO_6 [59], which does not share a group-subgroup relationship with $CaCu_2TeO_6$.
Figure 30 shows the crystal structure of $CaCu_2TeO_6$. It bears resemblance to the structure of $Ca_3Cu_3Te_2O_{12}$, which is discussed above, however both structures crystallize in distinct space groups of $C2/c$ and $P4_2/nnm$, respectively. The monoclinic angle of 92.928(10)° is also close to the corresponding orthorhombic 90° angle in $Ca_3Cu_3Te_2O_{12}$. $CaCu_2TeO_6$ and $Ca_3Cu_3Te_2O_{12}$ do not show a group-subgroup relationship. This is because $Ca_3Cu_3Te_2O_{12}$ has a higher point symmetry of $4/mmm$, while $CaCu_2TeO_6$ has a higher translational symmetry. The fact that the reduced cell volume of $CaCu_2TeO_6$ is actually smaller than that of $Ca_3Cu_3Te_2O_{12}$ evidences this. So, a group-subgroup relationship between the spacegroups is prohibited.
Still, there certainly is a crystal chemical relationship present owing to the similarilty of composition and coordination geometry in both phases. The biggest difference between the two structures in this regard is increased distortion of some $[CuO_4]^{6-}$ positions. The slightly distorted quadratic planar positions in $Ca_3Cu_3Te_2O_{12}$ are further increased in $CaCu_2TeO_6$ and become an intermediate between tetrahedral and quadratic planar coordination. The atomic positions and anisotropic atomic displacement parameters of $CaCu_2TeO_6$ are compiled in the appendix in table 23 and 22.

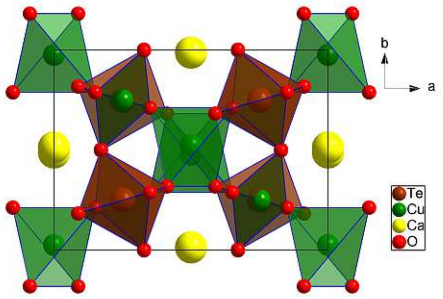

(a) View along the [001] direction.

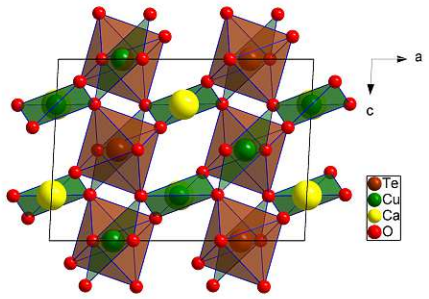

(b) View along the [010] direction.

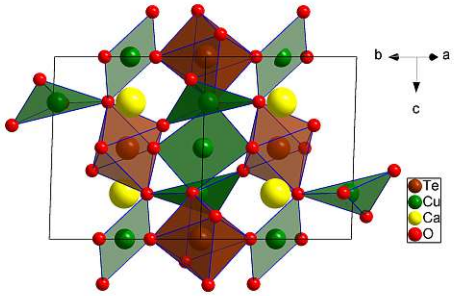

(c) View along the [110] direction.

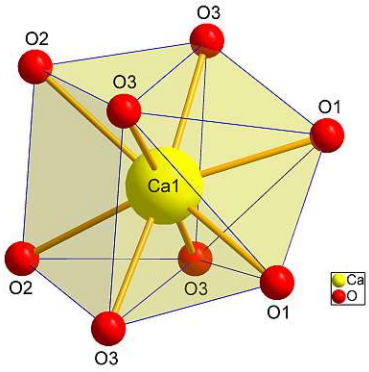

(d) Irregular eightfold Ca1 [CaO_8] coordination geometry.

Figure 30: Above and below left: Crystal structure of $CaCu_2TeO_6$. Quadratic planar [CuO_4] and a distorted quadratic planar [CuO_4] coordination geometry occur for Cu1 and Cu2, respectively. Lower right: Irregular eightfold Ca1 [CaO_8] coordination in $CaCu_2TeO_6$.

3.5.4 Crystal structure of $Ca_5Te_4O_{12}Cl_2$

A novel calcium oxidotellurate chloride $Ca_5Te_4O_{12}Cl_2$ was obtained reproducibly via a series of solid state synthesis experiments with CsCl and $CaCl_2$ flux. $Ca_2TeO_3Cl_2$ and $Ca_5Te_4O_{12}Cl_2$ (which will be described in the next section) were synthesized serendipitously while investigating the suitability of Ca to substitute for M in $A_2M_2TeO_6$ honeycomb tellurates. The reaction conditions are summarized in section 2.3.6 and table 6 on page 24. Following the initial synthesis of $Ca_5Te_4O_{12}Cl_2$ in sample S11, it was reproduced with a set of similar experiments (utilizing TeO_2 instead of $Te(OH)_6$), ultimately aiming at achieving single phase material. During this set of experiments, $Ca_2TeO_3Cl_2$ was obtained unexpectedly, as yet another fortunate coincidence in sample SnB61. The maximal achieved, reproducible purity was around 50% for both $Ca_2TeO_3Cl_2$ and $Ca_5Te_4O_{12}Cl_2$.
MoK_α radiation was used to obtain this $Pnma$ structure model with $Z = 4$ and the cell parameters $a = 17.1142(4)$ Å, $b = 18.2830(6)$ Å, $c = 11.1879(3)$ Å. A value of $R_1[I >= 2\sigma(I)] = 0.0322$ and $wR_2[all] = 0.0808$ was achieved with 11576 independent reflections and 214 parameters. The cell parameters obtained by Rietveld fit of sample SnB64 in comparison show a small deviation: $\widehat{a} = 17.1240(2)$ Å, $\widehat{b} = 18.2654(1)$ Å, $c = 11.246(1)$ Å. While a and $\widehat{a}$ as well as b and $\widehat{b}$ match closely, c and $\widehat{c}$ differ by about 6‰.
The crystal structure of $Ca_5Te_4O_{12}Cl_2$ is shown in figure 31. It contains isolated trigonal $[TeO_4]$ pyramids. The Ca coordination in this compound is 6-8 fold (depending on the Ca-O bondlength cutoff used, here: 2.7 Å) and irregular, except for the two Ca atoms (Ca1 and Ca4) which bind to Cl atoms. These show a distorted trigonal prismatic sixfold $[CaO_4Cl_2]^{8-}$ coordination geometry, as is shown in figure 31c and 31d. Bond lengths and distances for the trigonal prismatic Ca coordination geometries can be found in the appendix section 8.1.7, in table 26 on page 101.
All atoms lie on the general position, except for the Cl atoms, which are located on a .m. site. Between the Cl atoms open channels extend parallel to the chlorine atom layer in the [001] direction. This leads to a relatively low theoretical density of around 3.695 g/cm^3.
The Wyckoff positions and anisotropic atomic displacement parameters of $Ca_5Te_3O_{12}Cl_2$ are summarized in the apendix under section 8.1.7 page 100, tables 27 and 28.

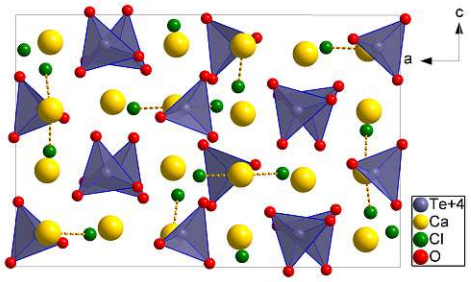

(a) View along the [010] direction.

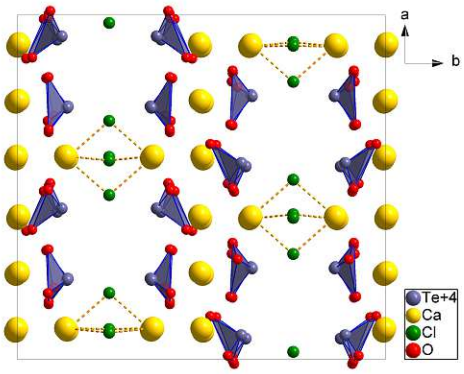

(b) View along the [001] direction.

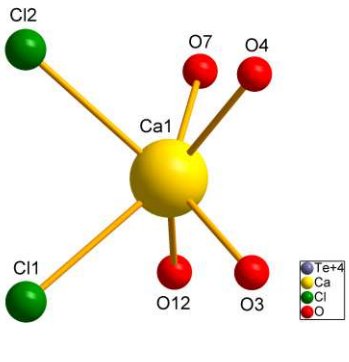

(c) Distorted trigonal Ca1 $[CaO_4Cl_2]^{8-}$ prism.

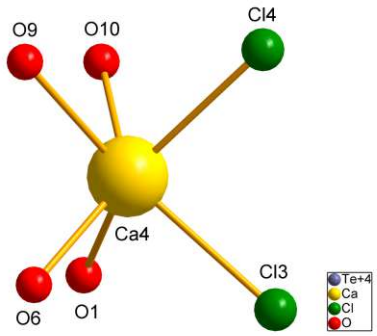

(d) Distorted trigonal Ca4 $[CaO_4Cl_2]^{8-}$ prism.

Figure 31: Top: Crystal structure of $Ca_5Te_4O_{12}Cl_2$. Trigonal $[TeO_4]$ pyramids shown in blue, Ca-Cl bonds drawn as dotted lines. Bottom: Trigonal prismatic $[CaO_4Cl_2]^{8-}$ coordination.

Notably, when $Ca_5Te_4O_{12}Cl_2$ was first obtained, $Te(OH)_6$ was used as a reagent, but the product contained only Te(IV). The Te(VI) species likely underwent thermal decomposition, similar to the decomposition of TeO_3 into TeO_2 upon heating.
Figure 32 shows the PXRD measurement with Rietveld fit of the $Ca_5Te_4O_{12}Cl_2$ sample. According to a semi quantitative XRD analysis, the sample consisted of near equal amounts of $Ca_5Te_4O_{12}Cl_2$ and Ca_3TeO_6. As is discussed in detail in section 2.3.6 on page 24 a phase pure synthesis pathway could not be found, however the synthesis was found to be reproducible.

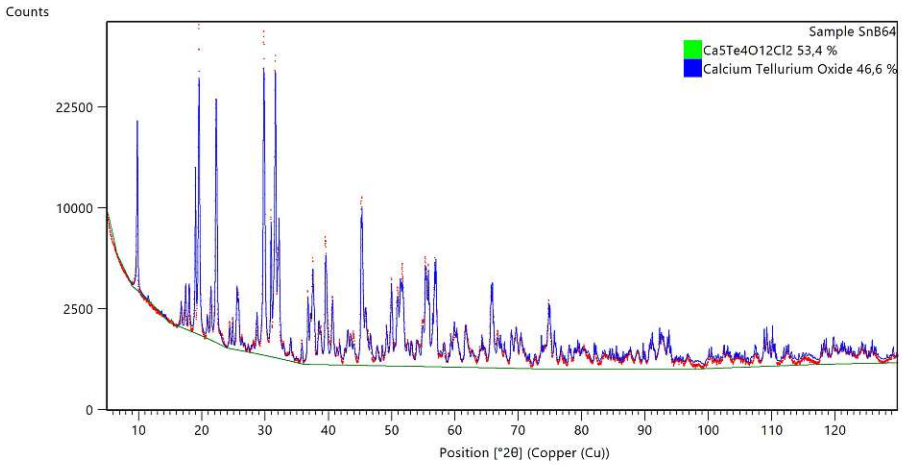

Figure 32: Rietveld fit of sample SnB64 containing $Ca_5Te_4O_{12}Cl_2$.

3.5.5 Crystal structure of $Ca_2TeO_3Cl_2$

The compound $Ca_2TeO_3Cl_2$ formed in similar conditions as $Ca_5Te_4O_{12}Cl_2$, which was discussed in the previous section. The notable difference in the synthesis conditions was the amount of added $CaCl_2$. $CaCl_2$ was always added in excess as a flux and reactant (relative to the Cl content of the product). The relative amount compared to the other reactants determined the prevalent products. The structure crystallizes in the triclinic space group $P\bar{1}$ and the cell parameters $Z = 2$, $a = 6.6855(13)$ Å, $b = 6.7181(12)$ Å, $c = 8.0847(15)$ Å, $\alpha = 66.645(5)°$, $\beta = 67.917(5)°$ and $\gamma = 82.124(6)°$. A value of $R_1[I >= 2\sigma(I)] = 0.0372$ and $wR_2[all] = 0.0688$ was achieved with 4129 independent observed reflections and 73 parameters. The cell parameters obtained by Rietveld fit of sample SnB61 confirm the cell determination done with single crystal structure determination: $\widehat{a} = 6.6905(2)$ Å, $\widehat{b} = 6.7401(2)$ Å, $c = 8.1104(3)$ Å, $\alpha = 66.7601(5)°$, $\beta = 67.8821(5)°$ and $\gamma = 82.0556(6)°$. Small deviations are present, but thermal contraction explains the variations between a, b, c and $\widehat{a}$, $\widehat{b}$, $\widehat{c}$. Since the single crystal measurement was performed at 100 K and the powder measurements at 300 K the cell parameters observed by powder XRD are larger.
The structure of $Ca_2TeO_3Cl_2$ is depicted in figure 33. The distinct trigonal pyramidal configuration of $[(TeO_3)]^{2-}$ units is clearly visible. Additionally, the Ca atoms show a sevenfold coordination, with three of the ligands being Cl atoms. This geometry is reminiscent of the *meridional* 33c and *facial* 33c arrangement in octahedral coordination, notwithstanding the different coordination number of seven. The most prominent feature of this structure are the layers formed by $[(CaO_4Cl_3)]^{9-}$ units, which are separated by $[(TeO_3)]^{2-}$ units. The $[(CaO_4Cl_3)]^{9-}$ layers are connected via a Ca-Cl-Ca bond two-dimensional network. Empty channels in the [010] direction are present between the $[(TeO_3)]^{2-}$ units. This is most evident in figure 33a.

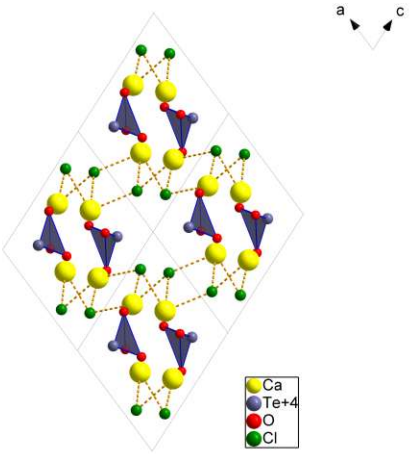

(a) View along the [100] direction.

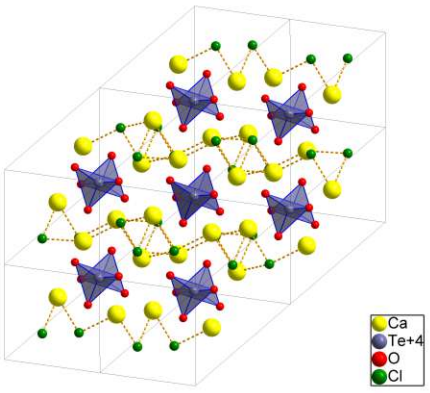

(b) View along the [11-1] direction.

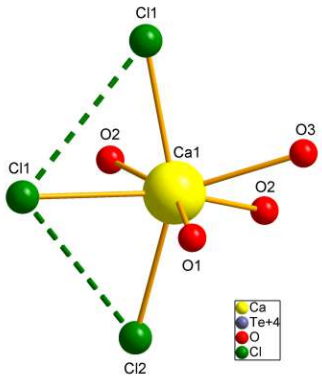

(c) Sevenfold $[CaO_4Cl_3]^{9-}$ irregular coordination geometry of Ca1.

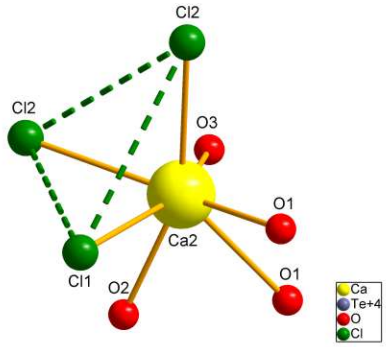

(d) Sevenfold $[CaO_4Cl_3]^{9-}$ irregular coordination geometry of Ca2.

Figure 33: Above: Crystal structure of $Ca_2Te_{O3}Cl_2$. Ca-Cl bonds are depicted as dashed lines. Below: Irregular, sevenfold $[CaO_4Cl_3]^{9-}$ coordination geometry of Ca1 and Ca2 in $Ca_2Te_{O3}Cl_2$.

3.5.6 $(Co_{0.93}Ni_{0.07})_3TeO_6$ phase

A novel, orthorhombic $Pca2_1$ $(Co_{0.93}Ni_{0.07})_3TeO_6$ orthotellurate was synthesized. The structure solution produced a model with $Z = 16$ and the cell parameters $a = 10.3819(3)$ Å, $b = 8.6126(2)$ Å and $c = 19.8265(5)$ Å. A value of $R_1[I >= 2\sigma(I)] = 0.0253$ and $wR_2[all] = 0.0493$ was achieved with 12718 independent observed reflections and 363 parameters. A powder measurement and Rietveld fit of sample SnB50 revealed cell parameters of $\widehat{a} = 10.3800(1)$ Å, $\widehat{b} = 8.61375(9)$ Å and $\widehat{c} = 19.8305(2)$ Å, which are in excellent agreement with the data from single crystal XRD.
It is suspected that the Ni and Co atoms share the same positions in the crystal structure, which would make this a solid solution. $(Co_{0.93}Ni_{0.07})_3TeO_6$ was obtained unexpectedly from solid state synthesis reactions aimed at producing Co_3TeO_6 [60]. The crystal structure of $(Co_{0.93}Ni_{0.07})_3TeO_6$ shows a clear relation to Co_3TeO_6, but their respective space groups $Pca2_1$ and $C2/c$ have no group-subgroup relationship. From the standpoint of crystal chemistry however, the crystal structures are intimately related. As Becker et al. reported for Co_3TeO_6 [60], $(Co_{0.93}Ni_{0.07})_3TeO_6$ consists of a network of $[TeO_6]^{6-}$ and distorted $[CoO_6]^{10-}$ octahedra as well as $[CoO_4]^{6-}$ tetrahedra. However, the difference in the structures lies in the orientation of the network and polyhedra, which leads to very similar cell parameters. The number of Co atoms in tetrahedral and octahedral coordination shifts aswell, since they connect different orientations of $[TeO_6]^{6-}$ octahedra respectively.

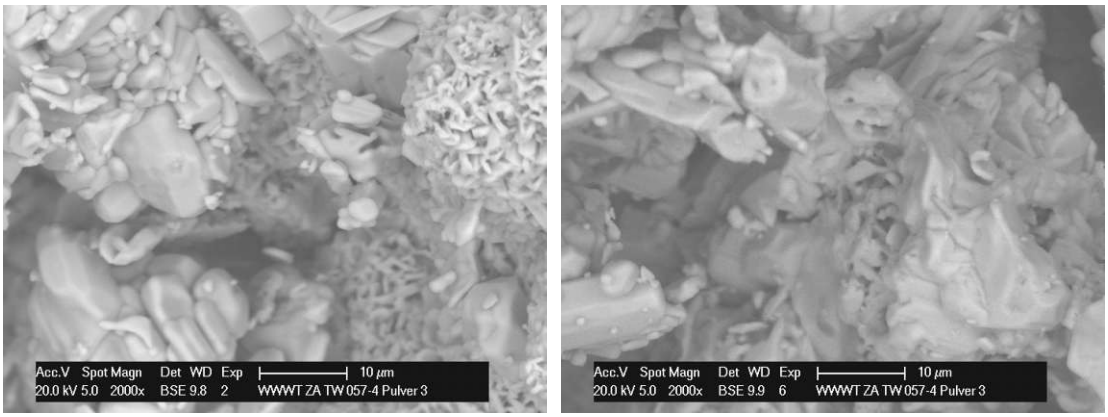

Figure 34: SEM pictures of $(Co_{0.93}Ni_{0.07})_3TeO_6$ grains from sample SnB41. EDX measurements were taken in these areas, to determine the Ni content of the sample grains and whether it is inhomogeneously distributed.

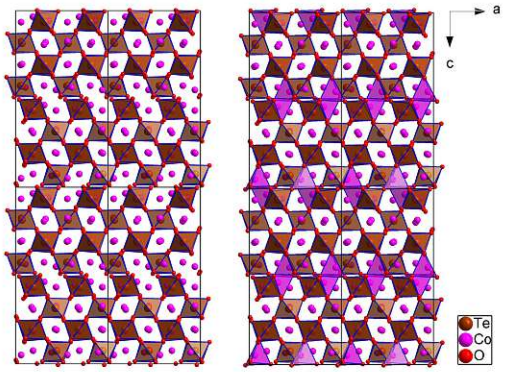

(a) View of $(Co_{0.93}Ni_{0.07})_3TeO_6$ along the [010] direction. Left without and right with $[CoO_4]^{6-}$ tetrahedra.

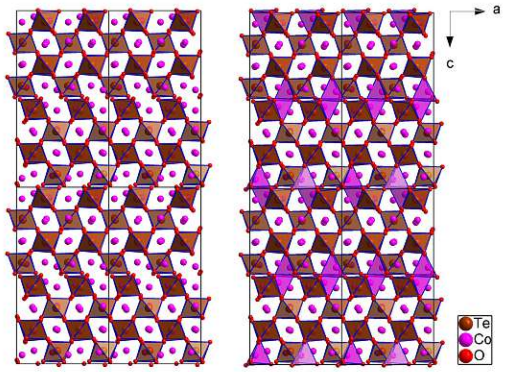

(b) View of Co_3TeO_6 along the [010] direction. Left without and right with $[CoO_4]^{6-}$ tetrahedra

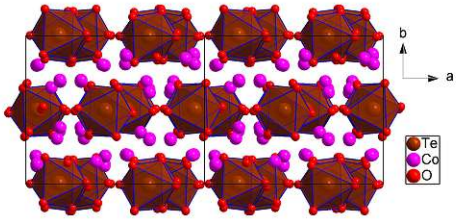

(c) View of $(Co_{0.93}Ni_{0.07})_3TeO_6$ along the [001] direction.

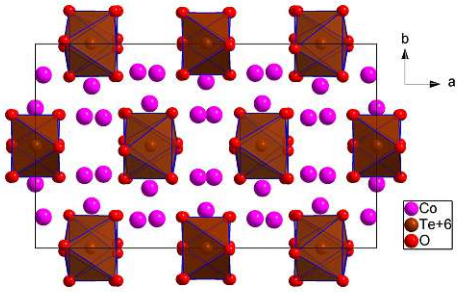

(d) View of Co_3TeO_6 along the [001] direction.

Figure 35: Structure comparison of $(Co_{0.93}Ni_{0.07})_3TeO_6$ with the known Co_3TeO_6. The major difference can be seen in 35a and 35b, with the differing $[TeO_6]^{6-}$ orientation and the monoclinic cell angle of Co_3TeO_6. Moreoever, $[CoO_4]^{6-}$ tetrahedra are less numerous in $(Co_{0.93}Ni_{0.07})_3TeO_6$.

3.5.7 Crystal structure of $H_8Rb_4Cu_2Te_2O_{14}$

A new rubidium oxidotellurate(VI) $H_8Rb_4Cu_2Te_2O_{14}$ was found, with a structure isotypic with the potassium analogue $H_4K_4Cu_2Te_2O_{14}$ reported by Effenberg and Tillmanns in 1992 [52].
MoK_α radiation at room temperature was used to determine the monoclinic Cc structure with $Z = 2$ and the cell parameters $a = 9.4781(6)$ Å, $b = 6.4883(4)$ Å, $c = 12.4659(8)$ Å and $\beta = 91.110(2)°$. A value of $R_1[I >= 2\sigma(I)] = 0.027$ and $wR_2[all] = 0.0498$ was achieved with 4065 independent reflections and 113 parameters. A powder measurement and Rietveld fit of sample HT4 gave the cell parameters $\widehat{a} = 9.4777(8)$ Å, $\widehat{b} = 6.4773(6)$ Å, $\widehat{c} = 12.4478(7)$ Å and $\widehat{\beta} = 91.0401(12)°$, which match the data from single crystal XRD very well.
The cell parameters of $H_8Rb_4Cu_2Te_2O_{14}$ and $H_4K_4Cu_2Te_2O_{14}$ are in good agreement, the largest increase owing to the larger Rb ionradius is observed for the c-axis. Overall, the cell volume increases from 718.26(26) Å to 766.47(8) Å. The monoclinic angle β changes only slightly from 90.44(2)° to 91.110(2)°. The relative atomic positions do not shift significantly and the occupied Wyckoff positions in both structures are all general.
Effenberg and Tillmanns described hydrogen positions and hydrogen bonds, but could not obtain a reliable position from structure refinement itself. With the data presented here, we achieved this for $H_8Rb_4Cu_2Te_2O_{14}$, which confirms their chemical and crystallographic considerations of the H positions.
The crystal structure of $H_8Rb_4Cu_2Te_2O_{14}$ can be seen in figure 36. $[TeO_4(OH)_2]^{4-}$ octahedra and the slightly distorted, quadratically planar coordinated $[CuO_4]^{6-}$ units form chains that constitute a two-dimensional criss-cross pattern. The structure appears as a layered structure from some directions, see figure 36b or 36c, but the chains themselves are monoperiodic, as is clearly visible in figure 36a. Rb coordination is similarly irregular to the ninefold coordination geometry of K in $H_4K_4Cu_2Te_2O_{14}$ [52].

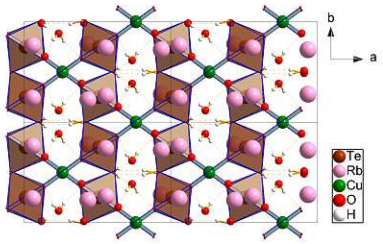

(a) View of $H_8Rb_4Cu_2Te_2O_{14}$ along the [001] direction.

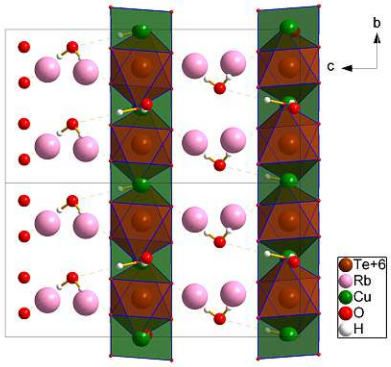

(b) View of $H_8Rb_4Cu_2Te_2O_{14}$ along the [100] direction.

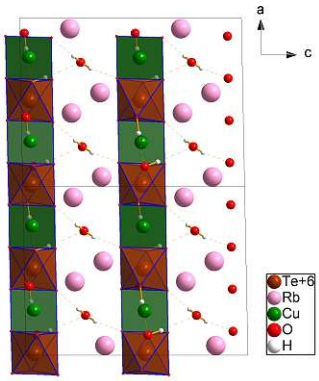

(c) View of $H_8Rb_4Cu_2Te_2O_{14}$ along the [010] direction.

Figure 36: Crystal structure of $H_8Rb_4Cu_2Te_2O_{14}$ in different viewing directions. The [100] and [010] directions (below) show that this structure does not consist of layers, as the [001] directional view (above) might suggest.

3.5.8 Crystal structures of $H_6K_3FeTe_2O_{12}$ and $H_4K_3FeTe_2O_{11}$

A novel $H_6K_3FeTe_2O_{12}$ iron potassium oxidotellurate(VI) with the monoclinic space group $C2/m$ was prepared via hydrothermal synthesis. The cell parameters are given as $Z = 8, a = 14.1306(7)$ Å, $b = 14.9042(8)$ Å, $c = 5.9782(3)$ Å and $\beta = 115.0300(10)°$. A value of $R_1[I >= 2\sigma(I)] = 0.0212$ and $wR_2[all] = 0.0385$ was achieved with 2348 independent observed reflections and 97 parameters. A powder measurement and Rietveld fit of sample HT8 gave the cell parameters $\widehat{a} = 14.1297(15)$ Å, $\widehat{b} = 14.9160(4)$ Å, $\widehat{c} = 5.9776(5)$ Å and $\widehat{\beta} = 114.9884(18)°$, that show excellent agreement with the structure cell determination by single crystal XRD.
The phase is a hydrate and possesses multiple positions for H atoms, which make it difficult to determine the placement of hydrogen in the structure. In fact, we suspect that some hydrogen positions may be only partially occupied, complicating the matter further. Since the single crystal XRD measurements of tellurates tend towards larger absorptions artifacts caused by the high electronic density of Te, assignment of H positions due to electronic density alone is difficult. A more feasible approach is the consideration of possible hydrogen bonds and bond valence calculations. Still, even with these tools we determined only the positions of some H atoms present in $H_6K_3FeTe_2O_{12}$.
The crystal structure of $H_6K_3FeTe_2O_{12}$ is depicted in figure 37 and features layers formed by $[TeO_4(OH)_2]^{4-}$ and $[(Te,Fe)O_6]^{6-,9-}$ octahedra in the stacking direction [010]. However these are jagged layers and are also penetrated by K atoms, forming holes in the layers and are therefore not honeycomb layers. Crystal refinement of the phase showed pseudo orthorhombic symmetry, which is broken mostly by the occupational Fe/Te disorder occuring in the $[(Te,Fe)O_6]$ octahedra. This Fe/Te disorder is likely caused by stacking faults, which were observed as diffuse rods in the diffraction images. There exist two Fe/Te positions, showing a 20/80 and 80/20 split respectively. The K positions show irregular ninefold coordination, where it is not entirely certain, where and which ligands are OH or H_2O ligands. The oxygen atom O7/O7' displaying positional disorder in a 70/30 ratio was confirmed to be in fact either OH or H_2O, where the H positions were not refined. This confirmation was accomplished by the fact, that heating a $H_6K_3FeTe_2O_{12}$ single crystal yielded a dehydrated $H_4K_3FeTe_2O_{11}$ phase, missing this oxygen position.
Investigations via non-ambient powder XRD revealed at least one phase transition and some decomposition reactions for $H_6K_3FeTe_2O_{12}$. This was expected, considering the phase is a hydrate. The first of these transitions was indeed monitored with single crystal XRD following the initial discovery and was confirmed to be a dehydrated $H_4K_3FeTe_2O_{11}$ phase, with largely unchanged cell parameters (compare table 12) and also preserving the same symmetry.$H_4K_3FeTe_2O_{11}$ has the same space group of Cc. For refinement, a value of $R_1[I >= 2\sigma(I)] = 0.0212$ and $wR_2[all] = 0.0385$ was achieved with 2348 independent observed reflections and 97 parameters.

Table 12: Comparison of cell parameters of $H_6K_3FeTe_2O_{12}$ and the dehydrated $H_4K_3FeTe_2O_{11}$ phase.

Phase	a [Å]	b [Å]	c [Å]	a [°]	V [Å]^3
$\mathbf{H_6K_3FeTe_2O_{12}}$	14.1306(7)	14.9042(8)	5.9782(3)	115.0300(10)	1140.80(10)
$\mathbf{H_4K_3FeTe_2O_{11}}$	14.0888(6)	14.9470(6)	5.9706(2)	115.027(3)	1139.27(8)

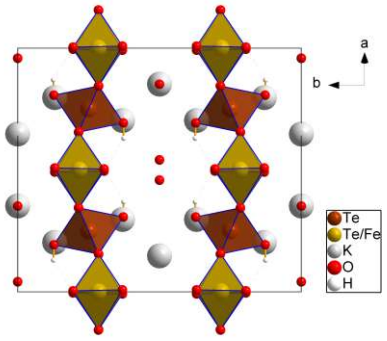

(a) View of $H_6K_3FeTe_2O_{12}$ along the [001] direction.

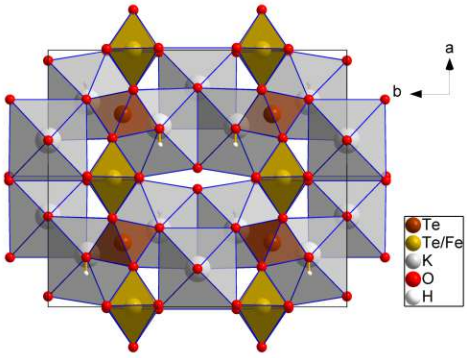

(b) View of $H_6K_3FeTe_2O_{12}$ along the [100] direction with K coordination polyhedra shown.

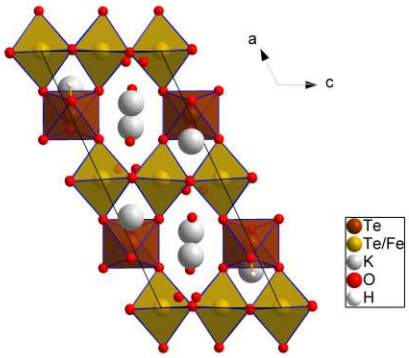

(c) View of $H_6K_3FeTe_2O_{12}$ along the [100] direction.

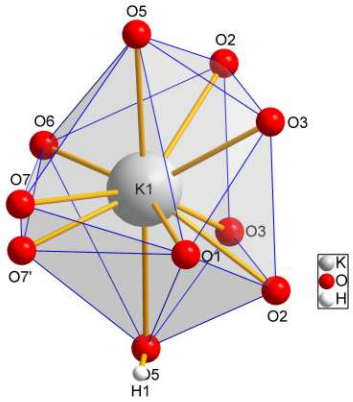

(d) Irregular, ninefold $[KO_9H_x]^{-(17-x)}$ coordination geometry. O7 and O7' represent one O atom showing positional disorder.

Figure 37: Crystal structure of $H_6K_3FeTe_2O_{12}$ in different viewing directions. As can be seen in 37a, $H_6K_3FeTe_2O_{12}$ forms layers made of $[TeO_6H_y]^{-(6-y)}$ and $[FeO_6]^{9-}$ octahedra in the stacking direction [010]. Holes or channels in the layers, as is shown in 37c are occupied by K atoms which are positioned slightly above and below the jagged octahedra layers. The position of the H atoms is not fully entirely clear yet.

The triperiodic depiction of the non-ambient powder XRD scans is shown in figure 38. It is evident that a number of phase changes can be observed. At around 150-175°C a new reflection forms at around 13° 2Θ. This is the dehydration to $H_4K_3FeTe_2O_{11}$, which was confirmed by a single crystal measurement at around 160(2)°C, which yielded a structure solution for $H_4K_3FeTe_2O_{11}$. Further phase transitions include an amorphisation at around 450(2)°C, where all sharp Bragg reflections have vanished. Between 160 and 450°C another unknown phase exists. It is possible that this is another phase related to $H_6K_3FeTe_2O_{12}$, possibly formed by more dehydration. After around 525°C a new phase begins to form, which is Fe_3TeO_6. At this point, essentially a new solid phase reaction is taking place, which means the dataset from that point onward is no longer of interest pertaining to the investigation of $H_6K_3FeTe_2O_{12}$.

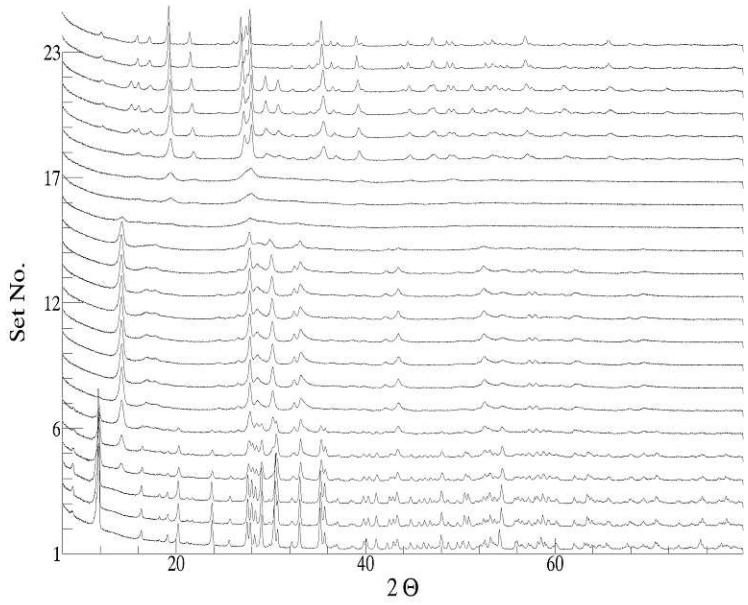

(a) Three-dimensional plot depicting array of non-ambient powder XRD measurements of sample HT8 containing $H_6K_3FeTe_2O_{12}$.

Scan Nr.	T [°C]
1	75
2	125
3	150
4	175
5	200
6	225
7	250
8	275
9	300
10	325
11	350
12	375
13	400
14	425
15	450
16	475
17	500
18	525
19	550
20	575
21	600
22	625
23	650

Figure 38: Three-dimensional plot depicting array of non-ambient powder XRD measurements of sample HT8 containing $H_6K_3FeTe_2O_{12}$ (left), heated up to 650°C as given by the temperature table (right).

As is depicted in figure 39, the crystal structure of $H_4K_3FeTe_2O_{11}$ is nearly isomorphous to that of $H_6K_3FeTe_2O_{12}$, discounting the absence of the disordered O7/O7' oxygen atom, which is therefore likely either an H_2O or OH group. This also results in a change of coordination for the K1 position, as seen in subfigure 39b.

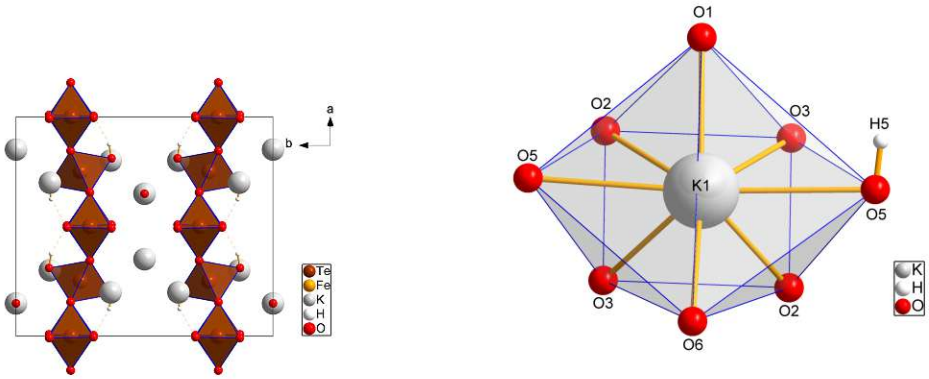

(a) View of $H_4K_3FeTe_2O_{11}$ along the [001] direction.

(b) Irregular, eightfold $[KO_8H_x]^{-(17-x)}$ coordination geometry.

Figure 39: Crystal structure of $H_4K_3FeTe_2O_{11}$ in the [001] direction. The structure is essentially unchanged from $H_6K_3FeTe_2O_{12}$ barring the absence of water in the channels in the [001] direction, compare with figure 37a.

3.5.9 Tentative novel $K_2Fe_6Te_2O_{16}$ and $Rb_2Fe_6Te_2O_{16}$ phases

A novel potassium and a novel rubidium iron oxidotellurate were synthesized and modelled using powder XRD data and Rietveld refinement. Because the crystal structure is of the hollandite type, Rietveld refinement was performed based on the data of the isotypic crystal structures $K_2Fe_2Ti_6O_{16}$ [61] and $Rb_2Fe_2Ti_6O_{16}$ [62]. The difference in the sum formulae between the base models and the obtained phases arises because of the higher positive charge of Te, which occurs as Te(VI) vs. the Ti(IV). The presence of Te(VI) and not Te(IV) was confirmed by the typical octahedral coordination of Ti and Fe in the crystal structures of $K_2Fe_2Ti_6O_{16}$ and $Rb_2Fe_2Ti_6O_{16}$. Because of the electronic neutrality, a ratio of Te to Fe as is present in $K_2Fe_6Te_2O_{16}$ follows. While Fe could theoretically occur as Fe(II), this seems unlikely, since the octahedral coordination is not typical for Fe(II) atoms.
However, further investigations are necessary to confirm the presented model. The synthesis of single crystals of these novel phases would be ideal. If no single crystals are avaibable that an EDX measurement or an electron microprobe measurement could affirm or disprove the suggested elementary composition. Figures 40 and 41 show the diffractograms of samples HT62 and HT64 containing $K_2Fe_2Ti_6O_{16}$ and $Rb_2Fe_2Ti_6O_{16}$ respectively. The comparison in figure 42 shows the close similarities between the diffractograms. Unexpectedly however, the reflections in $Rb_2Fe_2Ti_6O_{16}$ are shifted to **higher** angles, which indicates a smaller cell. Since Rb is larger, the usual expectation would be a shift to **lower** diffraction angles, which is not observed here however. We can not explain this result as of yet, more investigations are needed.

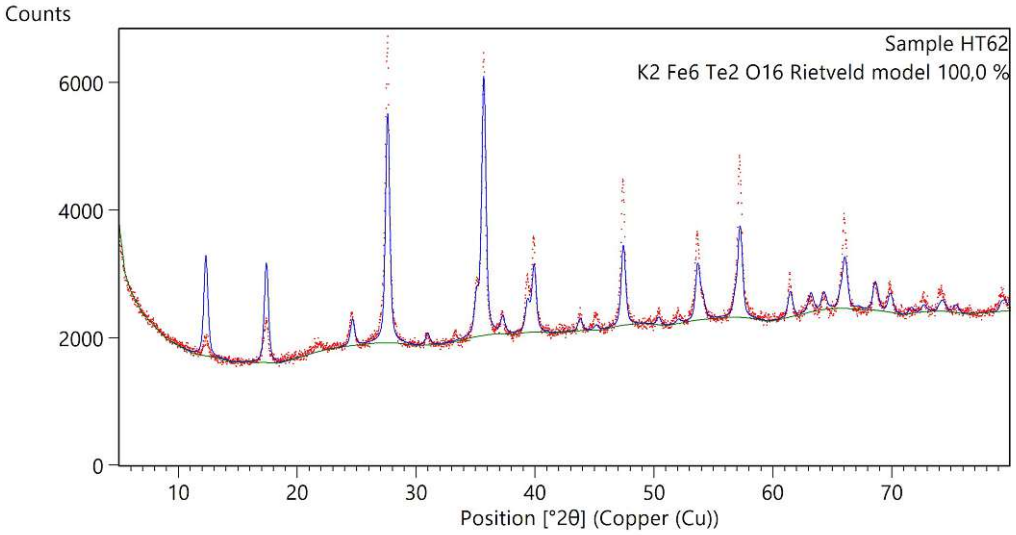

Figure 40: Rietveld fit of sample HT62 containing $K_2Fe_6Te_2O_{16}$, based on the crystal structure of $Rb_2Fe_2Ti_6O_{16}$ [62].

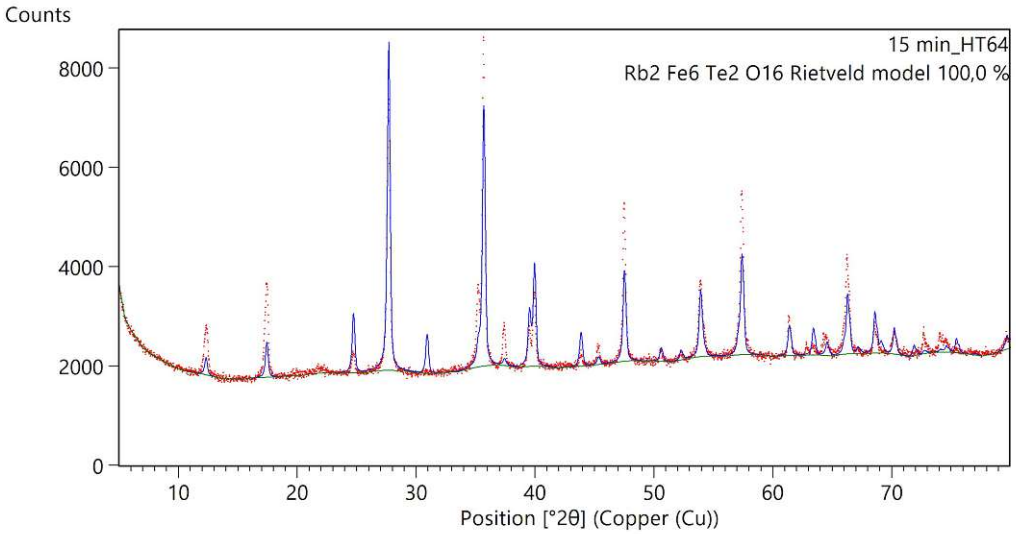

Figure 41: Rietveld fit of sample HT64 containing $Rb_2Fe_6Te_2O_{16}$, based on the crystal structure of $Rb_2Fe_2Ti_6O_{16}$ [62].

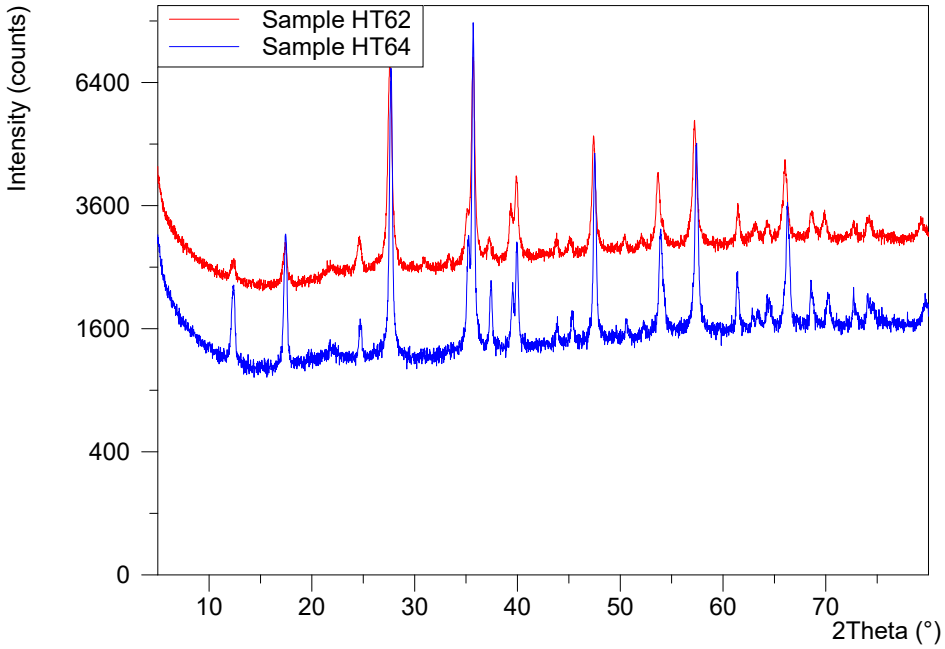

Figure 42: Comparison of $K_2Fe_6Te_2O_{16}$ and $Rb_2Fe_6Te_2O_{16}$ Rietveld fits.

3.6 Investigation into Rb and Cs honeycomb tellurates

As described in the methods section, numerous experiments were conducted to synthesize Rb and Cs honeycomb tellurates (see section 2.3.2 from page 21 onward). While some of these samples yielded novel phases, such as $H_8Rb_4Cu_2Te_2O_{14}$ and the tentative $Rb_2Fe_6Te_2O_{16}$ phase, neither Rb nor Cs honeycomb tellurates could be evidenced. Some samples showed signs of the presence of honeycomb tellurates, such as SnB5 and SnB12. The powder diffractograms of a selection of these samples is shown in figure 43.
Clearly, reflections are present in positions where the 002 and 004 honeycomb tellurate layer reflections in stacking direction are expected. In this case, they would indicate a layer distance of approximately 14.6 Å, determined by Rietveld refinement based on the $K_2Ni_2TeO_6$ basic crystal structure. Notably however, all other reflections, such as the 100 or 110 reflection are absent in the diffractograms. This likely means that the produced phases are some sort of layered structure, probably containing Te and Rb, but likely not honeycomb tellurates. Moreover, this assumption is reinforced by the fact that later experiments could not reproduce diffractograms containing the reflections suggesting a honeycomb tellurates. Instead, Rb_2TeO_4 was often identified as the major phase in the products, as shown for samples SnB66 and SnB74 in figure 44. This assumption is reasonable, since the in-situ monitoring of similar systems containing K instead of Rb showed the formation of K_2TeO_4 as a major intermediate phase (compare section 3.3.5 starting at page 43). Had formation of Rb honeycomb tellurates occurred, present Rb_2TeO_4 would have likely reacted completely to form them. Moreover, honeycomb tellurates are not expected to undergo decomposition upon cooling, rendering the reformation of Rb_2TeO_4 also unlikely.
We furthermore suspect the formed Rb_2TeO_4 to form various hydrates upon exposure to air. However, no such hydrates are published in the ICSD so far and we were not able to obtain single crystals of such phases from the samples.
It is entirely possible that Rb honeycomb tellurates are not stable due to the larger ion radius of Rb. This would result in increased Rb ion repulsion inside a hypothetical $Rb_2M_2TeO_6$ honeycomb tellurate. Similarly, no Cs honeycomb tellurates or analogous phases were obtained in the performed experiments. This is in agreement with the explanation of increased repulsion due to the trend of growing ionic radii by atomic number.

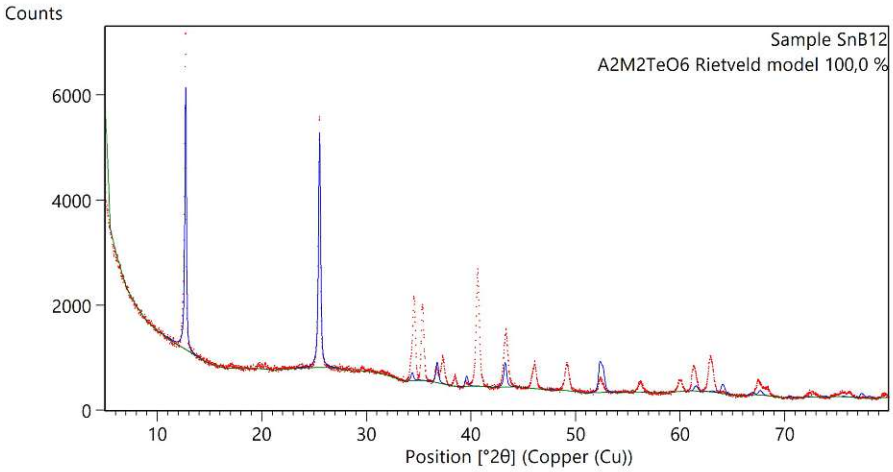

(a) Rietveld fit of sample SnB12. To model the honeycomb tellurate like reflections, modelling with the crystal structure of $K_2Ni_2TeO_6$ was performed.

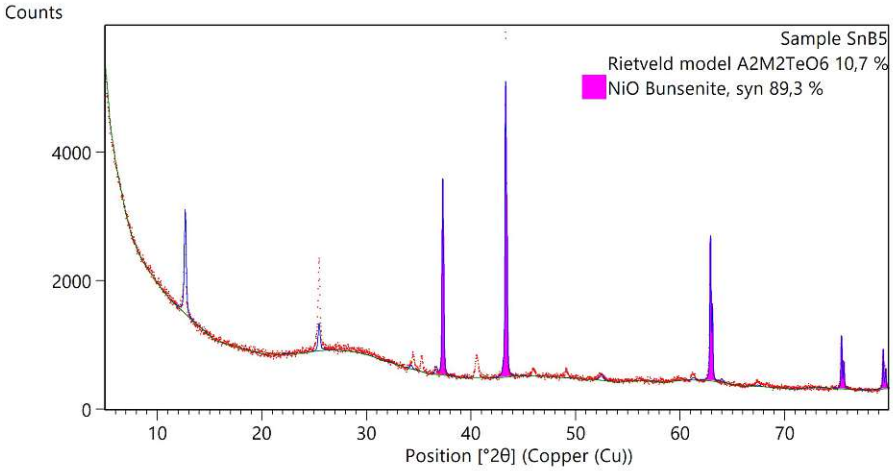

(b) Rietveld fit of sample SnB5. To model the honeycomb tellurate like reflections, modelling with the crystal structure of $K_2Ni_2TeO_6$ was performed.

Figure 43: Rietveld fit of samples SnB5 and SnB12 with, modelling honeycomb-esque reflections.

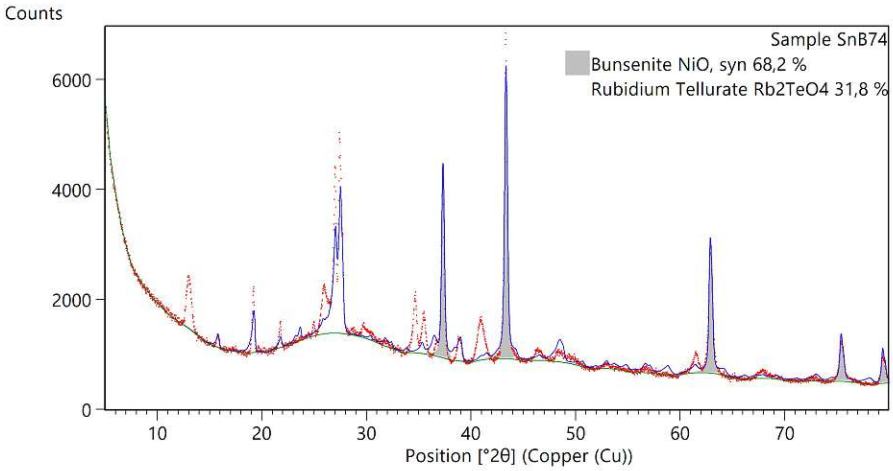

(a) Rietveld fit of sample SnB74.

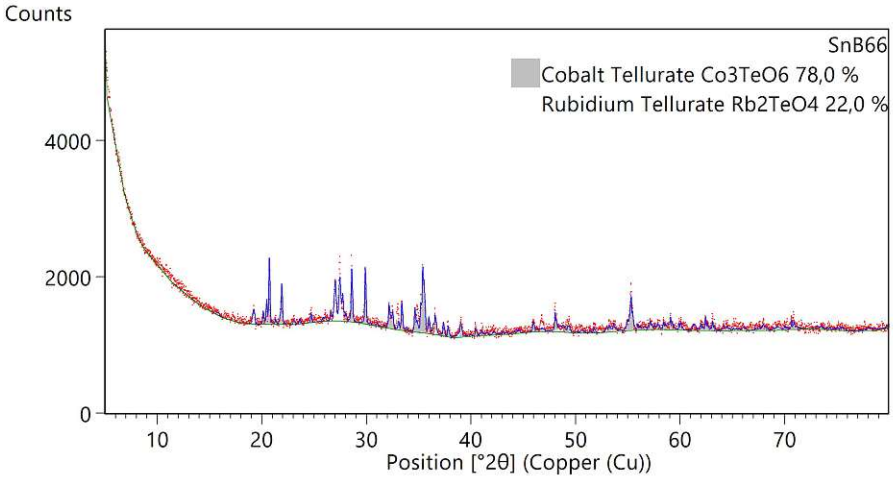

(b) Rietveld fit of sample SnB66.

Figure 44: Rietveld fits for samples SnB66 and SnB74 showing the presence of Rb_2TeO_4.

4 Conclusion

We demonstrated the existence of several novel honeycomb tellurates, including $K_{2(x-y)}Ni_xTe_yO_{2(x+y)}$ and $Na_{2(x-y)}Ni_xTe_yO_{2(x+y)}$ type honeycomb tellurates. $Na_2Ni_2TeO_6$ and $K_2Ni_2TeO_6$ are already known in recent literature and have been investigated for their electrochemical properties. Together with the (non ideal) structure solution we obtained for $K_4Ni_5Te_3O_{16}$, this knowledge paves the way to further research into the suitabililty of honeycomb tellurates as battery materials in K ion batteries.

$K_4Ni_5Te_3O_{16}$ shows a descent from the hexagonal symmetry of the intimately related $K_2Ni_2TeO_6$ to a orthorhombic space group of $Amm2$. The c-axis is doubled and the structure shows at least two distinct kinds of K layers labelled $\boldsymbol{B_1}$ and $\boldsymbol{B_2}$. $\boldsymbol{B_1}$ is well defined in the structure solution, while $\boldsymbol{B_2}$ appears to consist of an overlay of different K-layers. This may be caused by the OD character of the crystal structure. Furthermore, the $\mathbf{B_1}$ K layer of $K_4Ni_5Te_3O_{16}$ shows the minimization of K-K repulsion forces by the arrangement of K atoms in the available positions. This arrangement of K atoms was not observed in $Na_2Ni_2TeO_6$ and $K_2Ni_2TeO_6$ by the respective authors. Most novel honeycomb tellurate phases, which were obtained, also featured diffuse scattering caused by stacking faults. In the case of $K_2Ni_2TeO_6$ disorder was also shown by HRTEM imaging. In literature this was only known to occur for $Na_2Ni_2TeO_6$, but according to our results this seems to be more likely to a general feature of $A_2M_2TeO_6$ honeycomb tellurates.

The novel arrangement of $[TeO_6]^{-6}$ and $[NiO_6]^{-10}$ octahedra showing $[Te_2O_{12}]^{12-}$ subunits in the honeycomb layers could allow for geometric magnetic frustration. Since $Na_2Ni_2TeO_6$ is known to be antiferromagnetic at low temperatures, this might be worth investigating in the future.

Additionally, reaction monitoring via non ambient powder XRD revealed some long lived reaction intermediates in the solid state synthesis of $K_{2(x-y)}Ni_xTe_yO_{2(x+y)}$ type honeycomb tellurates from TeO_2, NiO and KNO_3. First K_2TeO_4 is formed at around 450°C, which already includes an oxidation of Te(IV) to Te(VI). This shows that neither the oxidation of Te(IV) nor the availabilty of K ions seem to be rate limiting, but rather the reactivity of NiO. We believe that this approximate mechanism is applicable also in the more general $A_2M_2TeO_6$ case. Thus, for successful synthesis of honeycomb tellurates, the usage of more reactive M ion sources (for example nitrates) would be one of the highest priorities.

Several other novel honeycomb tellurates were found with SAED, TEM and ED measurements, of which the structure is yet unknown. A $Na_{2(x-y)}Ni_xTe_yO_{2(x+y)}$ type honeycomb tellurate was found by single crystal XRD measurement, however no structure solution of sufficient quality was possible. This was due to the fact that the $Na_{2(x-y)}Ni_xTe_yO_{2(x+y)}$ crystal exhibited extensive diffuse scattering and was additionally of poor quality. Therefore, only the cell and a family structure were confirmed. The family structure is the smallest cell with a honeycomb $(Ni,Te)O_2$ layer and Na atoms positioned in between. Furthermore, a $K_{2(x-y)}Ni_xTe_yO_{2(x+y)}$ type honeycomb tellurate was discovered by SAED measurements.

Repeated experiments also indicated that $Rb_2M_2TeO_6$ and $Cs_2M_2TeO_6$ are very difficult to synthesize, if they are at all stable. The synthesis is impeded greatly by the deliquescent properties of what we believe to be Rb_2TeO_4 in accordance with our results from non ambient powder XRD reaction monitoring in the $K_{2(x-y)}Ni_xTe_yO_{2(x+y)}$ synthesis. Also, the minimization of K-K repulsion in the $\mathbf{B_1}$ K layer of $K_4Ni_5Te_3O_{16}$ further reinforces the instability of $Rb_2M_2TeO_6$ and $Cs_2M_2TeO_6$ honeycomb tellurates because the A-A repulsion grows while the A-layer interaction becomes more unfavourable (increasing widening of layers by larger ion radius leads to changes in coordination towards stretched prisms). In the more general case, our experience with the synthesis

and attempted synthesis of various $A_2M_2TeO_6$ honeycomb tellurates show that the formation of suitable single crystals for single crystal XRD is hard to control. However, the structural features, such as the stacking faults and preferred orientation of crystallites in powdered samples necessitate additional methods aside powder XRD. Therefore, another way in future research into honeycomb tellurates may be the increased usage of TEM imaging as well as SAED and electron diffraction measurements, since they can provide more structural information while not needing large single crystals.

Several novel oxidotellurate phases with a wide variety of crystal structures were also synthesized. Novel phases always carry the potential to find application in further fields down the road. Furthermore, for some of the novel phases (including $Ca_5Te_4O_{12}Cl_2$, $Ca_2TeO_3Cl_2$ and $(Co_{0.93}Ni_{0.07})_3TeO_6$), a range of experiments were done to confirm reproducibility and find a preliminary satisfying synthesis route. Therefore, most of our results should be well reproducable and the novel phases can be investigated for the material properties further in the future.

Summarizing, there is further research necessary, especially concerning the diffuse scattering and quantification of it. $K_4Ni_5Te_3O_{16}$ and the several novel honeycomb tellurate phases we found need to be studied in more detail, as well as other, already investigated systems of $A_2M_2TeO_6$ honeycomb tellurates. Powder XRD should ideally be supplemented with further methods besides single crystal XRD such as TEM and SAED in these investigations.

5 References

References

[1] A. K. Bera and S. M. Yusuf, "Temperature-dependent Na-ion conduction and its pathways in the crystal structure of the layered battery material $Na_2Ni_2TeO_6$," *The Journal of Physical Chemistry C*, vol. 124, no. 8, pp. 4421–4429, 2020. DOI: 10.1021/acs.jpcc.9b11191. eprint: https://doi.org/10.1021/acs.jpcc.9b11191. [Online]. Available: https://doi.org/10.1021/acs.jpcc.9b11191.

[2] G. Fonthal, L. Tirado-Mejíia, J. Maríin-Hurtado, H. Ariza-Calderíon, and J. Mendoza-Alvarez, "Temperature dependence of the band gap energy of crystalline cdte," *Journal of Physics and Chemistry of Solids*, vol. 61, no. 4, pp. 579–583, 2000, ISSN: 0022-3697. DOI: https://doi.org/10.1016/S0022-3697(99)00254-1. [Online]. Available: https://www.sciencedirect.com/science/article/pii/S0022369799002541.

[3] T. D. Lee and A. U. Ebong, "A review of thin film solar cell technologies and challenges," *Renewable and Sustainable Energy Reviews*, vol. 70, pp. 1286–1297, 2017, ISSN: 1364-0321. DOI: https://doi.org/10.1016/j.rser.2016.12.028. [Online]. Available: https://www.sciencedirect.com/science/article/pii/S136403211631070X.

[4] "Cadmium telluride accelerator consortium." (2022), [Online]. Available: https://www.energy.gov/eere/solar/cadmium-telluride-accelerator-consortium (visited on 09/14/2022).

[5] A. G. Christy, S. J. Mills, and A. R. Kampf, "A review of the structural architecture of tellurium oxycompounds," *Mineralogical Magazine*, vol. 80, no. 3, pp. 415–545, 2016. DOI: 10.1180/minmag.2016.080.093.

[6] A. F. Holleman and E. W. und Nils Wiberg, *Anorganische Chemie*. Berlin/Boston: Walter de Gruyter GmbH, 2017, vol. Band 1.

[7] Y. Moëlo, E. Makovicky, N. N. Mozgova, *et al.*, "Sulfosalt systematics: a review. Report of the sulfosalt sub-committee of the IMA Commission on Ore Mineralogy," *European Journal of Mineralogy*, vol. 20, no. 1, pp. 7–46, Feb. 2008, ISSN: 0935-1221. DOI: 10.1127/0935-1221/2008/0020-1778. eprint: https://pubs.geoscienceworld.org/eurjmin/article-pdf/20/1/7/3126472/007_ejm20_1_007_046_moelo.pdf. [Online]. Available: https://doi.org/10.1127/0935-1221/2008/0020-1778.

[8] G. Tunell, "The atomic arrangement of sylvanite," *American Mineralogist*, vol. 26, no. 8, pp. 457–477, Aug. 1941, ISSN: 0003-004X. eprint: https://pubs.geoscienceworld.org/msa/ammin/article-pdf/26/8/457/4237291/am-1941-457.pdf.

[9] S. R. Lewis, "The crystal structure of some metallic sulfides," *Journal Mineralogical Society of America*, vol. 10, pp. 281–304, 1925.

[10] M. Rabadanov, I. Verin, Y. Ivanov, and V. Simonov, "Refinement of the atomic structure of CdTe single crystals," *Crystallography Reports*, vol. 46, pp. 636–641, Jul. 2001. DOI: 10.1134/1.1387130.

[11] M. Weil, "New phases in the systems Ca−Te−O and cd-te-o: The calcium tellurite(iv) ca4te5o14, and the cadmium compounds cd2te3o9 and cd2te2o7 with mixed-valent oxotellurium(iv/vi) anions," *Solid State Sciences*, vol. 6, no. 1, pp. 29–37, 2004, ISSN: 1293-2558. DOI: https://doi.org/10.1016/j.solidstatesciences.2003.11.003. [Online]. Available: https://www.sciencedirect.com/science/article/pii/S1293255803002474.

[12] N. Barrier, S. Malo, O. Hernandez, M. Hervieu, and B. Raveau, "The mixed valent tellurate $SrTe_3O_8$: Electronic lone pair effect of te4+," *Journal of Solid State Chemistry*, vol. 179, no. 11, pp. 3484–3488, 2006, ISSN: 0022-4596. DOI: https://doi.org/10.1016/j.jssc.2006.07.012. [Online]. Available: https://www.sciencedirect.com/science/article/pii/S0022459606003872.

[13] *Zeitschrift für Kristallographie*, vol. 124, no. 3, pp. 228–237, 1967. DOI: doi:10.1524/zkri.1967.124.3.228. [Online]. Available: https://doi.org/10.1524/zkri.1967.124.3.228.

[14] M. Dušek and J. Loub, "X-ray powder diffraction data and structure refinement of teo3," *Powder Diffraction*, vol. 3, no. 3, pp. 175–176, 1988. DOI: 10.1017/S0885715600032942.

[15] M. Cameron, S. Sueno, C. T. Prewitt, and J. J. Papike, "High-Temperature Crystal Chemistry of Acmite, Diopside, Hedenbergite Jadeite, Spodumene and Ureyite," *American Mineralogist*, vol. 58, no. 7-8, pp. 594–618, Aug. 1973, ISSN: 0003-004X. eprint: https://pubs.geoscienceworld.org/msa/ammin/article-pdf/58/7-8/594/4257177/am-1973-594.pdf.

[16] J. W. Gruner, "The crystal structure of kaolinite," *Zeitschrift für Kristallographie - Crystalline Materials*, vol. 83, no. 1-6, pp. 75–88, 1932. DOI: doi:10.1524/zkri.1932.83.1.75. [Online]. Available: https://doi.org/10.1524/zkri.1932.83.1.75.

[17] O. Lindqvist, "Refinement of the structure of alpha-TeO_2.," *Acta Chemica Scandinavica*, vol. 22, pp. 977–982, 1968. DOI: doi:10.3891/acta.chem.scand.22-0977.

[18] J. Champarnaud-Mesjard, S. Blanchandin, P. Thomas, A. Mirgorodsky, T. Merle-Méjean, and B. Frit, "Crystal structure, raman spectrum and lattice dynamics of a new metastable form of tellurium dioxide: Γ-TeO_2," *Journal of Physics and Chemistry of Solids*, vol. 61, no. 9, pp. 1499–1507, 2000, ISSN: 0022-3697. DOI: https://doi.org/10.1016/S0022-3697(00)00012-3. [Online]. Available: https://www.sciencedirect.com/science/article/pii/S0022369700000123.

[19] U. Müller, *Symmetry Relationships between Crystal Structures: Applications of Crystallographic Group Theory in Crystal Chemistry*. Great Clarendon Street, Oxford, OX2 6DP: Oxford University Press, 2013.

[20] T. Hahn, H. Arnold, M. I. Aroyo, and et al., *International Tables for Crystallography: Space-group symmetry*. Wiley, 2006, vol. A, ISBN: ISBN: 978-0-7923-6590-7. DOI: https://doi.org/10.1107/97809553602060000100.

[21] G. Aminoff, "Über die struktur des magnesiumhydroxydes," *Zeitschrift für Kristallographie - Crystalline Materials*, vol. 56, pp. 505–509, 1921. DOI: 10.1524/zkri.1921.56.1.506.

[22] V. Kopský, D. B. Litvin, and et al., *International Tables for Crystallography: Subperiodic groups*. Wiley, 2006, vol. E, ISBN: ISBN: 978-1-4020-0715-6. DOI: https://doi.org/10.1107/97809553602060000105.

[23] R. Woeber. "Honey comb pollen." (2017), [Online]. Available: https://pixabay.com/photos/honeycomb-pollen-hexagon-2441542/ (visited on 09/19/2022).

[24] T. Masese, K. Yoshii, Y. Yamaguchi, *et al.*, "Rechargeable potassium-ion batteries with honeycomb-layered tellurates as high voltage cathodes and fast potassium-ion conductors," *Nature Communications*, vol. 9, Sep. 2018. DOI: 10.1038/s41467-018-06343-6.

[25] R. D. Shannon, "Revised effective ionic radii and systematic studies of interatomic distances in halides and chalcogenides," *Acta Crystallographica Section A*, vol. 32, no. 5, pp. 751–767, 1976. DOI: https://doi.org/10.1107/S0567739476001551. eprint: https://onlinelibrary.wiley.com/doi/pdf/10.1107/S0567739476001551. [Online]. Available: https://onlinelibrary.wiley.com/doi/abs/10.1107/S0567739476001551.

[26] K. Dornberger-Schiff and H. Grell-Niemann, "On the theory of order–disorder (OD) structures," *Acta Crystallographica*, vol. 14, no. 2, pp. 167–177, Feb. 1961. DOI: 10.1107/S0365110X61000607. [Online]. Available: https://doi.org/10.1107/S0365110X61000607.

[27] M. M. J. Treacy, J. M. Newsam, and M. W. Deem, "A general recursion method for calculating diffracted intensities from crystals containing planar faults," *Proceedings: Mathematical and Physical Sciences*, vol. 433, no. 1889, pp. 499–520, 1991, ISSN: 09628444. [Online]. Available: http://www.jstor.org/stable/51916 (visited on 09/13/2022).

[28] N. Episcopo, P.-H. Chang, T. W. Heitmann, *et al.*, "Magnetic structure, excitations and short-range order in honeycomb na2ni2teo6," *Journal of Physics: Condensed Matter*, vol. 33, no. 37, p. 375 803, Jul. 2021. DOI: 10.1088/1361-648X/ac0ea6. [Online]. Available: https://dx.doi.org/10.1088/1361-648X/ac0ea6.

[29] K. Mizushima, P. Jones, P. Wiseman, and J. Goodenough, "LixCoO$_2$ (0¡x¡-1): A new cathode material for batteries of high energy density," *Materials Research Bulletin*, vol. 15, no. 6, pp. 783–789, 1980, ISSN: 0025-5408. DOI: https://doi.org/10.1016/0025-5408(80)90012-4. [Online]. Available: https://www.sciencedirect.com/science/article/pii/0025540880900124.

[30] J. Akimoto, Y. Gotoh, and Y. Oosawa, "Synthesis and structure refinement of LiCoO$_2$ single crystals," *Journal of Solid State Chemistry*, vol. 141, no. 1, pp. 298–302, 1998, ISSN: 0022-4596. DOI: https://doi.org/10.1006/jssc.1998.7966. [Online]. Available: https://www.sciencedirect.com/science/article/pii/S002245969897966X.

[31] C. Greaves and S. Katib, "The structural chemistry of Li$_3$Zn$_2$MO$_6$ (m=sb, bi) and related phases," *Materials Research Bulletin*, vol. 25, no. 9, pp. 1175–1182, 1990, ISSN: 0025-5408. DOI: https://doi.org/10.1016/0025-5408(90)90148-U. [Online]. Available: https://www.sciencedirect.com/science/article/pii/002554089090148U.

[32] K. Kang, Y. S. Meng, J. Bréger, C. P. Grey, and G. Ceder, "Electrodes with high power and high capacity for rechargeable lithium batteries," *Science*, vol. 311, no. 5763, pp. 977–980, 2006. DOI: 10.1126/science.1122152. eprint: https://www.science.org/doi/pdf/10.1126/science.1122152. [Online]. Available: https://www.science.org/doi/abs/10.1126/science.1122152.

[33] A. A. Pospelov, V. B. Nalbandyan, E. I. Serikova, *et al.*, "Crystal structure and properties of a new mixed-valence compound LiMn$_2$TeO$_6$ and the survey of the LiMM'XO$_6$ family (x = sb or te)," rus ; eng, vol. 13, no. 11, pp. 1931–1937, 2011, ISSN: 1293-2558.

[34] V. Kumar, N. Bhardwaj, N. Tomar, V. Thakral, and S. Uma, "Novel lithium-containing honeycomb structures," *Inorganic Chemistry*, vol. 51, no. 20, pp. 10 471–10 473, 2012. DOI: 10.1021/ic301125n. eprint: https://doi.org/10.1021/ic301125n. [Online]. Available: https://doi.org/10.1021/ic301125n.

[35] V. Nalbandyan, M. Avdeev, and M. Evstigneeva, "Crystal structure of Li$_4$ZnTeO$_6$ and revision of Li$_3$Cu$_2$SbO$_6$," *Journal of Solid State Chemistry*, vol. 199, pp. 62–65, 2013, ISSN: 0022-4596. DOI: https://doi.org/10.1016/j.jssc.2012.11.027. [Online]. Available: https://www.sciencedirect.com/science/article/pii/S0022459612007116.

[36] M. A. Evstigneeva, V. B. Nalbandyan, A. A. Petrenko, B. S. Medvedev, and A. A. Kataev, "A new family of fast sodium ion conductors: Na2m2teo6 (m = ni, co, zn, mg)," *Chemistry of Materials*, vol. 23, no. 5, pp. 1174–1181, 2011. DOI: 10.1021/cm102629g. eprint: https://doi.org/10.1021/cm102629g. [Online]. Available: https://doi.org/10.1021/cm102629g.

[37] V. Nalbandyan, A. Petrenko, and M. Evstigneeva, "Heterovalent substitutions in Na$_2$M$_2$TeO$_6$ family: Crystal structure, fast sodium ion conduction and phase transition of na2lifeteo6," *Solid State Ionics*, vol. 233, pp. 7–11, 2013, ISSN: 0167-2738. DOI: https://doi.org/10.1016/j.ssi.2012.12.002. [Online]. Available: https://www.sciencedirect.com/science/article/pii/S0167273812006510.

[38] J. Orive, R. Sivasamy, R. F. de Luis, E. Mosquera, and M. I. Arriortua, "K$_2$MnII$_2$(H$_2$O)$_2$C$_2$O$_4$(HPO$_3$)$_2$: A new 2d manganese(ii) oxalatophosphite with double-layered honeycomb sheets stabilized by potassium ions," *CrystEngComm*, vol. 20, pp. 301–311, 2018.

[39] L. D. Sanjeewa, M. A. McGuire, C. D. McMillen, D. R. Willett, G. Chumanov, and J. W. Kolis, "Honeycomb-like s = 5/2 spin-lattices in manganese(ii) vanadates.," *Inorganic chemistry*, vol. 55 18, pp. 9240–9, 2016.

[40] D. Su, A. McDonagh, S.-Z. Qiao, and G. Wang, "High-capacity aqueous potassium-ion batteries for large-scale energy storage," *Advanced Materials*, vol. 29, no. 1, p. 1 604 007, 2017. DOI: https://doi.org/10.1002/adma.201604007. [Online]. Available: https://onlinelibrary.wiley.com/doi/abs/10.1002/adma.201604007.

[41] X. Wu, D. Leonard, and X. Ji, "Emerging non-aqueous potassium-ion batteries: Challenges and opportunities," *Chemistry of Materials*, vol. 29, May 2017. DOI: 10.1021/acs.chemmater.7b01764.

[42] J. C. Pramudita, D. Sehrawat, D. Goonetilleke, and N. Sharma, "An initial review of the status of electrode materials for potassium-ion batteries," *Advanced Energy Materials*, vol. 7, no. 24, p. 1 602 911, 2017. DOI: https://doi.org/10.1002/aenm.201602911. eprint: https://onlinelibrary.wiley.com/doi/pdf/10.1002/aenm.201602911. [Online]. Available: https://onlinelibrary.wiley.com/doi/abs/10.1002/aenm.201602911.

[43] A. Rabenau, "The role of hydrothermal synthesis in preparative chemistry," *Angewandte Chemie International Edition in English*, vol. 24, no. 12, pp. 1026–1040, 1985. DOI: https://doi.org/10.1002/anie.198510261. eprint: https://onlinelibrary.wiley.com/doi/pdf/10.1002/anie.198510261. [Online]. Available: https://onlinelibrary.wiley.com/doi/abs/10.1002/anie.198510261.

[44] R. Gruehn and R. Glaum, "New results of chemical transport as a method for the preparation and thermochemical investigation of solids," *Angewandte Chemie International Edition*, vol. 39, no. 4, pp. 692–716, 2000. DOI: https://doi.org/10.1002/(SICI)1521-3773(20000218)39:4<692::AID-ANIE692>3.0.CO;2-6. eprint: https://doi.org/10.1002/(SICI)1521-3773(20000218)39:4<692::AID-ANIE692>3.0.CO;2-6. [Online]. Available: https://doi.org/10.1002/(SICI)1521-3773(20000218)39:4%3C692::AID-ANIE692%3E3.0.CO;2-6.

[45] N. V. Golubko, V. Y. Proidakova, G. M. Kaleva, *et al.*, "Synthesizing and investigating the structure and phase transitions in a3teo6 (a—mn, co, ni) oxides," *Bulletin of the Russian Academy of Sciences: Physics*, vol. 74, pp. 724–726, 2010. DOI: https://doi.org/10.3103/S1062873810050400. [Online]. Available: https://link.springer.com/article/10.3103/S1062873810050400.

[46] X. Zhu, Z. Wang, X. Su, and P. M. Vilarinho, "New cu3teo6 ceramics: Phase formation and dielectric properties," *ACS Applied Materials & Interfaces*, vol. 6, no. 14, pp. 11 326–11 332, 2014, PMID: 24960531. DOI: 10.1021/am501742z. eprint: https://doi.org/10.1021/am501742z. [Online]. Available: https://doi.org/10.1021/am501742z.

[47] O. V. Dolomanov, L. J. Bourhis, R. J. Gildea, J. A. K. Howard, and H. Puschmann, "Olex2: A complete structure solution, refinement and analysis program," *Journal of Applied Crystallography*, vol. 42, pp. 339–341, 2009.

[48] G. M. Sheldrick, "Crystal structure refinement with *SHELXL*," *Acta Crystallographica Section C*, vol. 71, no. 1, pp. 3–8, Jan. 2015. DOI: 10.1107/S2053229614024218. [Online]. Available: https://doi.org/10.1107/S2053229614024218.

[49] A. L. Spek, "Single-crystal structure validation with the program platon.," *Journal of Applied Crystallography*, vol. 36, no. 1, pp. 7–11, 2003, ISSN: 0021-8898. [Online]. Available: https://journals.iucr.org/j/issues/2003/01/00/os0104/os0104.pdf (visited on 09/13/2022).

[50] K. Brandenburg, M. Berndt, and G. Bergerhoff, "Diamond, visuelles informationssystem für kristallstrukturen," *Universitat Bonn, Germany*, 1999.

[51] J. Lima-de-Faria, E. Hellner, F. Liebau, E. Makovicky, and E. Parthé, "Nomenclature of inorganic structure types. Report of the International Union of Crystallography Commission on Crystallographic Nomenclature Subcommittee on the Nomenclature of Inorganic Structure Types," *Acta Crystallographica Section A*, vol. 46, no. 1, pp. 1–11, Jan. 1990. DOI: 10.1107/S0108767389008834. [Online]. Available: https://doi.org/10.1107/S0108767389008834.

[52] H. S. Effenberger and E. Tillmanns, "The crystal structure of k2{cu[teo4(oh)2]} h2o," *Zeitschrift für Kristallographie - Crystalline Materials*, vol. 205, no. 1-2, pp. 41–54, 1993. DOI: doi:10.1524/zkri.1993.205.12.41. [Online]. Available: https://doi.org/10.1524/zkri.1993.205.12.41.

[53] *Grundlagen und Hauptgruppenelemente*. Berlin, Boston: De Gruyter, 2017, pp. 693–738, ISBN: 9783110495850. DOI: doi:10.1515/9783110495850. [Online]. Available: https://doi.org/10.1515/9783110495850.

[54] A. K. Bera, S. M. Yusuf, L. Keller, F. Yokaichiya, and J. R. Stewart, "Magnetism of two-dimensional honeycomb layered $Na_2Ni_2TeO_6$ driven by intermediate na-layer crystal structure," *Physical Review B*, vol. 105, no. 1, Jan. 2022. DOI: 10.1103/physrevb.105.014410. [Online]. Available: https://doi.org/10.1103%5C%2Fphysrevb.105.014410.

[55] Y. J. Shan, Y. Yoshioka, M. Wakeshima, K. Tezuka, and H. Imoto, "Synthesis, structure, and magnetic properties of the novel sodium cobalt tellurate $Na_5Co_{15\cdot 5}Te_6O_{36}$," *Journal of Solid State Chemistry*, vol. 211, pp. 63–68, 2014, ISSN: 0022-4596. DOI: https://doi.org/10.1016/j.jssc.2013.12.003. [Online]. Available: https://www.sciencedirect.com/science/article/pii/S0022459613005902.

[56] B. Wedel, K. Sugiyama, K. Hiraga, and K. Itagaki, "On a lead nickel manganese tellurium oxide $PbMn_2Ni_6Te_3O_{18}$ containing mn2+ in trigonal prismatic oxygen coordination," *Materials Research Bulletin*, vol. 34, no. 14, pp. 2193–2199, 1999, ISSN: 0025-5408. DOI: https://doi.org/10.1016/S0025-5408(99)00231-7. [Online]. Available: https://www.sciencedirect.com/science/article/pii/S0025540899002317.

[57] S. Van Smaalen, *Incommensurate Crystallography*, ser. International Union of Crystallography Monographs on Crystallography. OUP Oxford, 2007, ISBN: 9780191524783. [Online]. Available: https://books.google.at/books?id=jQpREAAAQBAJ.

[58] A. Zaraq, B. Orayech, A. Faik, J. Igartua, A. Jouanneaux, and A. E. Bouari, "High temperature induced phase transitions in $SrCaCoTeO_6$ and $SrCaNiTeO_6$ ordered double perovskites," *Polyhedron*, vol. 110, pp. 119–124, 2016, ISSN: 0277-5387. DOI: https://doi.org/10.1016/j.poly.2016.02.041. [Online]. Available: https://www.sciencedirect.com/science/article/pii/S0277538716001352.

[59] D. Iwanaga, Y. Inaguma, and M. Itoh, "Crystal structure and magnetic properties of b-site ordered perovskite-type oxides $A_2CuB'O_6$ (a=ba, sr; b'=w, te)," *Journal of Solid State Chemistry*, vol. 147, no. 1, pp. 291–295, 1999, ISSN: 0022-4596. DOI: https://doi.org/10.1006/jssc.1999.8273. [Online]. Available: https://www.sciencedirect.com/science/article/pii/S0022459699982737.

[60] R. Becker, M. Johnsson, and H. Berger, "A new synthetic cobalt tellurate: Co_3TeO_6," *Acta Crystallographica Section C*, vol. 62, no. 8, pp. i67–i69, Aug. 2006. DOI: 10.1107/S010827010602347X. [Online]. Available: https://doi.org/10.1107/S010827010602347X.

[61] S. Bevara, S. N. Achary, N. Garg, *et al.*, "Pressure and temperature dependent structural studies on hollandite type ferrotitanate and crystal structure of a high pressure phase," *Inorganic Chemistry*, vol. 57, no. 4, pp. 2157–2168, 2018, PMID: 29397694. DOI: 10.1021/acs.inorgchem.7b03028. eprint: https://doi.org/10.1021/acs.inorgchem.7b03028. [Online]. Available: https://doi.org/10.1021/acs.inorgchem.7b03028.

[62] A. Knyazev, N. Chernorukov, I. Ladenkov, and S. S. Belopol'skaya, "Synthesis, structure, and thermal expansion of $M_2Fe_2Ti_6O_{16}$ and $MFeTiO_4$ compounds," *Inorganic Materials*, vol. 47, no. 999, 2011. DOI: 10.1134/S0020168511090123. eprint: https://doi.org/10.1134/S0020168511090123. [Online]. Available: https://doi.org/10.1134/S0020168511090123.

6 List of figures

List of Figures

7 List of tables

List of Tables

8 Appendix

8.1 Supplemental crystal structure data

8.1.1 Supplemental data for $K_4Ni_5Te_3O_{16}$

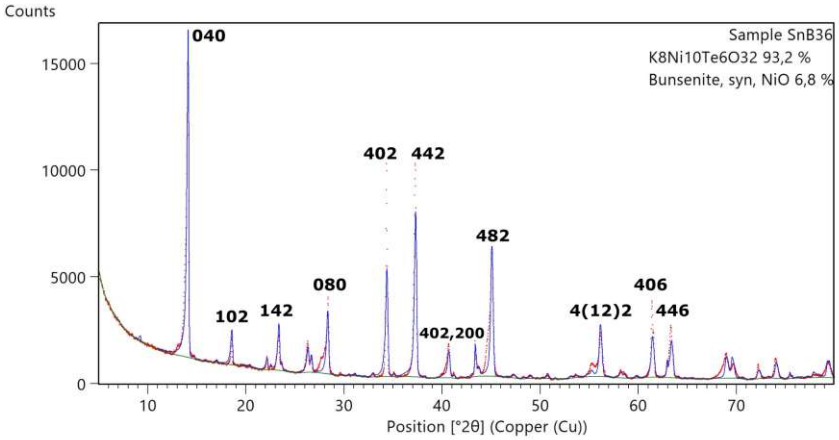

(a) Rietveld fit of sample SnB36 containing $K_4Ni_5Te_3O_{16}$ and NiO.

(b) Difference plot for the Rietveld fit in 45a.

Figure 45: Supplemental Rietveld fit of sample SnB36 containing $K_4Ni_5Te_3O_{16}$.

Table 13: Reported distances between selected atoms in $K_4Ni_5Te_3O_{16}$. K positions are selected for the well characterized K layer.

Atoms	Distance [Å]
K1-O1	3.024(17)
K1-O3	2.683(17)
K1-O8	2.769(17)
K1-O12	2.665(17)
K1-O15	3.011(18)
K1-O20	2.728(18)
K2-O1	2.755(19)
K2-O1	2.755(19)
K2-O14	2.72(2)
K2-O15	2.716(19)
K2-O15	2.716(19)
K2-O21	2.67(2)
K3-O3	2.827(18)
K3-O3	2.827(18)
K3-O5	2.57(2)
K3-O8	2.879(18)
K3-O8	2.879(18)
K3-O10	2.66(2)

Atoms	Distance [Å]
K1-K2	3.744(8)
K1-K2	4.640(7)
K1-K3	4.097(8)
K1-K3	3.583(6)
K2-K3	6.0425(6)

Atoms	Distance [Å]
Te1-Ni1	3.0373(202)
Te1-Ni2	2.9730(207)
Te1-Ni3	2.9872(24)
Te2-Te2	3.1530(21)
Te2-Ni2	2.9720(28)
Te2-Ni3	3.0036(203)
Te2-Ni4	3.0822(199)
Te2-Ni5	2.9789(203)
Te2-Ni6	3.0268(198)
Te3-Te3	3.1745(21)
Te3-Ni1	2.9774(28)
Te3-Ni3	2.9801(203)
Te3-Ni4	3.0217(198)
Te3-Ni5	2.9956(204)
Te3-Ni6	3.0861(199)
Te4-Ni1	2.9562(194)
Te4-Ni2	3.0339(203)
Te4-Ni5	3.0043(24)
Ni1-Ni1	2.936(5)
Ni2-Ni2	2.968(6)
Ni2-Ni3	2.999(6)

Table 14: Wyckoff sites and atomic positions in $K_4Ni_5Te_3O_{16}$. "Occ." stands for the occupation in case of partial occupation or occupational disorder.

Atom	Wyckoff	Site	Occ.	x/a	y/b	z/c
Te1	4e	m..		1/2	0.624 74(8)	0.2897(14)
Te2	8f	1		0.130 68(12)	0.623 47(8)	0.5387(13)
Te3	8f	1		0.131 57(12)	0.623 28(8)	0.0391(13)
Te4	4e	m..		1/2	0.624 69(9)	0.7896(13)
Ni1	8f	1		0.6217(2)	0.625 63(15)	0.0352(17)
Ni2	8f	1		0.3770(2)	0.625 09(14)	0.5363(18)
Ni3	8f	1		0.2524(2)	0.623 90(13)	0.2879(18)
Ni4	4d	m..		0	0.624 62(18)	0.2852(18)
Ni5	8f	1		0.2510(2)	0.622 95(13)	−0.2123(18)
Ni6	4d	m..		0	0.626 78(16)	−0.2141(18)
K1	8f	1	0.8449	0.7322(5)	0.7494(3)	0.3086(13)
K2	4d	m..	0.8178	0	0.7502(5)	0.6274(14)
K3	4e	m..	0.8441	1/2	0.7490(5)	1.0948(13)
K4	2a	mm2		0	1/2	−0.1927(15)
K5	4c	.m.	0.4407	0.2734(11)	1/2	−0.0955(18)
K6	4c	.m.	0.81(2)	0.377 51	1/2	0.209 04
K7	4c	.m.	0.19(2)	0.0458(9)	1/2	0.2704(16)
K8	4c	.m.	0.1404	0.070(4)	1/2	0.550(7)
K9	4c	.m.	0.6186	0.2492(11)	1/2	0.3679(19)
K10	4c	.m.	0.3993	1/2	1/2	0.430(7)
K11	4c	.m.	0.6417	0.3818(16)	1/2	0.548(2)
K12	2b	mm2	0.7844	0.3551(9)	1/2	0.7105(16)
K13	4c	.m.	0.3446	1/2	0.5858(9)	0.143(2)
K14	4c	.m.	0.75	0.6181(10)	0.6665(6)	0.217(2)
O1	8f	1		0.395 49	1/2	0.089 79
O2	4e	m..		1/2	0.6678(9)	0.947(2)
O3	8f	1		1/2	0.5781(8)	0.639(2)
O5	4e	m..		0.3824(9)	0.5831(5)	0.874(2)
O6	4e	m..		0.3838(10)	0.6645(6)	0.714(2)
O7	8f	1		0.383(1)	0.5826(6)	0.378(2)
O8	8f	1		1/2	0.6646(9)	0.448(2)
O9	8f	1		0.2383(15)	0.5799(9)	0.6259(19)
O10	4e	m..		0.2407(10)	0.6665(7)	0.4635(17)
O11	8f	1		0	0.5854(9)	0.624(2)
O12	8f	1		0.1235(11)	0.6628(6)	0.1980(19)
O13	4d	m..		0	0.6638(9)	0.471(2)
O14	4d	m..		0.1224(11)	0.6649(6)	0.699(2)
O15	8f	1		0.1239(9)	0.5812(5)	0.3881(19)
O16	8f	1		0.2403(15)	0.5792(8)	0.1253(19)
O17	8f	1		0	0.5785(9)	0.122(2)
O18	4d	m..		0.1253(10)	0.5851(6)	−0.108(2)
O19	8f	1		0.2422(11)	0.6649(7)	−0.0353(17)
O20	8f	1		0	0.6653(9)	−0.025(2)
O21	4d	m..		0.354 04	1/2	0.041 93

Table 15: Atomic displacement parameters in $K_4Ni_5Te_3O_{16}$. * = isotropic atomic displacement parameters.

Atom	U_{11}	U_{22}	U_{33}	U_{23}	U_{13}	U_{12}
Te1	0.0065(9)	0.0092(11)	0.0060(11)	−0.0030(9)	0	0
Te2	0.0070(10)	0.0133(10)	0.0062(8)	−0.0028(7)	0.0006(9)	−0.0003(7)
Te3	0.0062(10)	0.0117(9)	0.0068(8)	−0.0015(7)	−0.0011(9)	0.0009(7)
Te4	0.0069(9)	0.0124(11)	0.0063(11)	−0.0020(10)	0	0
Ni1	0.0050(17)	0.018(2)	0.0032(17)	−0.0026(14)	0.0000(15)	0.0015(13)
Ni2	0.0083(18)	0.0108(19)	0.0059(17)	0.0000(13)	0.0034(16)	−0.0006(13)
Ni3	0.0046(13)	0.0137(18)	0.0099(15)	−0.0022(16)	0.0011(19)	−0.0002(11)
Ni4	0.0104(19)	0.018(2)	0.000(2)	−0.0016(19)	0	0
Ni5	0.0085(14)	0.0127(18)	0.0051(14)	−0.0050(17)	−0.0039(17)	−0.0002(11)
Ni6	0.0055(18)	0.009(2)	0.007(2)	0.001(2)	0	0
K1	0.045(3)	0.0061(16)	0.050(4)	0.004(4)	−0.028(3)	0.003(4)
K2	0.021(4)	0.007(3)	0.040(5)	0.004(5)	0	0
K3	0.028(4)	0.008(2)	0.014(3)	0.001(4)	0	0
K4*	0.019(2)					
K5*	0.013(3)					
K6*	0.047(3)					
K7*	0.047(3)					
K8*	0.02					
K9	0.033(7)	0.027(5)	0.032(8)	0	−0.015(5)	0
K10*	0.153(18)					
K11*	0.041(3)					
K12*	0.32(3)					
K13*	0.02					
K14	0.039(6)	0.007(4)	0.036(6)	0	−0.012(5)	0
O1*	0.007(3)					
O2*	0.006(5)					
O3*	0.008(3)					
O5*	0.01					
O6*	0.003(4)					
O7*	0.007(3)					
O8*	0.007(3)					
O9*	0.013(3)					
O10*	0.007(4)					
O11*	0.014(4)					
O12*	0.002(3)					
O13*	0.005(5)					
O14*	0.003(4)					
O15*	0.010(3)					
O16*	0.005(3)					
O17*	0.014(4)					
O18*	0.011(5)					
O19*	0.008(3)					
O20*	0.004(3)					
O21*	0.007(5)					

8.1.2 Supplemental data for $K_{5.5}(Co_{0.9}Ni_{0.1})_{14.5}Te_6O_{36}$

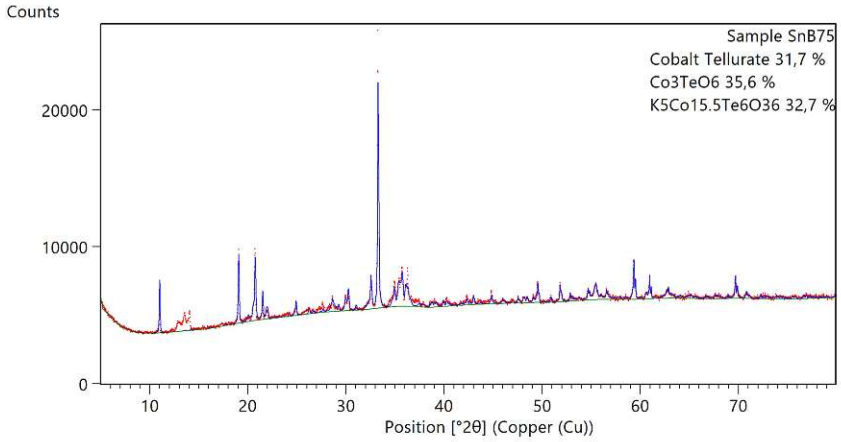

(a) Rietveld fit of sample SnB75 containing $K_{5.5}(Co_{0.9}Ni_{0.1})_{14.5}Te_6O_{36}$.

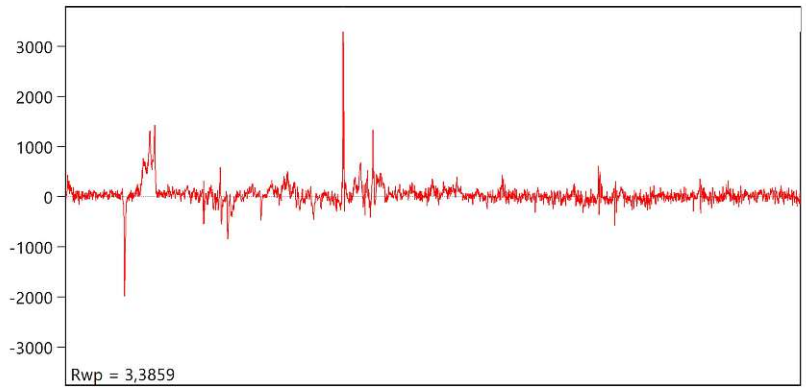

(b) Difference plot for the Rietveld fit in 46a.

Figure 46: Supplemental Rietveld fit of sample SnB75 containing $K_{5.5}(Co_{0.9}Ni_{0.1})_{14.5}Te_6O_{36}$.

Table 16: Wyckoff sites and atomic positions in $K_{5.5}(Co_{0.9}Ni_{0.1})_{14.5}Te_6O_{36}$. "Occ." stands for the occupation in case of partial occupation or occupational disorder.

Atom	Wyckoff	Site	Occ.	x/a	y/b	z/c
Te1	6h	m..		0.353 32(3)	0.341 54(3)	3/4
Co1	12i	1		0.009 13(5)	0.354 37(5)	0.588 74(4)
K1	2b	-3..		0	0	1/2
O1	12i	1		0.5252(2)	0.3921(3)	0.9013(2)
O2	6h	m..		0.2937(4)	0.1151(3)	3/4
O3	12i	1		0.2091(3)	0.3190(3)	0.5917(2)
O4	6h	m..		0.4491(3)	0.5833(3)	3/4
Co2	4f	3..	0.224(9)	1/3	2/3	0.6098(11)
Co3	2c	-6..	0.785(13)	2/3	1/3	3/4
K2	4f	3..	0.776(9)	1/3	2/3	0.5765(5)
K3	2c	-6..	0.215(13)	2/3	1/3	3/4

Table 17: Atomic displacement parameters in $K_{5.5}(Co_{0.9}Ni_{0.1})_{14.5}Te_6O_{36}$.

Atom	U_{11}	U_{22}	U_{33}	U_{23}	U_{13}	U_{12}
Te1	0.007 21(11)	0.006 49(11)	0.006 04(10)	0	0	0.003 20(9)
Co1	0.011 18(17)	0.010 17(17)	0.006 94(16)	−0.000 68(10)	−0.000 17(12)	0.006 38(14)
K1	0.0112(4)	0.0112(4)	0.0585(13)	0	0	0.0056(2)
O1	0.0081(8)	0.0115(9)	0.0098(8)	−0.0011(7)	−0.0008(6)	0.0028(7)
O2	0.0155(13)	0.0069(11)	0.0072(11)	0	0	0.0050(10)
O3	0.0100(9)	0.0148(9)	0.0072(8)	0.0001(6)	−0.0005(6)	0.0072(7)
O4	0.0103(13)	0.0063(12)	0.0207(14)	0	0	0.0019(10)
Co2	0.0182(3)	0.0182(3)	0.024(2)	0	0	0.009 12(16)
Co3	0.0089(3)	0.0089(3)	0.0107(4)	0	0	0.004 46(13)
K2	0.0182(3)	0.0182(3)	0.024(2)	0	0	0.009 12(16)
K3	0.0089(3)	0.0089(3)	0.0107(4)	0	0	0.004 46(13)

8.1.3 Supplemental data for $K_{4.67}Cd_{15.67}Te_6O_{36}$

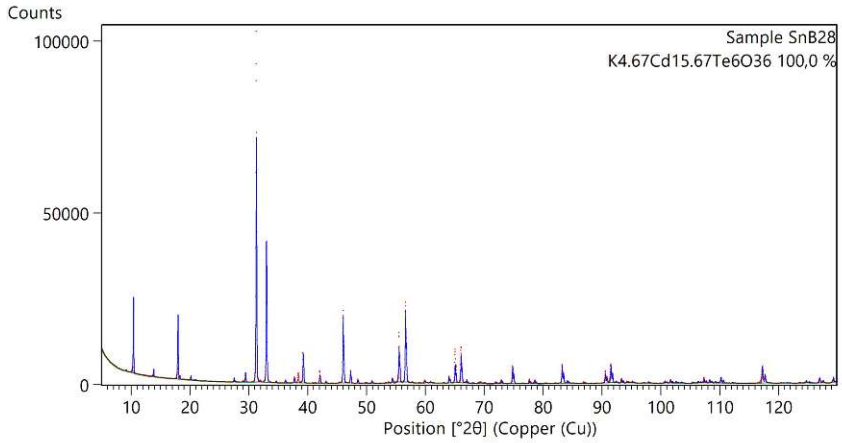

(a) Rietveld fit of sample SnB28 containing $K_{4.67}Cd_{15.67}Te_6O_{36}$.

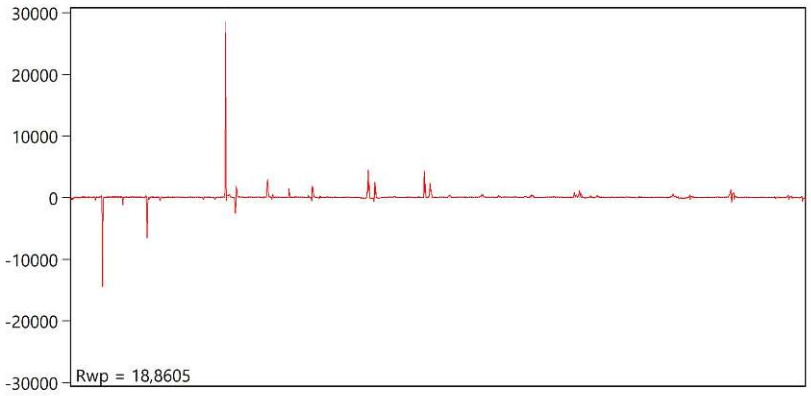

(b) Difference plot for the Rietveld fit in 47a.

Figure 47: Supplemental Rietveld fit of sample SnB28 containing $K_{4.67}Cd_{15.67}Te_6O_{36}$.

Table 18: Wyckoff sites and atomic positions in $K_{4.67}Cd_{15.67}Te_6O_{36}$. "Occ." stands for the occupation in case of partial occupation or occupational disorder.

Atom	Wyckoff	Site	Occ.	x/a	y/b	z/c
Te1	6g	1		1.009 33(16)	0.355 60(17)	0.249 10(15)
Cd1	2d	3..		4/3	2/3	0.2491(3)
Cd2	6g	1		1.3424(2)	0.346 83(19)	0.087 67(16)
Cd3	2d	3..	0.45(3)	2/3	1/3	0.0807(5)
Cd4	2d	3..	0.22(2)	2/3	1/3	0.4200(5)
Cd5	6g	1	0.877(16)	0.653 69(19)	−0.003 57(19)	0.413 28(16)
K1	2d	3..	0.55(3)	2/3	1/3	0.0807(5)
K2	2d	3..	0.78(2)	2/3	1/3	0.4200(5)
K3	6g	1	0.123(16)	0.653 69(19)	−0.003 57(19)	0.413 28(16)
K4	2c	3..	0.19(4)	1	0	0.440(4)
K5	2c	3..	0.19(4)	1	0	0.325(4)
K6	2c	3..	0.16(5)	1	0	0.221(5)
K7	2c	3..	0.56(7)	1	0	0.096 44
O1	6g	1		1.130(2)	0.5089(19)	0.1056(16)
O2	6g	1		1.132(2)	0.5116(19)	0.3914(17)
O3	6g	1		1.1625(19)	0.2924(19)	0.2467(16)
O4	6g	1		0.8928(19)	0.2129(19)	0.1060(16)
O5	6g	1		0.880(3)	0.449(2)	0.242(2)
O6	6g	1		0.8904(19)	0.2096(18)	0.3921(16)

Table 19: Atomic displacement parameters in $K_{4.67}Cd_{15.67}Te_6O_{36}$. * = isotropic displacement parameter.

Atom	$\mathbf{U_{11}}$	$\mathbf{U_{22}}$	$\mathbf{U_{33}}$	$\mathbf{U_{23}}$	$\mathbf{U_{13}}$	$\mathbf{U_{12}}$
Te1	0.0143(8)	0.0146(8)	0.0194(8)	0.0003(5)	0.0005(5)	0.0070(6)
Cd1	0.0193(7) *					
Cd2	0.0187(5) *					
Cd3	0.022(2)	0.022(2)	0.024(3)	0	0	0.0108(10)
Cd4	0.009(2)	0.009(2)	0.017(3)	0	0	0.0047(11)
Cd5	0.0137(10)	0.0147(10)	0.0154(10)	−0.0003(6)	0.0006(6)	0.0070(7)
K1	0.022(2)	0.022(2)	0.024(3)	0	0	0.0108(10)
K2	0.009(2)	0.009(2)	0.017(3)	0	0	0.0047(11)
K3	0.0137(10)	0.0147(10)	0.0154(10)	−0.0003(6)	0.0006(6)	0.0070(7)
K4	0.016(15) *					
K5	0.015(15) *					
K6	0.010(18) *					
K7	0.025(10)	0.025(10)	0.42(11)	0	0	0.012(5)
O1	0.022(9)	0.019(9)	0.016(8)	0.006(6)	0.003(6)	0.003(7)
O2	0.024(9)	0.019(9)	0.031(10)	−0.004(7)	0.004(7)	0.010(8)
O3	0.017(8)	0.019(8)	0.016(7)	0.003(6)	0.000(6)	0.000(7)
O4	0.020(3) *					
O5	0.036(12)	0.027(11)	0.071(15)	0.002(9)	0.000(10)	0.024(10)
O6	0.021(8)	0.013(8)	0.017(8)	−0.006(6)	0.000(6)	0.000(7)

8.1.4 Supplemental data for $Ca_2Te_2O_7$

Table 20: Wyckoff sites and atomic positions in $Ca_2Te_2O_7$.

Atom	Wyckoff	Site	x/a	y/b	z/c
Te1	2i	1	0.146 30(9)	0.157 97(5)	0.575 32(6)
Te2	2i	1	0.515 56(12)	0.278 93(5)	0.216 52(6)
Te3	2i	1	0.617 59(9)	0.141 86(5)	0.648 74(6)
Te4	2i	1	1.013 14(12)	0.275 00(4)	0.217 37(6)
Ca1	2i	1	0.6218(4)	0.622 18(14)	0.131 50(17)
Ca2	2i	1	0.2526(2)	0.518 03(14)	0.517 64(17)
Ca3	2i	1	0.1183(4)	0.615 52(15)	0.155 25(18)
Ca4	2i	1	0.2519(2)	0.016 98(14)	0.015 98(17)
O1	2i	1	1.2766(8)	0.2601(5)	0.1526(6)
O2	2i	1	0.9679(8)	0.1097(5)	0.1128(7)
O3	2i	1	0.9953(7)	0.1771(5)	0.4254(7)
O4	2i	1	1.0521(8)	0.4328(5)	0.3434(6)
O5	2i	1	1.0567(9)	0.3777(5)	0.0337(6)
O6	2i	1	0.7488(8)	0.2874(5)	0.2945(6)
O7	2i	1	0.5295(8)	0.1120(5)	0.1204(7)
O8	2i	1	0.3837(7)	0.1818(6)	0.4271(7)
O9	2i	1	0.4952(9)	0.4383(5)	0.3390(7)
O10	2i	1	0.6130(9)	0.3836(5)	0.0312(6)
O11	2i	1	0.6632(13)	0.3275(5)	0.6696(6)
O12	2i	1	0.7981(7)	0.1320(6)	0.7740(7)
O13	2i	1	0.3818(7)	0.1424(5)	0.7854(7)
O14	2i	1	0.1652(13)	0.3274(5)	0.6741(6)

Table 21: Atomic displacement parameters in $Ca_2Te_2O_7$.

Atom	U_{11}	U_{22}	U_{33}	U_{23}	U_{13}	U_{12}
Te1	0.0117(2)	0.0099(2)	0.0119(2)	0.000 56(15)	−0.0025(3)	0.0018(2)
Te2	0.0078(2)	0.0092(2)	0.0094(2)	−0.000 64(14)	−0.0015(3)	0.0019(3)
Te3	0.0121(3)	0.0111(2)	0.0144(2)	−0.000 77(16)	−0.0033(3)	0.0025(2)
Te4	0.0075(2)	0.0094(2)	0.0092(2)	−0.000 52(14)	−0.0014(3)	0.0019(3)
Ca1	0.0131(8)	0.0128(7)	0.0130(7)	0.0001(5)	−0.0026(9)	0.0018(9)
Ca2	0.0112(7)	0.0112(7)	0.0119(7)	0.0002(5)	−0.0026(7)	0.0023(8)
Ca3	0.0115(7)	0.0153(7)	0.0118(7)	0.0007(5)	−0.0017(8)	0.0027(9)
Ca4	0.0115(7)	0.0113(7)	0.0124(7)	0.0012(5)	−0.0022(8)	0.0018(8)
O1	0.008(2)	0.018(3)	0.014(2)	−0.0021(19)	−0.004(2)	0.002(3)
O2	0.016(4)	0.011(3)	0.018(3)	−0.006(2)	−0.004(2)	0.004(2)
O3	0.014(3)	0.016(3)	0.013(3)	0.003(2)	−0.001(2)	0.003(2)
O4	0.012(3)	0.011(3)	0.014(3)	−0.004(2)	−0.003(2)	0.003(2)
O5	0.013(4)	0.012(3)	0.014(3)	0.002(2)	−0.003(2)	0.001(2)
O6	0.009(2)	0.019(3)	0.013(2)	−0.0021(19)	−0.005(2)	0.006(3)
O7	0.015(4)	0.013(3)	0.018(3)	−0.006(2)	−0.004(2)	0.005(2)
O8	0.014(3)	0.019(3)	0.012(3)	0.004(2)	0.000(2)	0.003(2)
O9	0.022(4)	0.008(2)	0.016(3)	−0.005(2)	−0.004(2)	0.005(2)
O10	0.012(3)	0.014(3)	0.012(3)	0.0024(19)	−0.001(2)	0.001(2)
O11	0.019(3)	0.008(2)	0.015(3)	0.0009(18)	−0.001(4)	0.004(4)
O12	0.015(3)	0.018(3)	0.018(3)	0.006(2)	−0.006(2)	0.003(2)
O13	0.015(3)	0.014(3)	0.018(3)	0.000(2)	0.000(2)	0.004(2)
O14	0.015(3)	0.014(2)	0.012(2)	−0.0028(19)	−0.003(4)	0.006(4)

8.1.5 Supplemental data for $CaCu_2TeO_6$

Table 22: Wyckoff sites and atomic positions in Ca_2CuTeO_6.

Atom	Wyckoff	Site	x/a	y/b	z/c
Te1	4d	-1	1/4	1/4	1/2
Cu2	4c	-1	1/4	1/4	0
Cu1	4e	2	0	0.475 43(6)	1/4
Ca1	4e	2	0	−0.012 51(9)	1/4
O3	8f	1	0.150 16(17)	0.2886(2)	0.2470(2)
O2	8f	1	0.328 60(19)	0.502 02(19)	0.4990(3)
O1	8f	1	0.412 11(18)	0.1818(3)	0.3758(2)

Table 23: Atomic displacement parameters in Ca_2CuTeO_6.

Atom	U_{11}	U_{22}	U_{33}	U_{23}	U_{13}	U_{12}
Te1	0.005 64(9)	0.004 03(9)	0.006 43(8)	−0.000 25(8)	0.001 69(5)	0.000 06(8)
Cu2	0.009 38(16)	0.005 34(17)	0.008 77(14)	−0.000 90(16)	0.002 28(11)	−0.001 17(17)
Cu1	0.0105(2)	0.006 44(19)	0.0170(2)	0.000	0.005 58(16)	0.000
Ca1	0.0075(3)	0.0098(3)	0.0070(3)	0.000	0.0010(2)	0.000
O3	0.0121(8)	0.0084(7)	0.0083(6)	0.0006(5)	0.0000(5)	0.0012(5)
O2	0.0095(8)	0.0048(8)	0.0112(7)	−0.0004(5)	0.0031(6)	−0.0007(5)
O1	0.0124(9)	0.0106(8)	0.0230(9)	−0.0036(6)	0.0096(7)	−0.0003(6)

8.1.6 Supplemental data for $Ca_3Cu_3Te_2O_{12}$

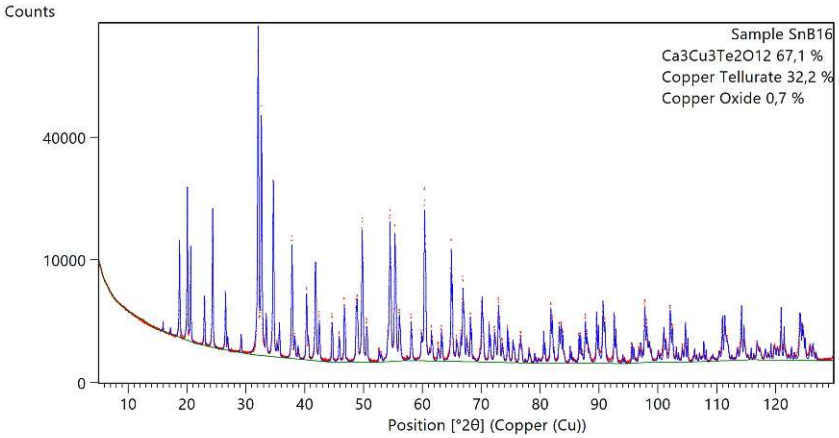

(a) Rietveld fit of sample SnB16 containing $Ca_3Cu_3Te_2O_{12}$ as well as Cu_3TeO_6 and traces of CuO.

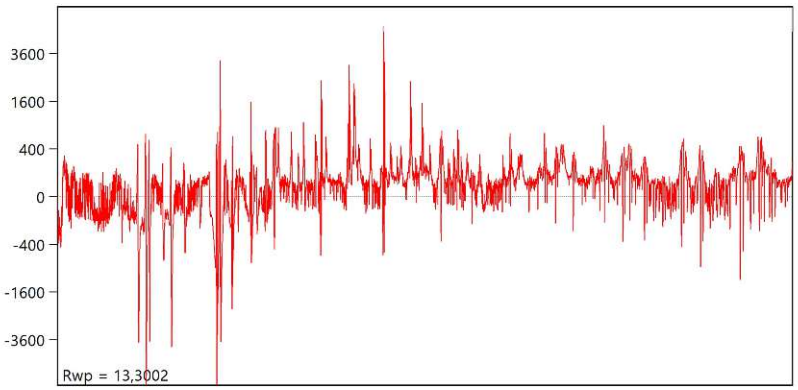

(b) Difference plot for the Rietveld fit in 46a.

Figure 48: Supplemental Rietveld fit of sample SnB75 containing $K_{5.5}(Co_{0.9}Ni_{0.1})_{14.5}Te_6O_{36}$.

Table 24: Wyckoff sites and atomic positions in $Ca_3Cu_3Te_2O_{12}$.

Atom	Wyckoff	Site	x/a	y/b	z/c
Te1	4e	..2/m	1/2	1/2	1/2
Cu1	2a	-42m	3/4	1/4	3/4
Cu2	4f	..2/m	0	1/2	1/2
Ca1	2b	-42m	1/4	3/4	3/4
Ca2	4c	222.	1/4	1/4	3/4
O1	8m	..m	0.5657(2)	0.4343(2)	0.7071(2)
O2	16n	1	0.252 33(18)	0.489 24(18)	0.570 13(18)

Table 25: Atomic displacement parameters in $Ca_3Cu_3Te_2O_{12}$.

Atom	U_{11}	U_{22}	U_{33}	U_{23}	U_{13}	U_{12}
Te1	0.005 77(8)	0.005 77(8)	0.006 60(10)	0.000 22(14)	0.000 01(9)	−0.000 01(9)
Cu1	0.0073(2)	0.0073(2)	0.0117(5)	−0.000 000	−0.000 000	0.000 000
Cu2	0.006 83(12)	0.006 83(12)	0.0132(2)	0.0010(3)	−0.002 18(19)	−0.002 18(19)
Ca1	0.0092(4)	0.0092(4)	0.0079(7)	−0.000 000	−0.000 000	0.000 000
Ca2	0.0204(5)	0.0073(4)	0.0099(4)	−0.000 000	−0.000 000	0.000 000
O1	0.0118(6)	0.0118(6)	0.0074(9)	0.0040(9)	−0.0012(6)	0.0012(6)
O2	0.0062(6)	0.0111(7)	0.0103(8)	−0.0006(9)	0.0004(4)	−0.0010(6)

8.1.7 Supplemental data for $Ca_5Te_4O_{12}Cl_2$

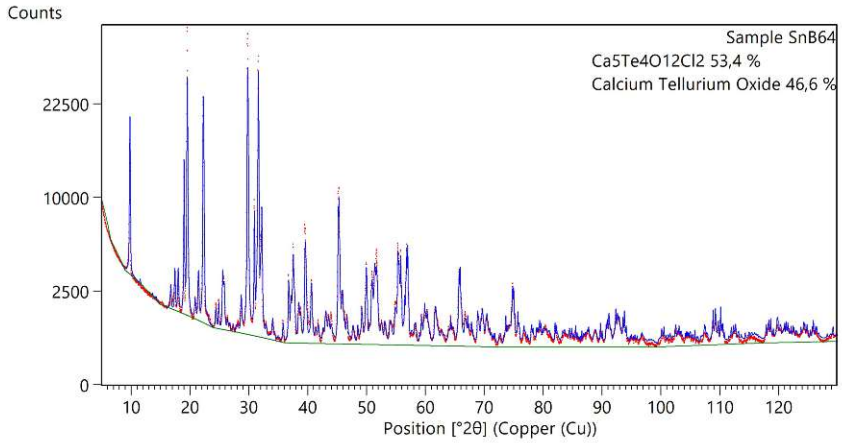

(a) Rietveld fit of sample SnB64 containing $Ca_5Te_4O_{12}Cl_2$ and Ca_3TeO_6.

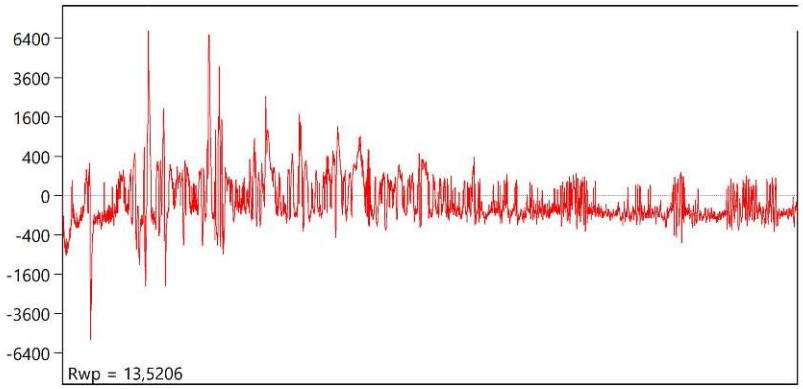

(b) Difference plot for the Rietveld fit in 49a.

Figure 49: Supplemental Rietveld fit of sample SnB64 containing $Ca_5Te_4O_{12}Cl_2$.

Table 26: Reported bond angles and distances of distorted trigonal prismatic [CaO_4Cl_2] Ca1 and Ca4 polyhedra in $Ca_5Te_4O_{12}Cl_2$.

Atom 1	Atom 2	Distance [Å]
Ca1	Cl1	2.8375(9)
Ca1	Cl2	2.8433(9)
Ca1	O2	2.9288(24)
Ca1	O3	2.2794(19)
Ca1	O4	2.3336(20)
Ca1	O7	2.2983(19)
Ca1	O12	2.3994(21)
Ca4	Cl3	2.7869(10)
Ca4	Cl4	2.7938(9)
Ca4	O1	2.3664(18)
Ca4	O6	2.2538(19)
Ca4	O9	2.4871(19)
Ca4	O10	2.2949(19)

Atom 1	Atom 2	Atom 3	Angle [°]
O4	Ca1	Cl1	129.911(52)
O3	Ca1	O12	98.141(70)
O3	Ca1	O7	136.931(67)
O3	Ca1	O4	76.904(68)
O3	Ca1	O2	72.630(66)
O3	Ca1	Cl2	130.487(50)
O3	Ca1	Cl1	80.891(48)
Cl2	Ca1	O2	146.570(49)
Cl1	Ca1	O2	132.258(49)
Cl1	Ca1	Cl2	79.881(12)
O4	Ca1	O2	81.842(69)
O12	Ca1	O2	62.233(67)
O12	Ca1	Cl2	124.318(52)
O12	Ca1	Cl1	83.802(51)
O7	Ca1	O12	77.628(69)
O7	Ca1	O4	81.750(67)
O7	Ca1	O2	67.581(66)
O7	Ca1	Cl2	81.466(50)
O7	Ca1	Cl1	139.474(51)
O4	Ca1	O12	143.217(70)
O4	Ca1	Cl2	81.508(51)
O10	Ca4	O1	79.542(65)
O6	Ca4	O1	79.850(66)
O6	Ca4	Cl4	128.994(53)
O6	Ca4	Cl3	85.829(52)
O1	Ca4	O9	128.117(63)
O1	Ca4	Cl4	147.017(49)
O1	Ca4	Cl3	84.088(47)
Cl3	Ca4	Cl4	82.880(14)
O6	Ca4	O10	134.461(69)
O9	Ca4	Cl3	141.990(49)
O9	Ca4	Cl4	77.621(47)
O10	Ca4	Cl3	131.386(53)
O10	Ca4	Cl4	86.681(51)
O6	Ca4	O9	81.721(66)
O10	Ca4	O9	79.919(65)

Table 27: Wyckoff sites and atomic positions in $Ca_5Te_4O_{12}Cl_2$.

Atom	Wyckoff	Site	x/a	y/b	z/c
Te1	8d	1	0.429 22(2)	0.391 15(2)	−0.129 39(2)
Te2	8d	1	0.438 82(2)	0.379 25(2)	0.372 84(2)
Te3	8d	1	0.731 30(2)	0.365 04(2)	0.381 64(2)
Te4	8d	1	0.735 14(2)	0.362 46(2)	0.870 85(2)
Ca1	8d	1	0.591 34(3)	0.368 88(3)	0.121 55(4)
Ca2	8d	1	0.252 94(3)	0.496 43(3)	0.345 79(4)
Ca3	8d	1	0.917 82(3)	0.495 12(3)	0.381 94(4)
Ca4	8d	1	0.585 20(3)	0.364 41(3)	0.634 32(4)
Ca5	8d	1	0.909 48(3)	0.498 81(3)	0.892 07(4)
Cl1	4c	.m.	0.588 59(7)	1/4	−0.041 44(10)
Cl2	4c	.m.	0.578 13(7)	1/4	0.284 15(10)
Cl3	4c	.m.	0.477 63(7)	1/4	0.638 51(12)
Cl4	4c	.m.	0.693 35(6)	1/4	0.628 65(9)
O1	8d	1	0.488 85(10)	0.427 55(11)	−0.254 47(15)
O2	8d	1	0.374 06(12)	0.475 37(13)	−0.090 75(17)
O3	8d	1	0.504 06(11)	0.414 16(11)	−0.013 39(15)
O4	8d	1	0.492 12(11)	0.415 77(12)	0.242 38(16)
O5	8d	1	0.377 06(12)	0.459 45(14)	0.405 18(18)
O6	8d	1	0.512 33(11)	0.410 44(11)	0.484 32(16)
O7	8d	1	0.668 12(11)	0.414 44(11)	0.272 75(16)
O8	8d	1	0.820 06(13)	0.415 16(14)	0.3365(2)
O9	8d	1	0.692 82(11)	0.416 87(11)	0.511 98(16)
O10	8d	1	0.660 89(11)	0.414 65(11)	0.782 41(16)
O11	8d	1	0.816 99(11)	0.420 94(12)	0.817 27(17)
O12	8d	1	0.709 17(12)	0.401 16(12)	1.017 99(17)

Table 28: Atomic displacement parameters in $Ca_5Te_4O_{12}Cl_2$.

Atom	U_{11}	U_{22}	U_{33}	U_{23}	U_{13}	U_{12}
Te1	0.011 52(6)	0.017 09(7)	0.009 55(6)	0.000 31(6)	0.000 18(5)	−0.003 41(5)
Te2	0.011 12(6)	0.016 27(7)	0.009 46(6)	−0.000 34(6)	0.000 39(5)	−0.003 16(5)
Te3	0.011 46(6)	0.011 92(7)	0.009 59(6)	−0.000 34(5)	0.000 57(5)	−0.000 70(5)
Te4	0.010 23(6)	0.011 50(6)	0.008 62(6)	−0.000 48(5)	0.000 70(5)	−0.000 74(5)
Ca1	0.010 93(18)	0.0185(2)	0.008 55(18)	−0.000 39(17)	−0.000 54(14)	0.001 75(16)
Ca2	0.008 66(18)	0.0164(2)	0.009 96(17)	−0.000 05(16)	−0.000 14(14)	−0.001 35(17)
Ca3	0.011 82(19)	0.0152(2)	0.0109(2)	0.000 06(17)	−0.002 75(14)	0.000 12(16)
Ca4	0.011 69(19)	0.0166(2)	0.009 48(18)	−0.000 87(18)	−0.001 26(16)	0.001 89(16)
Ca5	0.012 13(19)	0.0160(2)	0.011 66(19)	−0.002 09(17)	−0.001 96(15)	−0.000 59(16)
Cl1	0.0349(6)	0.0188(5)	0.0228(5)	0.000	0.0050(4)	0.000
Cl2	0.0332(5)	0.0178(4)	0.0232(5)	0.000	−0.0004(4)	0.000
Cl3	0.0218(5)	0.0192(5)	0.0474(7)	0.000	0.0026(5)	0.000
Cl4	0.0202(4)	0.0174(4)	0.0202(4)	0.000	0.0009(3)	0.000
O1	0.0113(8)	0.0203(9)	0.0089(7)	−0.0005(6)	0.0021(6)	0.0002(7)
O2	0.0139(9)	0.0383(13)	0.0135(8)	−0.0064(9)	0.0005(7)	0.0091(8)
O3	0.0144(8)	0.0179(9)	0.0097(7)	0.0013(7)	−0.0043(6)	0.0012(7)
O4	0.0152(8)	0.0265(11)	0.0122(8)	0.0047(7)	0.0049(7)	0.0043(8)
O5	0.0152(9)	0.0392(14)	0.0190(9)	−0.0101(9)	−0.0012(7)	0.0112(9)
O6	0.0163(8)	0.0206(10)	0.0117(8)	0.0036(7)	−0.0057(6)	−0.0049(7)
O7	0.0182(9)	0.0178(9)	0.0100(7)	0.0017(7)	−0.0035(6)	0.0010(7)
O8	0.0183(10)	0.0355(13)	0.0290(11)	−0.0088(10)	0.0057(8)	−0.0103(9)
O9	0.0188(9)	0.0187(10)	0.0098(7)	−0.0029(7)	0.0029(6)	−0.0019(7)
O10	0.0158(8)	0.0182(9)	0.0125(8)	−0.0015(7)	−0.0032(6)	0.0041(7)
O11	0.0154(9)	0.0244(11)	0.0162(8)	0.0000(8)	0.0017(7)	−0.0067(8)
O12	0.0247(10)	0.0279(12)	0.0137(8)	−0.0094(8)	0.0072(7)	−0.0109(9)

8.1.8 Supplemental data for $Ca_2TeO_3Cl_2$

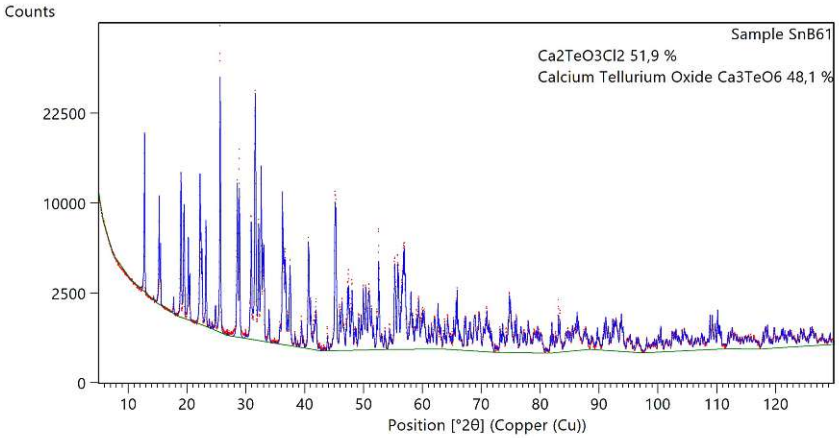

(a) Rietveld fit of sample SnB61 containing $Ca_2TeO_3Cl_2$ and Ca_3TeO_6.

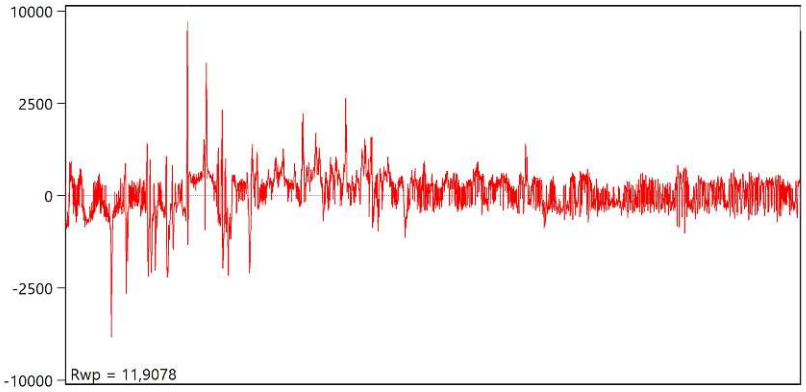

(b) Difference plot for the Rietveld fit in 50a.

Figure 50: Supplemental Rietveld fit of sample SnB61 containing $Ca_2TeO_3Cl_2$.

Table 29: Reported bond angles and distances of the irregular sevenfold [CaO_4Cl_3] coordination of Ca1 and Ca2 in $Ca_2TeO_3Cl_2$.

Atom 1	Atom 2	Distance [Å]
Ca1	O2	2.3405(17)
Ca1	O1	2.3524(17)
Ca1	O2	2.4145(21)
Ca1	O3	2.4679(16)
Ca1	Cl1	2.7933(8)
Ca1	Cl2	2.8402(10)
Ca1	Cl1	2.8455(8)
Ca2	O3	2.2864(21)
Ca2	O1	2.3616(20)
Ca2	O2	2.3844(15)
Ca2	O1	2.7259(17)
Ca2	Cl2	2.7736(8)
Ca2	Cl1	2.8658(9)
Ca2	Cl2	2.8700(8)

Atom 1	Atom 2	Atom 3	Angle [°]
O2	Ca1	O1	158.200(57)
O2	Ca1	O2	75.012(61)
O1	Ca1	O2	123.411(63)
O2	Ca1	O3	125.411(54)
O1	Ca1	O3	75.786(52)
O2	Ca1	O3	65.983(58)
O2	Ca1	Cl1	79.405(42)
O1	Ca1	Cl1	101.079(42)
O2	Ca1	Cl1	112.260(47)
O3	Ca1	Cl1	81.661(40)
O2	Ca1	Cl2	80.054(40)
O1	Ca1	Cl2	91.896(41)
O2	Ca1	Cl2	78.182(41)
O3	Ca1	Cl2	124.326(38)
Cl1	Ca1	Cl2	153.400(23)
O2	Ca1	Cl1	78.544(45)
O1	Ca1	Cl1	80.216(47)
O2	Ca1	Cl1	148.734(51)
O3	Ca1	Cl1	145.029(43)
Cl1	Ca1	Cl1	78.396(20)
Cl2	Ca1	Cl1	81.112(20)
O3	Ca2	O1	124.251(72)
O3	Ca2	O2	89.429(58)
O1	Ca2	O2	109.842(66)
O3	Ca2	O1	71.839(51)
O1	Ca2	O1	71.479(53)
O2	Ca2	O1	63.974(47)
O3	Ca2	Cl2	95.620(42)
O1	Ca2	Cl2	84.412(40)
O2	Ca2	Cl2	158.559(42)
O1	Ca2	Cl2	137.316(35)
O3	Ca2	Cl1	155.790(47)
O1	Ca2	Cl1	79.640(43)
O2	Ca2	Cl1	77.225(40)
O1	Ca2	Cl1	118.069(37)
Cl2	Ca2	Cl1	90.252(21)
O3	Ca2	Cl2	77.785(49)
O1	Ca2	Cl2	155.524(52)
O2	Ca2	Cl2	78.046(46)
O1	Ca2	Cl2	130.667(38)
Cl2	Ca2	Cl2	82.673(20)
Cl1	Ca2	Cl2	79.716(21)

Table 30: Wyckoff sites and atomic positions in $Ca_2TeO_3Cl_2$.

Atom	Wyckoff	Site	x/a	y/b	z/c
Ca1	1	2i	0.184 26(6)	0.719 36(7)	0.455 05(6)
Ca2	1	2i	0.449 74(6)	0.274 44(7)	0.284 32(6)
Te1	1	2i	0.763 36(2)	0.774 68(2)	0.240 05(2)
O1	1	2i	0.5099(2)	0.8988(3)	0.3627(2)
O2	1	2i	0.8434(2)	0.6660(3)	0.4593(2)
O3	1	2i	0.6601(2)	0.5047(3)	0.2978(2)
Cl1	1	2i	−0.081 37(7)	0.851 58(9)	0.753 28(7)
Cl2	1	2i	0.697 50(8)	0.308 01(10)	−0.088 61(7)

Table 31: Atomic displacement parameters in $Ca_2TeO_3Cl_2$.

Atom	U_{11}	U_{22}	U_{33}	U_{23}	U_{13}	U_{12}
Ca1	0.006 07(12)	0.006 09(18)	0.007 60(15)	−0.002 63(13)	−0.002 91(11)	0.000 00(11)
Ca2	0.006 67(12)	0.006 08(18)	0.006 90(15)	−0.003 10(13)	−0.001 94(10)	0.000 23(11)
Te1	0.004 99(4)	0.005 53(6)	0.005 07(5)	−0.001 88(4)	−0.001 58(3)	0.000 07(3)
O1	0.0065(5)	0.0069(7)	0.0089(6)	−0.0041(5)	−0.0024(4)	0.0014(4)
O2	0.0066(5)	0.0080(7)	0.0063(5)	−0.0021(5)	−0.0029(4)	0.0000(4)
O3	0.0095(5)	0.0083(8)	0.0109(6)	−0.0038(6)	−0.0044(5)	−0.0014(5)
Cl1	0.009 57(15)	0.0075(2)	0.008 42(18)	−0.003 59(16)	−0.003 47(14)	0.000 86(14)
Cl2	0.010 53(16)	0.0095(2)	0.006 88(18)	−0.003 33(17)	−0.002 46(14)	0.002 43(15)

8.1.9 Supplemental data for $(Co_{0.93}Ni_{0.07})_3TeO_6$

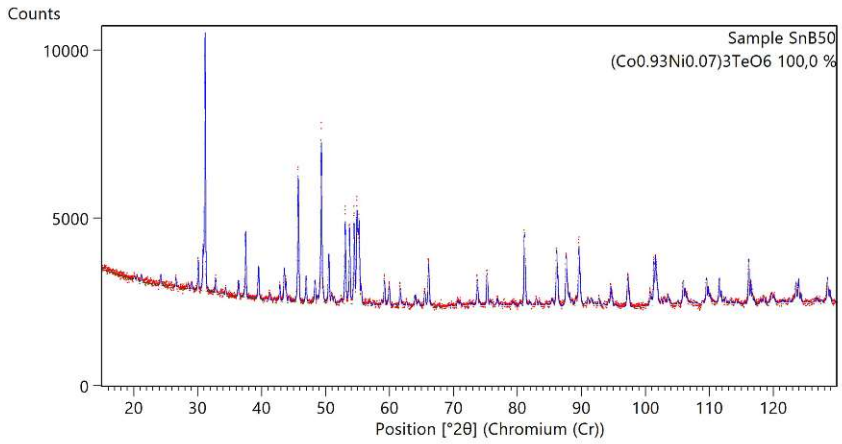

(a) Rietveld fit of sample SnB50 containing $(Co_{0.93}Ni_{0.07})_3TeO_6$.

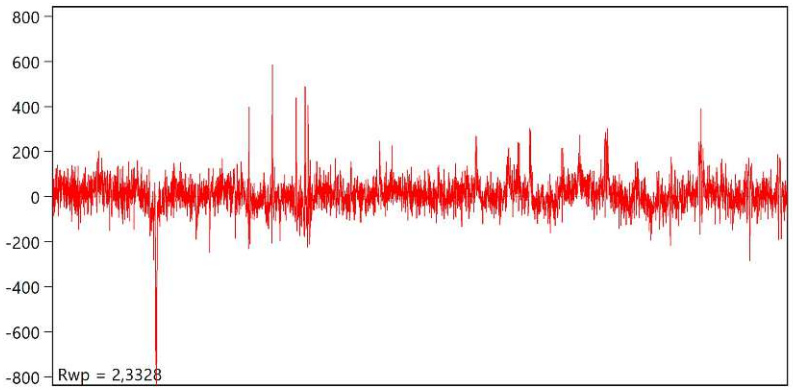

(b) Difference plot for the Rietveld fit in 53a.

Figure 51: Supplemental Rietveld fit of sample SnB50 containing $(Co_{0.93}Ni_{0.07})_3TeO_6$.

Table 32: Wyckoff sites and atomic positions in $(Co_{0.93}Ni_{0.07})_3TeO_6$.

Atom	Wyckoff	Site	x/a	y/b	z/c
Te1	4a	1	0.817 09(3)	−0.005 81(2)	0.305 58(2)
Te2	4a	1	0.558 27(3)	0.502 12(2)	0.426 14(2)
Te3	4a	1	0.431 11(3)	0.493 37(2)	0.684 64(2)
Te4	4a	1	0.191 00(3)	0.994 60(2)	0.564 12(2)
Co1	4a	1	0.938 86(4)	−0.134 44(5)	0.449 42(3)
Co2	4a	1	0.608 63(4)	−0.151 99(5)	0.435 30(2)
Co3	4a	1	0.808 53(5)	0.307 65(7)	0.192 65(3)
Co4	4a	1	0.571 49(5)	0.193 99(6)	0.303 29(3)
Co5	4a	1	0.809 28(4)	0.298 46(5)	0.425 04(3)
Co6	4a	1	0.308 57(4)	0.382 42(5)	0.316 72(3)
Co7	4a	1	0.311 61(4)	0.359 34(5)	0.535 02(3)
Co8	4a	1	0.443 51(5)	0.190 05(6)	0.807 51(3)
Co9	4a	1	0.438 97(4)	0.800 75(5)	0.565 58(3)
Co10	4a	1	0.141 98(4)	0.650 14(4)	0.557 75(3)
Co11	4a	1	0.438 32(4)	1.123 64(5)	0.672 74(3)
Co12	4a	1	0.174 07(4)	1.308 28(6)	0.679 31(3)
O1	4a	1	1.0401(4)	0.0070(2)	0.504 92(16)
O2	4a	1	0.8937(2)	−0.1805(3)	0.354 71(11)
O3	4a	1	0.7408(3)	0.1597(3)	0.258 32(14)
O4	4a	1	0.9033(2)	0.1273(3)	0.370 65(12)
O5	4a	1	0.7352(3)	−0.1650(3)	0.250 96(14)
O6	4a	1	0.9759(3)	−0.0021(2)	0.254 42(17)
O7	4a	1	0.6615(4)	−0.0094(3)	0.359 54(16)
O8	4a	1	0.6350(3)	0.3343(3)	0.378 75(14)
O10	4a	1	0.6461(3)	0.6580(3)	0.372 61(13)
O11	4a	1	0.4843(2)	0.3512(3)	0.489 66(12)
O12	4a	1	0.4034(3)	0.5217(3)	0.376 87(16)
O13	4a	1	0.4951(2)	0.6775(3)	0.477 99(11)
O14	4a	1	0.2094(4)	0.5105(3)	0.485 40(16)
O15	4a	1	0.3519(2)	0.3274(3)	0.630 06(12)
O16	4a	1	0.5163(3)	0.6442(3)	0.740 08(13)
O17	4a	1	0.5859(4)	0.4946(2)	0.631 36(17)
O18	4a	1	0.2731(4)	0.4930(3)	0.736 46(17)
O19	4a	1	0.5076(3)	0.3194(3)	0.731 75(12)
O20	4a	1	0.3472(3)	0.6431(3)	0.627 58(13)
O21	4a	1	0.2559(2)	0.8192(3)	0.513 72(12)
O22	4a	1	0.1125(3)	1.1627(3)	0.609 72(14)
O23	4a	1	0.1056(3)	0.8415(3)	0.618 74(13)
O24	4a	1	0.2670(2)	1.1435(3)	0.498 75(12)
O25	4a	1	0.3452(3)	0.9830(3)	0.612 87(16)

Table 33: Atomic displacement parameters in $(Co_{0.93}Ni_{0.07})_3TeO_6$.

Atom	U_{11}	U_{22}	U_{33}	U_{23}	U_{13}	U_{12}
Te1	0.004 52(11)	0.005 02(8)	0.004 98(8)	−0.000 04(6)	0.000 24(6)	0.000 04(4)
Te2	0.004 68(10)	0.004 95(10)	0.004 86(8)	0.000 00(4)	−0.000 12(7)	0.000 08(4)
Te3	0.004 60(10)	0.004 87(8)	0.005 05(8)	−0.000 05(6)	0.000 16(7)	−0.000 09(5)
Te4	0.004 93(10)	0.004 70(9)	0.004 85(8)	0.000 02(5)	−0.000 05(7)	0.000 00(4)
Co1	0.009 82(17)	0.012 81(18)	0.007 81(17)	−0.002 51(14)	−0.000 54(12)	−0.002 56(13)
Co2	0.010 96(16)	0.007 94(14)	0.005 36(14)	−0.001 13(12)	0.001 21(12)	−0.001 88(12)
Co3	0.006 75(16)	0.007 41(16)	0.006 86(17)	0.000 99(14)	0.000 21(12)	0.000 65(13)
Co4	0.006 06(17)	0.006 99(15)	0.007 07(16)	−0.000 58(14)	0.000 20(12)	0.000 24(12)
Co5	0.006 31(15)	0.007 58(15)	0.006 94(15)	0.000 30(13)	0.000 22(11)	0.000 38(11)
Co6	0.008 21(15)	0.008 41(15)	0.006 73(16)	0.000 51(13)	−0.001 48(12)	−0.000 72(12)
Co7	0.009 00(16)	0.009 97(16)	0.007 33(15)	0.001 37(13)	−0.000 85(12)	0.001 44(12)
Co8	0.007 36(16)	0.008 09(16)	0.005 44(15)	0.000 45(14)	0.000 90(12)	0.001 43(13)
Co9	0.006 53(15)	0.007 88(15)	0.007 02(15)	−0.000 30(13)	0.000 17(11)	−0.000 10(11)
Co10	0.012 00(16)	0.007 80(14)	0.006 01(14)	−0.001 00(13)	0.002 03(13)	−0.002 47(12)
Co11	0.008 91(16)	0.008 41(15)	0.007 02(16)	−0.000 98(13)	−0.001 07(12)	−0.001 24(12)
Co12	0.006 18(15)	0.007 27(16)	0.006 19(16)	−0.000 78(14)	−0.000 10(12)	0.000 50(13)
O1	0.0075(13)	0.0077(10)	0.0072(10)	0.0002(6)	−0.0018(9)	−0.0015(6)
O2	0.0087(9)	0.0080(8)	0.0055(8)	0.0016(7)	0.0005(6)	0.0018(7)
O3	0.0078(10)	0.0094(9)	0.0109(9)	0.0046(8)	0.0014(7)	0.0025(7)
O4	0.0070(8)	0.0098(9)	0.0101(9)	−0.0051(7)	−0.0007(7)	−0.0006(7)
O5	0.0084(10)	0.0098(9)	0.0100(9)	−0.0034(8)	0.0011(7)	−0.0018(7)
O6	0.0044(13)	0.0073(11)	0.0077(11)	−0.0001(6)	0.0017(9)	0.0000(5)
O7	0.0070(12)	0.0085(10)	0.0070(11)	0.0013(6)	0.0018(9)	0.0008(6)
O8	0.0086(10)	0.0095(10)	0.0104(10)	−0.0045(8)	−0.0017(7)	0.0021(8)
O10	0.0081(9)	0.0065(9)	0.0073(9)	0.0016(7)	0.0016(7)	0.0002(7)
O11	0.0086(9)	0.0083(9)	0.0087(9)	0.0013(7)	0.0005(7)	−0.0016(7)
O12	0.0057(10)	0.0095(8)	0.0117(10)	−0.0019(9)	−0.0025(8)	0.0020(8)
O13	0.0083(9)	0.0084(9)	0.0068(9)	−0.0016(7)	0.0013(6)	0.0003(7)
O14	0.0069(13)	0.0092(10)	0.0077(10)	−0.0004(7)	−0.0021(9)	0.0008(7)
O15	0.0087(8)	0.0079(8)	0.0072(8)	−0.0010(7)	−0.0011(6)	−0.0013(7)
O16	0.0077(9)	0.0086(9)	0.0083(9)	−0.0032(7)	0.0007(7)	−0.0006(7)
O17	0.0063(12)	0.0083(11)	0.0090(12)	−0.0016(6)	0.0026(9)	−0.0010(6)
O18	0.0086(15)	0.0093(12)	0.0077(12)	0.0010(6)	0.0008(10)	0.0005(6)
O19	0.0074(9)	0.0070(8)	0.0078(8)	0.0014(7)	0.0001(7)	0.0018(7)
O20	0.0085(9)	0.0104(9)	0.0107(9)	0.0033(7)	0.0008(7)	0.0011(7)
O21	0.0088(9)	0.0073(8)	0.0077(9)	−0.0021(7)	0.0015(7)	0.0014(7)
O22	0.0078(10)	0.0103(10)	0.0095(10)	−0.0048(8)	−0.0021(7)	0.0020(8)
O23	0.0079(9)	0.0079(9)	0.0074(9)	0.0015(8)	0.0016(7)	−0.0013(8)
O24	0.0072(9)	0.0084(9)	0.0080(9)	0.0022(7)	0.0017(7)	−0.0011(7)
O25	0.0079(10)	0.0095(8)	0.0081(9)	−0.0020(8)	−0.0031(8)	0.0001(8)

8.1.10 Supplemental data for $H_8Rb_4Cu_2Te_2O_{14}$

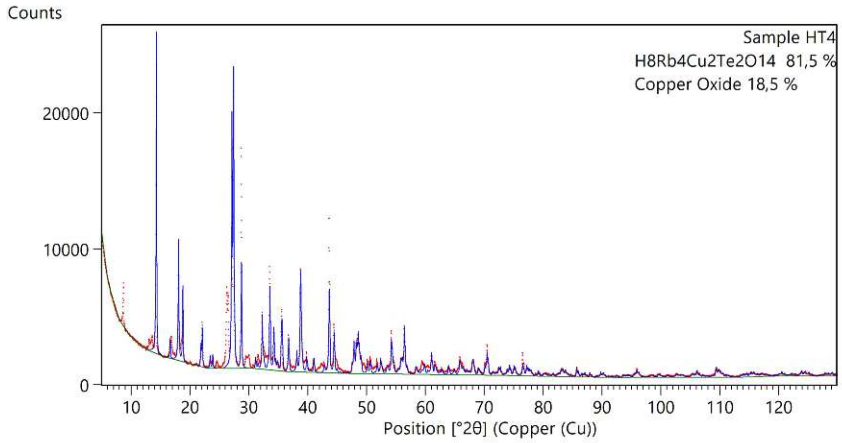

(a) Rietveld fit of sample HT4 containing $H_8Rb_4Cu_2Te_2O_{14}$ and CuO as well as at least one unidentified phase.

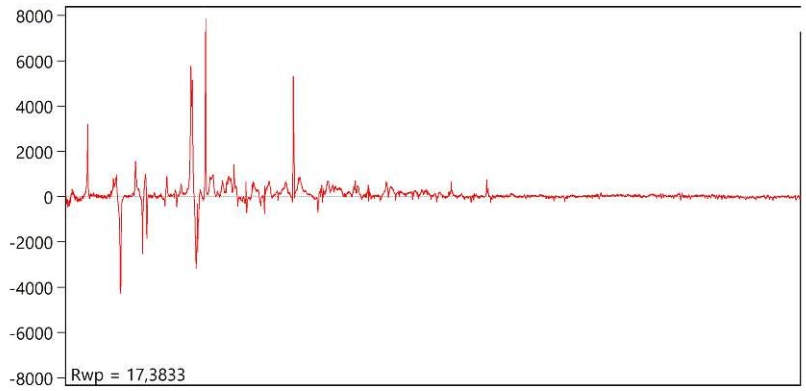

(b) Difference plot for the Rietveld fit in 50a.

Figure 52: Supplemental Rietveld fit sample HT4 containing $H_4Rb_4Cu_2Te_2O_{14}$.

Table 34: Wyckoff sites and atomic positions in $H_8Rb_4Cu_2Te_2O_{14}$.

Atom	Wyckoff	Site	x/a	y/b	z/c
Te1	4a	1	0.511 10(2)	0.749 32(5)	0.537 87(2)
Rb1	4a	1	0.435 66(6)	0.778 68(8)	0.226 22(4)
Rb2	4a	1	0.556 63(6)	0.262 12(8)	0.356 42(4)
Cu1	4a	1	0.7625(1)	0.995 13(11)	0.538 19(9)
O1	4a	1	0.6187(4)	0.4844(5)	0.5510(4)
O2	4a	1	0.3912(4)	0.6144(6)	0.4355(3)
O3	4a	1	0.3828(4)	0.6435(6)	0.6419(3)
O4	4a	1	0.6331(4)	0.8772(6)	0.6412(3)
O5	4a	1	0.6414(4)	0.8472(6)	0.4348(3)
O6	4a	1	0.4082(5)	1.0120(5)	0.5201(4)
O7	4a	1	0.2365(4)	0.8836(6)	0.7719(4)
H1	4a	1	0.664(7)	0.458(11)	0.602(4)
H2	4a	1	0.449(7)	0.69(1)	0.473(5)
H3	4a	1	0.279(10)	0.803(13)	0.740(7)
H4	4a	1	0.197(9)	0.829(14)	0.819(7)

Table 35: Atomic displacement parameters in $H_8Rb_4Cu_2Te_2O_{14}$.

Atom	U_{11}	U_{22}	U_{33}	U_{23}	U_{13}	U_{12}
Te1	0.009 38(8)	0.011 42(8)	0.010 19(8)	−0.000 53(7)	0.001 10(6)	−0.002 96(7)
Rb1	0.0297(3)	0.0197(2)	0.0195(2)	0.0018(2)	−0.001 06(18)	0.0004(2)
Rb2	0.0340(3)	0.0166(2)	0.0170(2)	−0.000 81(18)	0.0012(2)	0.000 42(18)
Cu1	0.011 10(16)	0.015 08(19)	0.013 74(16)	0.000 83(14)	0.000 55(12)	−0.004 85(14)
O1	0.0184(19)	0.0158(17)	0.020(2)	−0.0002(14)	−0.0019(15)	0.0026(12)
O2	0.0128(16)	0.0183(16)	0.0118(18)	−0.0005(13)	−0.0019(12)	−0.0082(12)
O3	0.0130(15)	0.0211(18)	0.0115(16)	−0.0017(13)	0.0025(12)	−0.0061(12)
O4	0.0148(16)	0.0192(18)	0.0107(17)	−0.0012(13)	−0.0002(12)	−0.0064(12)
O5	0.0149(15)	0.0171(17)	0.0111(17)	−0.0005(13)	0.0026(12)	−0.0060(12)
O6	0.0207(19)	0.0147(17)	0.023(2)	0.0005(14)	0.0023(16)	0.0004(13)
O7	0.032(2)	0.0199(15)	0.027(2)	0.0030(14)	0.0108(16)	0.0028(14)

8.1.11 Supplemental data for $H_6K_3FeTe_2O_{12}$ and $H_4K_3FeTe_2O_{11}$

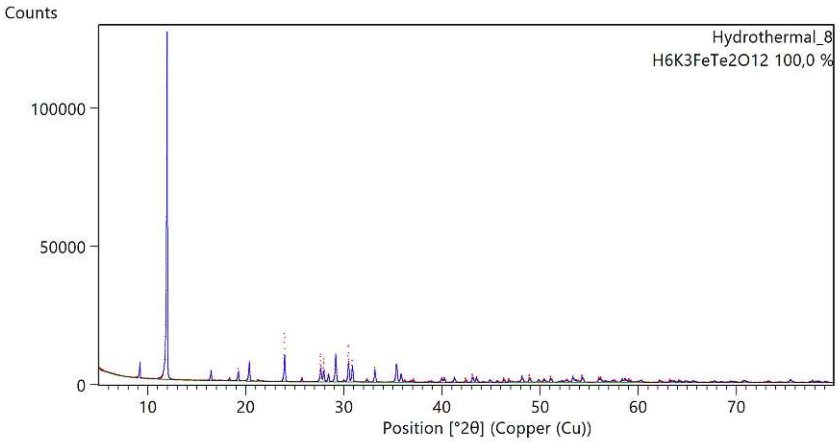

(a) Rietveld fit of sample HT8 containing $H_6K_3FeTe_2O_{12}$.

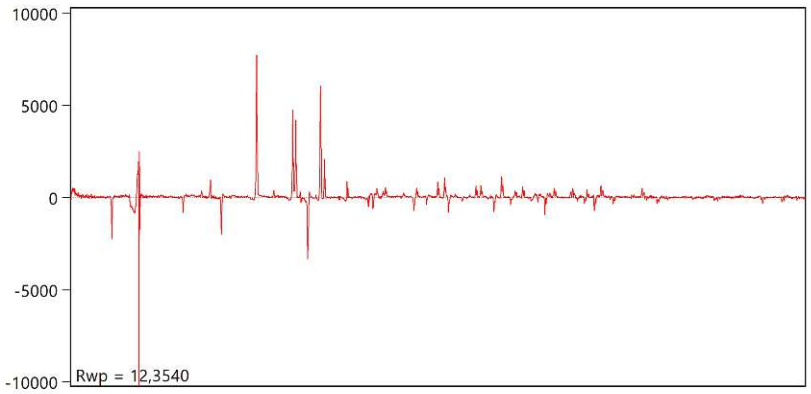

(b) Difference plot for the Rietveld fit in 53a.

Figure 53: Supplemental Rietveld fit of sample HT8 containing $H_6K_3FeTe_2O_{12}$.

Table 36: Wyckoff sites and atomic positions in $H_6K_3FeTe_2O_{12}$. "Occ." stands for the occupation in case of partial occupation or occupational disorder.

Atom	Wyckoff	Site	Occ.	x/a	y/b	z/c
Te2	4e	-1		3/4	3/4	0
Te1	4h	2	0.793(2)	1	0.716 61(2)	1/2
Fe1'	4h	2	0.207(2)	1	0.716 61(2)	1/2
Fe1	4g	2	0.793(2)	1/2	0.783 64(4)	0
Te1'	4g	2	0.207(2)	1/2	0.783 64(4)	0
K1	8j	1		0.702 96(5)	0.630 34(4)	0.4514(5)
K2	4i	m		0.647 61(7)	1	−0.1000(9)
O1	8j	1		0.504 32(15)	0.695 48(12)	0.2652(4)
H1	8j	1		0.8697(15)	0.874(2)	0.105(9)
O2	8j	1		0.845 07(16)	0.714 48(18)	0.3273(13)
H2	4i	m		0.907(2)	1/2	0.614(10)
O3	8j	1		0.656 48(17)	0.784 68(19)	0.1389(15)
O4	8j	1		0.491 66(14)	0.869 24(12)	−0.2670(5)
O5	8j	1		0.807 10(14)	0.872 35(13)	0.0616(15)
O6	4i	m		0.8519(2)	1/2	0.611(3)
O7	4i	m	0.343(14)	0.5418(17)	1/2	0.187(4)
O7'	4i	m	0.657(14)	0.5411(8)	1/2	0.333(2)

Table 37: Atomic displacement parameters in $H_6K_3FeTe_2O_{12}$.

Atom	U_{11}	U_{22}	U_{33}	U_{23}	U_{13}	U_{12}
Te2	0.004 15(8)	0.012 00(10)	0.0061(4)	0.000 23(9)	0.0015(5)	0.000 45(7)
Te1	0.004 36(11)	0.010 64(16)	0.0049(3)	0	0.0012(4)	0
Fe1'	0.004 36(11)	0.010 64(16)	0.0049(3)	0	0.0012(4)	0
Fe1	0.005 61(19)	0.0123(3)	0.0058(6)	0	0.0019(7)	0
Te1'	0.005 61(19)	0.0123(3)	0.0058(6)	0	0.0019(7)	0
K1	0.0188(2)	0.0192(3)	0.0172(6)	0.0023(7)	0.0088(7)	0.0046(2)
K2	0.0170(4)	0.0223(4)	0.0279(10)	0	0.0064(12)	0
O1	0.0094(7)	0.0123(8)	0.0140(14)	−0.0012(8)	0.0051(15)	0.0003(6)
O2	0.0047(7)	0.0215(11)	0.0059(18)	0.0007(16)	0.0032(11)	0.0005(9)
O3	0.0061(8)	0.0222(12)	0.014(2)	−0.0024(18)	0.0047(13)	0.0015(10)
O4	0.0109(7)	0.0115(8)	0.0108(12)	−0.0001(8)	0.0028(14)	0.0004(6)
O5	0.0095(7)	0.0136(8)	0.0185(18)	0.001(2)	0.0042(19)	−0.0005(6)
O6	0.0111(12)	0.0161(13)	0.038(4)	0	0.008(4)	0